Learning patient–specific parameters for a diffuse interface glioblastoma model from neuroimaging data

Abramo Agosti‡, Pasquale Ciarletta‡, Harald Garcke♯, Michael Hinze*

‡ MOX–Dipartimento di Matematica, Politecnico di Milano
via Bonardi 9, 20133 Milano, Italy
abramo.agosti@polimi.it

♯ Fakultät für Mathematik, Universität Regensburg
93040 Regensburg, Germany
harald.garcke@ur.de

* Mathematisches Institut, Universität Koblenz-Landau
D-56070 Koblenz, Germany
hinze@uni-koblenz.de

Abstract

Parameters in mathematical models for glioblastoma multiforme (GBM) tumour growth are highly patient specific. Here we aim to estimate parameters in a Cahn–Hilliard type diffuse interface model in an optimised way using model order reduction (MOR) based on proper orthogonal decomposition (POD). Based on snapshots derived from finite element simulations for the full order model (FOM) we use POD for dimension reduction and solve the parameter estimation for the reduced order model (ROM). Neuroimaging data are used to define the highly inhomogeneous diffusion tensors as well as to define a target functional in a patient specific manner. The reduced order model heavily relies on the discrete empirical interpolation method (DEIM) which has to be appropriately adapted in order to deal with the highly nonlinear and degenerate parabolic PDEs. A feature of the approach is that we iterate between full order solves with new parameters to compute a POD basis function and sensitivity based parameter estimation for the ROM problems. The algorithm is applied using neuroimaging data for two clinical test cases and we can demonstrate that the reduced order approach drastically decreases the computational effort.

Mathematics Subject Classification (2010). 92C50, 65M60, 35K35, 35K65, 65K10.

Key words. diffuse interface model, degenerate Cahn–Hilliard equation, finite elements, tumour growth, personalised medicine, parameter estimation, model order reduction, discrete empirical interpolation method.

1 Introduction

Glioblastoma multiforme (GBM) is a malignant primary brain tumour characterised by high infiltration into the parenchyma and wide phenotypic heterogeneity [28]. These characteristic features of GBM provoke recurrence and marked resistance to adjuvant therapy, resulting into poor prognosis and very low survival rates [34]. Thus, the emergent development of precision medicine in neuro-oncology mainly concern the patient-specific optimisation of the clinical treatment of GBM, with the aim to guide the decision making of medical doctors for improving the quality of life of each patient [33].

In this context, mathematical models have proved useful as in-silico benchmarks to improve the prognostic prediction and to tailor personalised strategies in clinical practice

1

[47, 25]. Most existing mathematical approaches to neuro-oncology are based on reaction-diffusion partial differential systems or agent-based models, that mimic the chemical exchanges driving the tumour growth and transport properties of the tumour cells as well as the response to adjuvant therapy [22, 24, 38, 4]. Recent developments also enable the possibility to integrate neuroimaging data in the virtual reconstruction of the patient's brain, gaining insight on the effect of the brain micro–structure on the invasive pathway [26, 46, 36, 29, 13, 45, 14]. Despite the great progress in assessing accurate mathematical predictions of the prognostic clinical outcomes, the complexity underlying the physical and biological cues driving GBM invasion make it particularly difficult to quantify the accuracy of a given class of models in reproducing the observable clinical events [23].

In this work we propose a new strategy for optimising the parameter estimation of a nonlinear degenerate diffuse interface model which describes the GBM evolution integrating neuroimaging data, recently proposed and analysed in [2, 3]. This partial differential model consists of a Cahn–Hilliard equation with a single–well potential of Lennard-Jones type, a non-conserved order parameter and a degenerate mobility, that couples the growth of the tumour phase with a reaction–diffusion equation for the oxygen concentration in the brain, including the effects of the standard Stupp protocol of adjuvant therapy. In particular, it accounts for the augmented tumour motility along white matter fibers tracts, which is a typical hallmark of GBM, through the definition of heterogeneous diffusion and chemotactic coefficients directly extracted from Magnetic Resonance (MRI) and Diffusion Tensor (DTI) imaging data. Because of the peculiar non-convexity and nonlinearity of the chemical potential driving the local cell-cell interactions, the finite element approximation of the discrete model has a high computational cost, since it requires sophisticated numerical techniques to select the physical solution representing the expanding GBM boundary whilst avoiding numerical instabilities [2].

A proof-of-concept of the predictive ability of this model in clinical practice has been presented in [3], showing by a manual tuning of the model parameters how the numerical simulations on a growing GBM tumour inside the virtual brain reconstructed by segmentation of neuroimaging data could accurately fit the observed invasion patterns observed at key clinical stages after surgical removal and during adjuvant therapy. Here we propose a robust automated procedure to optimise the parameter estimation by minimising the L^2-distance between the indicator functions of the tumour distribution sets in numerical simulations and the corresponding clinical data of the GBM mass at a key time identified by our medical collaborators in the clinical protocol. The constrained optimisation problem is formulated at the numerical level as a Mathematical Problem with Equilibrium Constraints (MPEC) [30]. Due to the high computational cost of solving the Full Order Model (FOM), the numerical solution of the MPEC will be given using model order reduction. In particular, we propose an iterative algorithm extending the one proposed in [21], which computes a snapshot based POD-ROM with the help of simulations at the FOM level and estimates parameter for the Reduced Order Model (ROM) level through sensitivity analysis. The main challenge with respect to existing approach is the derivation of a ROM dealing with a singular single-well potential and a degenerate anisotropic mobility. The goal is to derive a robust iterative algorithm which converges to an optimal state, that explores new regions in the parameter space by changing the ROM basis and minimises the optimisation functional at the ROM level avoiding the ROM solution to violate the physical constraints satisfied by the full order solution. For this scope, the bottleneck is the definition of an effective order reduction of the degenerate and nonlinear terms of the diffuse interface model.

The paper is organised as follows. In Section 2 we summarise the diffuse interface model of GBM invasion and we derive the corresponding FOM and ROM discretised problems. In Section 3, we introduce a novel optimisation algorithm for parameter estimation. In Section 4, we apply this algorithm using neuroimaging data corresponding to two clinical test cases: the growth of a primary GBM and the recurrence pattern after surgical resections. The accuracy and the computational gain of the proposed numerical procedure are finally discussed in Section 5, together with few concluding remarks.

2

2 Mathematical model

In this section, we first summarise the diffuse interface model employed for the patient-specific description of GBM evolution, followed by the presentation of its FOM and ROM discretisations.

2.1 The diffuse interface model

The patient-specific GBM evolution is described using the diffuse interface model proposed in [2]. The model considers the brain tissue as a saturated mixture composed by a tumour phase with a volume fraction $\phi = \phi(\mathbf{x}, t)$ that expands at the expense of another phase made of cells and fluids, so that $0 \leq \phi \leq 1$. The mass exchanges are regulated by the oxygen concentration $n = n(\mathbf{x}, t)$ that is produced by the vascular network and consumed by the tumour cells. This multi-phase framework has proved to give a more realistic representation of the mechano-biological features underlying the tumour growth processes [39, 49, 10, 19].

Within the domain Ω representing the brain, the mathematical model is given by the following coupled PDEs:

$$\begin{cases} \frac{\partial \phi}{\partial t} = \nabla \cdot \left(\frac{\phi(1-\phi)^2}{M} \mathbf{T} \nabla \Sigma(\phi) \right) + \Gamma_\phi(\phi, n) - \nabla \cdot \left(\chi_n \phi(1-\phi)^2 \mathbf{T} \nabla n \right) & \text{in } \Omega \times (0, T), \\ \frac{\partial n}{\partial t} = \nabla \cdot (\mathbf{D} \nabla n) + \Gamma_n(\phi, n) & \text{in } \Omega \times (0, T), \end{cases} \quad (1)$$

where $\mathbf{D}$ and $\mathbf{T}$ are the diffusion tensors of oxygen and the tensor of preferential mobility, that can be extracted from neuroimaging data as in [3], M is a friction parameter that penalises the relative velocity between the phases, and χ_n is a chemotactic coefficient, that is considered to be 4 times higher in the White Matter (WM) than its value in the Grey Matter (GM) and in the Cerebrospinal Fluid (CSF). We set $\chi_n = k_n \chi$ where k_n is a chemotactic parameter which we need to estimate and $\chi = 4$ in the White Matter (WM) and $\chi = 1$ in the Grey Matter (GM) and the Cerebrospinal Fluid (CSF).

The first equation in (1) is a Cahn–Hilliard (CH) type equation with degenerate mobility and non-conserved order parameter; the chemical potential is defined by

$$\Sigma(\phi) = E(1 - \phi_e)\psi_1'(\phi) + E\psi_2'(\phi) - \gamma^2 \Delta \phi, \quad (2)$$

where E is the Young modulus of the healthy tissue, γ a characteristic short-range interaction coefficient, and ϕ_e is the homeostatic value of the volume fraction. We note that, due to the non-smoothness in space of the chemotactic coefficient χ_n, the chemotactic term is inserted in the first equation of system (1), due to stability issues of the associated numerical approximation, while it should be more natural to consider it as a micro–force term associated to a coupling energy between cells and nutrient directly in the form of the chemical potential Σ as in [19]. The local interaction potential is given by:

$$\psi_1(\phi) := -\log(1 - \phi), \quad \psi_2(\phi) := -\frac{\phi^3}{3} - (1 - \phi_e)\left(\frac{\phi^2}{2} + \phi \right),$$

and it is split into a convex ψ_1 and a non-convex ψ_2 term for future convenience. Such a functional form of the Lennard-Jones type describes attraction at low volume fraction and repulsion at beyond the homeostatic threshold ϕ_e, as proposed in [9]. A simple functional form is given for the growth term Γ_n for the oxygen :

$$\Gamma_n(\phi, n) = -\delta_n \phi n + S_n(1 - n)(1 - \phi)$$

where S_n is the production rate from the vascular network and δ_n gives the characteristic decay time. Similarly, the tumour growth rate is assumed in the form:

$$\Gamma_\phi(\phi, n) = \nu\phi(n - \delta)(1 - \phi) - k_T(t)\phi$$

3

where ν is the production rate mediated by the local oxygen concentration, and k_T is a decay rate that accounts for apoptosis and/or adjuvant therapy. The latter contribution is defined by the clinical Stupp protocol consisting of radiotherapy and chemotherapy as in [37], reading:

$$k_T(t)\phi = k_R(t)\phi + k_C(t)\phi. \tag{3}$$

The functions $k_R(t)$ and $k_C(t)$ are the temporal profiles of the radio- and chemo-therapy schedules, respectively:

$$k_R(t) = \begin{cases} R_{eff} & t_i \leq t \leq t_{i+1} \\ 0 & \text{otherwise} \end{cases} \qquad k_C(t) = \begin{cases} k_{C1} & s_0 \leq t \leq s_1 \\ k_{C2} & s_2 \leq t \leq s_3 \\ k_{C3} & s_j \leq t \leq s_{j+1} \\ 0 & \text{otherwise} \end{cases} \tag{4}$$

where the coefficients k_{C1}, k_{C2} and k_{C3} are extracted by clinical data and reflect the increasing drug dosage at different chemotherapy cycles, while t_i, t_{i+1} are the days at the beginning and at the end of radiotherapy administration periods and s_j, s_{j+1} are the days at the beginning and at the end of chemotherapy administration cycles. The radiotherapy death rate R_{eff} is modelled via the linear-quadratic (LQ) model [48] as

$$R_{eff} = \alpha md + \beta md^2\,, \tag{5}$$

where d [Gy] is the dose of radiation for every fraction, m is the number of fractions per day (here, $m = 1$ day^{-1}), α [Gy^{-1}] and β [Gy^{-2}] are two tissue-dependent parameters for cell kill [40, 42].

The model (1) is complemented by the following initial and boundary conditions:

$$\begin{cases} \nabla\phi \cdot \boldsymbol{\nu} = \nabla\Sigma \cdot \boldsymbol{\nu} = \nabla n \cdot \boldsymbol{\nu} = 0 & \text{on } \partial\Omega \times (0,T), \\ \phi(.,0) = \phi_0,\ n(.,0) = 1 & \text{in } \Omega, \end{cases} \tag{6}$$

where $\boldsymbol{\nu}$ is the outer unit normal vector to $\partial\Omega$ and ϕ_0 is the initial distribution of tumour concentration, that will be given by a neuroimaging datum at the beginning of the clinical follow-up. A list of reference biological ranges for the values of the parameters in (1) and the corresponding source is reported in Table 1.

	Parameter description	Range of values	Ref.
M	Tumour inter-phase friction	1377.86–5032.2 (Pa day)/mm^2	[44]
ν	Tumour cells proliferation rate	0.012–0.5 day^{-1}	[46, 31]
k_n	Chemotactic parameter	0.007–90.72 mm^2/(day)	[2, 3, 15]
S_n	Oxygen supply rate	10^4 day^{-1}	[10]
δ_n	Oxygen consumption rate	8640 day^{-1}	[17, 31]
γ	Diffuse interface thickness	0.29–0.78 Pa$^{1/2}$mm	[2]
E	Brain Young modulus	689.8 Pa–698.2 Pa	[12]
δ	Hypoxia threshold	0.1–0.33	[6, 32]
ϕ_e	Equilibrium cell volume fraction	0.389–0.8	[8]
m	Radiation fractions per day	1 day^{-1}	[43]
d	Radiation dose	2 Gy	[43]
α	Linear coefficient for RT induced cell kill	0.027 Gy^{-1}	[40, 37]
β	Quadratic coefficient for RT induced cell kill	0.0027 Gy^{-2}	[37, 41, 16]
k_{C1}	Concomitant chemotherapy death rate	0.00735 day^{-1}	[37]
k_{C2}	First cycle of adjuvant CHT death rate	0.0147 day^{-1}	[37]
k_{C3}	Remain. cycles of adjuvant CHT death rate	0.0196 day^{-1}	[37]

Table 1: Values or ranges of values for parameters used in the model.

As first highlighted in [7], the presence of compactly supported weak solutions of the degenerate Cahn–Hilliard equation in (1) is linked to the non-uniqueness of the solution, with the

existence of physical solutions with moving free boundary at a finite speed and unphysical ones with fixed support in time. Due to the degeneracy of the mobility and the logarithmic singularity of the potential, we remark that a weak solution of (1), (6) satisfies the positivity and separation constraints

$$0 \leq \phi < 1 \quad \text{a.e in } \Omega \times (0, T).$$

For future convenience, we finally define the following set of model parameters

$$\mathcal{P} \equiv \{L := 1/M, \nu, k_n, S_n, \delta_n, \gamma^2, E, \delta, c_e := 1 - \phi_e\},$$

whose optimal value will be searched for in the parameters optimisation problem introduced in the following sections.

2.2 FOM discretisation

In order to discretise the initial boundary value problem given by (1), (6) we start from the MRI and DTI data collected at the initial time $t = 0$ to generate the tetrahedral mesh for the discretised geometry of the brain $\mathcal{T}_h$, the map which specifies the location of the brain tissues, the initial tumour distribution and the tensors $\mathbf{D}$ and $\mathbf{T}$.
We solve the following **Initialisation** problem:
Problem 1
__Initialisation:__ Given MRI($t = 0$) and DTI($t = 0$), determine the set

$$\begin{cases} \mathcal{T}_h, \\ map(WM, GM, CSF), \\ \phi_0, \\ \mathbf{D}, \mathbf{T} \end{cases} = \textbf{\textit{Initialization}}\text{(MRI(t=0), DTI(t=0))}. \tag{7}$$

The **Initialisation** procedure is defined as follows. Starting from a segmentation of the brain tissues and of the initial tumour distribution, we extract the external brain surface and generate the computational surface and the tetrahedral internal mesh, conveniently refined around the tumour region. We also generate the labelled mesh $map(WM, GM, CSF)$ which maps each cell of the mesh to an integer value identifying the cerebral tissue the cell barycentre belongs to, together with the map for the characteristic function of the tumour distribution. The initial tumour distribution ϕ_0 is then obtained as the characteristic function of the tumour extension multiplied by the equilibrium value $\bar{\phi}$. The value $\bar{\phi}$ is obtained by solving $\Gamma_\phi(\bar{\phi}, \bar{n}) = 0 = \Gamma_n(\bar{\phi}, \bar{n})$ with $k_T(0) = 0$, i.e. $\bar{n} = \delta$ and

$$\bar{\phi} = \frac{S_n(1 - \delta)}{S_n + \delta(\delta_n - S_n)}.$$

This means that we are considering that the tumour phase is in an homogeneous equilibrium value in the tumour support at the initial temporal stage, before the application of the therapy. We finally generate the meshes containing the values of the independent components of the tensors $\mathbf{D}$ and $\mathbf{T}$ by analysing the log–signal associated to the DTI data. The extrapolation processes performed in **Problem 1** are described in detail in [2, 3].
The FOM discretisation of system (1) is obtained through the finite element method, by following the approach introduced in [2, 5]. Let us introduce the following finite element spaces:

$$Q_h := \{\chi \in C(\bar{\Omega}) : \chi|_K \in \mathbb{P}^1(K) \ \forall K \in \mathcal{T}_h\} \subset H^1(\Omega),$$
$$Q_h^+ := \{\chi \in Q_h : \chi \geq 0 \text{ in } \Omega\}$$

where $\mathbb{P}_1(K)$ indicates the space of polynomials of total order one on K. We set $\Delta t = T/N$ for a $N \in \mathbb{N}$ and $t_n = n\Delta t$, $n = 0, ..., N$. Starting from initial data $\phi_h^0 = \pi^h \phi_0$, $n_h^0 = \pi^h n_0$, where π^h is the standard Lagrangian interpolation operator, and from a set of parameters $\mathcal{P}_k$, we consider the following **FOM** discretisation. (Note that if no mesh vertex is on the

boundary of the tumour support, the Lagrangian projection $\phi_h^0 = \pi^h(\phi_0)$ is well defined. Otherwise, we take a smoothing of ϕ_0 such that $\phi_0 \in C(\bar{\Omega})$.)

Problem 2

FOM:

For $n = 1, \ldots, N$, given $(\phi_h^{n-1}, n_h^{n-1}) \in Q_h^+ \times Q_h^+$, we define

$$(\phi_h^n, \Sigma_h^n, n_h^n) = \boldsymbol{F}_k^n(\boldsymbol{Initialization}, \mathcal{P}_k) = \boldsymbol{F}_k^n(\mathcal{T}_h, map(WM, GM, CSF), \phi_0, \mathbf{D}, \mathbf{T}, \mathcal{P}_k), \quad (8)$$

where $(\phi_h^n, \Sigma_h^n, n_h^n) \in Q_h^+ \times Q_h \times Q_h^+$ satisfies, $\forall (v_h, w_h, q_h) \in Q_h \times Q_h^+ \times Q_h$,

$$
\begin{cases}
\left(\dfrac{\phi_h^n - \phi_h^{n-1}}{\Delta t}, v_h\right)^h = & -L_k(\phi_h^{n-1}(1 - \phi_h^{n-1})^2 \mathbf{T} \nabla \Sigma_h^n, \nabla v_h) + \nu_k(\phi_h^{n-1}(n_h^n - \delta_k)(1 - \phi_h^{n-1}), v_h)^h \\
& + k_{nk}(\chi \phi_h^{n-1}(1 - \phi_h^{n-1})^2 \mathbf{T} \nabla n_h^n, \nabla v_h) - (k_T \phi_h^{n-1}, v_h)^h, \\
\gamma_k^2(\nabla \phi_h^n, \nabla(w_h - \phi_h^n)) + & (E_k c_{ek} \psi_1'(\phi_h^n), w_h - \phi_h^n)^h \geq \left(\Sigma_h^n + E_k \psi_2'(\phi_h^{n-1}), w_h - \phi_h^n\right)^h, \\
\left(\dfrac{n_h^n - n_h^{n-1}}{\Delta t}, q_h\right)^h = & -(\mathbf{D}\nabla n_h^n, \nabla q_h) + S_{nk}((1 - n_h^n)(1 - \phi_h^{n-1}), q_h)^h - \delta_{nk}(\phi_h^{n-1} n_h^n, q_h)^h.
\end{cases}
$$

$$(9)$$

The finite element approximation (9) has the form of a discrete variational inequality, where the positivity of the discrete solution is enforced as a constraint. Indeed, ϕ_h^n is projected onto the space with positive values Q_h^+. This projection aims at recovering the analytical properties of the continuous solution [2, 5].

Remark 2.1 *For a solution of (9), we obtain that $\phi_h^n(\mathbf{x}_j) \geq 0$ and if $\phi_h^n(\mathbf{x}_j) > 0$ holds the equality*

$$\gamma_k^2(\nabla \phi_h^n, \nabla \chi_j) + (E_k c_{ek} \psi_1'(\phi_h^n) + E_k \psi_2'(\phi_h^{n-1}) - \Sigma_h^n, \chi_j)^h = 0 \quad (10)$$

is true, with χ_j the basis function associated to the node j. To prove this we choose in the case $\phi_h^n(\mathbf{x}_j) > 0$ in (9) the test functions $w_h = \phi_h^n \pm \frac{1}{2}\phi_h^n(\mathbf{x}_j)\chi_j$ and obtain (10) as $\phi_h^n(\mathbf{x}_j) > 0$. This shows that $\Sigma_h^n(\mathbf{x}_j)$ is uniquely defined if $\phi_h^n(\mathbf{x}_j) > 0$.

The lumped mass approximation of the L^2-scalar product is introduced in (9) in order for the discrete solution to be able to track compactly supported solutions with a moving free boundary from the unphysical ones with fixed support.

Note that the convex part of the cellular potential is treated implicitly in time, whereas the concave part is treated explicitly. The well posedness of system (9) can be shown expressing its equations as the KKT conditions of a convex minimisation problem with regular inequality constraints. It is solved by a null–space gradient projection algorithm.

2.3 ROM discretisation

We use Proper Orthogonal Decomposition (POD) reduced order modelling to obtain a ROM of the full order system (9). We follow [20], which formulates a ROM of a Cahn–Hilliard equation with constant mobility and advection by projecting the equations for ϕ and Σ onto the spaces spanned by the POD basis obtained from the time snapshots matrices associated to ϕ and Σ, respectively, and which approximates the nonlinear convex term in the double–well potential using the Discrete Empirical Interpolation Method (DEIM). In the present case, this formalism is extended to take into account for the degeneracy of the mobility and the physical constraints expected to be satisfied by the ROM solution, as well as for the presence of anisotropy and the presence of the dynamics of the nutrient. In particular, our strategy is to use DEIM interpolation to approximate the nonlinear terms ψ_1' and ψ_1'', (the latter term is needed to solve the nonlinear ROM system by a Newton method), and to project the equations for ϕ, Σ and n in (9) onto the space spanned by the POD basis associated to ϕ, Σ and n, respectively. The mobility and chemotactic terms, which contain polynomial nonlinearities in the variable ϕ, are written as higher order tensors acting on the reduced order space associated to ϕ.

We start by calculating the POD basis obtained from the snapshots matrices associated to ϕ, Σ, n, $\psi_1'(\phi)$ and $\psi_1''(\phi)$. In what follows we do not distinguish between a finite element function f_h and its nodal vector and it will be clear from the context which object is meant. For a given snapshot matrix $F = \left[f_h^0, \ldots, f_h^N\right]$ the POD basis elements ξ_s^f of the POD basis $\left\{\xi_l^f\right\}_{l=1,\ldots,N_{\mathrm{POD}}}$ are obtained as follows:

- prescribe the required information content to be covered by the POD basis as $ic \in (0,1]$;
- compute the trace $tr(F^t F)$ of the correlation matrix $F^t F = (f_h^m, f_h^l)_{ml} \in M(N+1, \mathbb{R})$, where $(\cdot, \cdot)$ denotes the chosen inner product;
- set $N_f^{\mathrm{POD}} := \min\left\{m, \left(\sum_{i \leq m} \lambda_i\right)/tr(F^t F) \geq ic\right\}$;
- (successively) compute the eigensystem $\{v^i, \lambda_i\}_{i=1,\ldots,N_f^{\mathrm{POD}}}$ of $F^t F$;
- set $\xi_s^f := \frac{1}{\sqrt{\lambda_s}} \sum_j v_j^s f_h^j$ $(1 \leq s \leq N_f^{\mathrm{POD}})$.

With this procedure we set up the POD bases for our reduced order models, whose construction is summarised in

Problem 3:

POD:

With the given time snapshots form the corresponding snapshot matrices in correspondence of the parameter set $\mathcal{P}_k$ according to $\mathbf{F}_1 := \left[\phi_h^0, \ldots, \phi_h^N\right]$, $\mathbf{F}_2 := \left[\Sigma_h^0, \ldots, \Sigma_h^N\right]$, $\mathbf{F}_3 := \left[n_h^0, \ldots, n_h^N\right]$, $\psi_1'(\mathbf{F}_1) := \left[\psi_1'(\phi_h^0), \ldots, \psi_1'(\phi_h^N)\right]$, and $\psi_1''(\mathbf{F}_1) := \left[\psi_1''(\phi_h^0), \ldots, \psi_1''(\phi_h^N)\right]$. Then compute the POD systems corresponding to the correlation matrices matrices $(\mathbf{F}_1)^T \mathbf{F}_1$, $(\mathbf{F}_2)^T \mathbf{F}_2$, $(\mathbf{F}_3)^T \mathbf{F}_3$, $(\psi_1'(\mathbf{F}_1))^T \psi_1'(\mathbf{F}_1)$, $(\psi_1''(\mathbf{F}_1))^T \psi_1'(\mathbf{F}_1)$ and set

$$N_{POD} := \max\{N_\phi^{POD}, N_\Sigma^{POD}, N_n^{POD}, N_{\psi_1'}^{POD}, N_{\psi_1''}^{POD}\}.$$

If the respective bases are computed successively complete them by adding the remaining $N_{POD} - N_\theta^{POD}$ basis elements to the basis $\left\{\xi_l^\theta\right\}_{l=1,\ldots,N_\theta^{POD}}$, where $\theta \in \{\phi, \Sigma, n, \psi_1', \psi_2''\}$. Finally assemble the respective bases in the array

$$\mathbf{P}_k := (\mathbf{P}_{k1}, \mathbf{P}_{k2}, \mathbf{P}_{k3}, \mathbf{P}_{k4}, \mathbf{P}_{k5}), \tag{11}$$

where

$$\mathbf{P}_{k1} := \left\{\xi_l^\phi\right\}_{l=1,\ldots,N_{POD}}, \mathbf{P}_{k2} := \left\{\xi_l^\Sigma\right\}_{l=1,\ldots,N_{POD}}, \mathbf{P}_{k3} := \left\{\xi_l^n\right\}_{l=1,\ldots,N_{POD}},$$

$$\mathbf{P}_{k4} := \left\{\xi_l^{\psi_1'}\right\}_{l=1,\ldots,N_{POD}}, \ and \ \mathbf{P}_{k5} := \left\{\xi_l^{\psi_1''}\right\}_{l=1,\ldots,N_{POD}}.$$

We note that POD basis elements are finite element functions. In the numerical examples we will specify N_ϕ^{POD}, N_Σ^{POD}, N_n^{POD}, $N_{\psi_1'}^{\mathrm{POD}}$, $N_{\psi_1''}^{\mathrm{POD}}$ such that the required information contents of the POD bases satisfy $ic = 0.9999$, i.e. all the POD bases contain at least 99.99% of the snapshot information.

Then we make the ansatz

$$\phi_h^n = \sum_{i=1}^{N_{\mathrm{POD}}} \alpha_{ik}^n \xi_i^\phi, \quad \Sigma_h^n = \sum_{i=1}^{N_{\mathrm{POD}}} \beta_{ik}^n \xi_i^\Sigma, \quad n_h^n = \sum_{i=1}^{N_{\mathrm{POD}}} \eta_{ik}^n \xi_i^n. \tag{12}$$

We moreover approximate the singular nonlinear terms $\psi_1'(\phi_h^n)$ and $\psi_1''(\phi_h^n)$ by a greedy algorithm using DEIM interpolation [11], i.e. by computing the nonlinearities only on the nodes of the mesh which give the greatest interpolation contribution for each of their POD basis elements,

$$\psi_1'\left(\sum_{i=1}^{N_{\mathrm{POD}}} \alpha_{ik}^n \xi_i^\phi\right) = \sum_{i=1}^{N_{\mathrm{POD}}} (P_{2,ij}^T U_{\psi_1',js})^{-1} \psi_1'(P_{2,sl}^T \Phi_{lm} \alpha_{mk}^n) \xi_i^{\psi_1'}, \tag{13}$$

$$\psi_1''\left(\sum_{i=1}^{N_{\mathrm{POD}}} \alpha_{ik}^n \xi_i^\phi\right) = \sum_{i=1}^{N_{\mathrm{POD}}} (P_{2,ij}^T U_{\psi_1'',js})^{-1} \psi_1''(P_{2,sl}^T \Phi_{lm} \alpha_{mk}^n) \xi_i^{\psi_1''}, \tag{14}$$

where $i, j, s, l, m = 1, \ldots, N_{\text{POD}}$, $U_{\psi_1'} := \left[\xi_1^{\psi_1'}, \ldots, \xi_{N_{\text{POD}}}^{\psi_1'}\right]$, $U_{\psi_1''} := \left[\xi_1^{\psi_1''}, \ldots, \xi_{N_{\text{POD}}}^{\psi_1''}\right]$, $\Phi := \left[\xi_1^\phi, \ldots, \xi_{N_{\text{POD}}}^\phi\right]$ and P_2 is the row selection operator of the DEIM interpolation nodes for the term $\psi_1''(\cdot)$. The DEIM algorithm is reported in the Appendix. We observe that we are computing both (13) and (14) on the same interpolation nodes (associated to the $\psi_1''(\cdot)$ term only). This is needed to practically enforce the separation property $\sum_{i=1}^{N_{\text{POD}}} \alpha_{ik}^{n,p} \xi_i^\phi < 1$, driven by the singularities in the terms $\psi_1'(\cdot)$ and $\psi_1''(\cdot)$, throughout the steps of the Newton algorithm.

Substituting (12) and (13) into (9), choosing $v_h \equiv \xi_m^\phi$, $w_h \equiv \xi_m^\Sigma$, $q_h \equiv \xi_m^n$, we - after replacing the original variational inequality by an equation as in the original equation (2) - obtain the following **ROM** system

$$
\begin{cases}
V_{1,mi}\dfrac{\alpha_{ik}^n - \alpha_{ik}^{n-1}}{\Delta t} &= -L_k\big(\alpha_{ik}^{n-1}\alpha_{jk}^{n-1}\alpha_{sk}^{n-1}V_{2,ijsml}\beta_{lk}^n - 2\alpha_{ik}^{n-1}\alpha_{jk}^{n-1}V_{3,ijms}\beta_{sk}^n + \alpha_{ik}^{n-1}V_{4,imj}\beta_{jk}^n\big) + \\
&\quad k_{nk}\big(\alpha_{ik}^{n-1}\alpha_{jk}^{n-1}\alpha_{sk}^{n-1}V_{8,ijsml}\eta_{lk}^n - 2\alpha_{ik}^{n-1}\alpha_{jk}^{n-1}V_{9,ijms}\eta_{sk}^n + \alpha_{ik}^{n-1}V_{10,imj}\eta_{jk}^n\big) + \\
&\quad \nu_k\big(\alpha_{ik}^{n-1}V_{5,ims} - \alpha_{ik}^{n-1}\alpha_{jk}^{n-1}V_{6,ijms}\big)\eta_{sk}^n - (\nu_k\delta_k + K_T)V_{1,mi}\alpha_{ik}^{n-1} + \nu_k\delta_k\alpha_{ik}^{n-1}V_{7,ims}\alpha_{sk}^{n-1}, \\[2ex]
U_{1,mi}\beta_{ik}^n &= \gamma_k^2 U_{6,mi}\alpha_{ik}^n + E_k c_{ek}U_{2,mi}(P_{2,ij}^T U_{\psi_1',js})^{-1}\psi_1'(P_{2,sl}^T\Phi_{lm}\alpha_{mk}^n) - E_k\alpha_{ik}^{n-1}U_{3,imj}\alpha_{jk}^{n-1} - \\
&\quad E_k c_{ek}U_{4,mi}\alpha_{ik}^{n-1} - E_k c_{ek}U_{5,m}, \\[2ex]
W_{1,mi}\dfrac{\eta_{ik}^n - \eta_{ik}^{n-1}}{\Delta t} &= -W_{2,mi}\eta_{ik}^n + S_{nk}\big(\alpha_{ik}^{n-1}W_{3,imj}\eta_{jk}^n + W_{4,m} - W_{5,mi}\alpha_{ik}^{n-1} - W_{1,mi}\eta_{ik}^{n-1}\big) - \\
&\quad \delta_{nk}\alpha_{ik}^{n-1}W_{3,imj}\gamma_{jk}^n.
\end{cases}
\tag{15}
$$

Here, $i, j, s, l, m = 1, \ldots, N_{\text{POD}}$, and the initial conditions are given by $\alpha_{ik}^0 = (\phi_h^0, \xi_i^\phi)^h$ and $\eta_{ik}^0 = (n_h^0, \xi_i^n)^h$. The second order and higher order tensors $V_1, V_2, \ldots, V_{10}, U_1, U_2, \ldots, U_6$, $W_1, \ldots, W_5$ in (15) and U_7 (needed for the Newton problem) are defined by the following **Assemble** problem in terms of $\mathbf{P}_k$ defined in (11).

Problem 4

Assemble:

$$\mathbf{A}_k(\mathbf{P}_{k1}, \mathbf{P}_{k2}, \mathbf{P}_{k3}, \mathbf{P}_{k4}, \mathbf{P}_{k5}) := (V_1, \ldots, V_{10}, U_1, U_2, \ldots, U_6, W_1, \ldots, W_5, U_7), \tag{16}$$

where

$$V_{1,ji} := (\xi_i^\phi, \xi_j^\phi)^h, \quad U_{1,ji} := (\xi_i^\Sigma, \xi_j^\Sigma)^h, \quad U_{2,ji} := (\psi_{1,i}', \xi_j^\Sigma)^h,$$

$$U_{4,ji} := (\xi_i^\phi, \xi_j^\Sigma)^h, \quad U_{5,i} := (1, \xi_i^\Sigma)^h, \quad U_{6,ji} := (\nabla\xi_i^\phi, \nabla\xi_j^\Sigma),$$

$$W_{1,ji} := (\xi_i^n, \xi_j^n)^h, \quad W_{2,ji} := (\mathbf{D}\nabla\xi_i^n, \nabla\xi_j^n), \quad W_{4,i} := (1, \xi_i^n)^h, \quad W_{5,ji} := (\xi_i^\phi, \xi_j^n)^h,$$

for the second order tensors corresponding to the bilinear forms in (9), with $i, j = 1, \ldots, N_{POD}$. For the higher order tensors of the polynomial nonlinear forms we for $i, j, k, l, m = 1, \ldots, N_{POD}$ find

$$V_{2,ijkml} := (\xi_i^\phi\xi_j^\phi\xi_k^\phi\mathbf{T}\nabla\xi_l^\Sigma, \nabla\xi_m^\phi), \quad V_{3,ijlk} := (\xi_i^\phi\xi_j^\phi\mathbf{T}\nabla\xi_k^\Sigma, \nabla\xi_l^\phi), \quad V_{4,ikj} := (\xi_i^\phi\mathbf{T}\nabla\xi_j^\Sigma, \nabla\xi_k^\phi),$$

for the mobility term;

$$V_{8,ijkml} := (\chi\xi_i^\phi\xi_j^\phi\xi_k^\phi\mathbf{T}\nabla\xi_l^n, \nabla\xi_m^\phi), \quad V_{9,ijlk} := (\chi\xi_i^\phi\xi_j^\phi\mathbf{T}\nabla\xi_k^n, \nabla\xi_l^\phi), \quad V_{10,ikj} := (\chi\xi_i^\phi\mathbf{T}\nabla\xi_j^n, \nabla\xi_k^\phi),$$

for the chemotactic term;

$$V_{5,ikj} := (\xi_i^\phi\xi_j^n, \xi_k^\phi)^h, \quad V_{6,ijlk} := (\xi_i^\phi\xi_j^\phi\xi_l^n, \xi_k^\phi)^h, \quad V_{7,ijk} := (\xi_i^\phi\xi_j^\phi, \xi_k^\phi)^h,$$

for the source term for ϕ,

$$U_{7,ikj} := (\psi_{1,i}''\xi_j^\phi, \xi_k^\Sigma)^h, \quad U_{3,ikj} := (\xi_i^\phi\xi_j^\phi, \xi_k^\Sigma)^h,$$

for the terms containing ψ_1'' and ψ_2', and

$$W_{3,ikj} := (\xi_i^\phi \xi_j^n, \xi_k^n)^h$$

for the source term for n.

We highlight that it is of utmost importance to assemble the higher order tensors V_2, V_3, V_4 and V_8, V_9, V_{10}, which project the mobility and chemotactic terms onto the ROM space, instead of approximating them through tensor interpolation. The former approach avoids to loose informations about the anisotropy of the tensor of preferential directions $\mathbf{T}$ and the heterogeneity of the chemotactic function χ.

Due to the nonlinearity in the term ψ_1', we solve (15) by means of the Newton method, defining the **ROM Newton** problem:
Problem 5
ROM Newton:

$$(\alpha_{ik}^n, \beta_{ik}^n, \eta_{ik}^n)_{i=1,\ldots,N_{POD};n=0,\ldots,N} = \mathbf{RN}_k^n(\mathbf{A}_k, \mathcal{P}_k, \phi_h^0, n_h^0). \tag{17}$$

The Newton algorithm, which defines the function $\mathbf{RN}_k^n$ is reported in the Appendix. We finally search for the solutions of the nine **ROM linearised** systems obtained from varying $\mathcal{P}_k = \mathcal{P}_k + \delta\mathcal{P}$ in (15), defining
Problem 6
ROM linearised:

$$\nabla_{\mathcal{P}_k} \vec{\alpha}_k = \left[\frac{\partial \vec{\alpha}_k}{\partial L_k} \frac{\partial \vec{\alpha}_k}{\partial \nu_k} \frac{\partial \vec{\alpha}_k}{\partial k_{nk}} \frac{\partial \vec{\alpha}_k}{\partial S_{nk}} \frac{\partial \vec{\alpha}_k}{\partial \delta_{nk}} \frac{\partial \vec{\alpha}_k}{\partial \gamma_k^2} \frac{\partial \vec{\alpha}_k}{\partial E_k} \frac{\partial \vec{\alpha}_k}{\partial \delta_k} \frac{\partial \vec{\alpha}_k}{\partial c_{ek}} \right]^t =$$
$$\mathbf{RL}_k(\mathbf{A}_k, \mathcal{P}_k, (\mathbf{RN}_k^n)_{n=0,\ldots,N}). \tag{18}$$

The construction of the functions $\mathbf{RL}_k$ is reported in the Appendix.

3   Optimisation algorithm

In the following we propose an algorithm to learn the parameters of our model from clinical neuroimaging data. For this purpose we set up a minimisation problem for the model parameters which we solve iteratively with the help of reduced order models aligned with the parameter sets associated to the respective iteration. We refer to [1] where this concept was proposed for optimal flow control using POD surrogate models.

The set of model parameters is given by

$$\mathcal{P} = \{L, \nu, k_n, S_n, \delta_n, \gamma^2, E, \delta, c_e\}.$$

To formulate the parameter learning problem as an optimisation problem we introduce the functional

$$J(\phi(\mathcal{P}), \mathcal{P}) = \frac{1}{2||H(\phi_{\text{data}}(T))||_{L^2(\Omega)}^2} ||H_{\phi_e}(\phi(T)) - H(\phi_{\text{data}}(T))||_{L^2(\Omega)}^2 + \frac{\eta}{2} \sum_{m=1}^{|\mathcal{P}|} \left(\frac{\mathcal{P}_m - \mathcal{P}_{\text{exp,m}}}{\mathcal{P}_{\text{exp,m}}} \right)^2, \tag{19}$$

where ϕ is a solution of the system (1) supplemented with the initial and boundary conditions (3). The set $\mathcal{P}_{\text{exp}}$ contains estimates of expected values for the parameters, η is a regularisation parameter and T is the time at which we compare the simulations and the data tumor extensions. A regularised Heaviside function H_{ϕ_e} with slope $2/\phi_e$ is used to approximate the characteristic function of the tumor extension

$$H_{\phi_e}(\phi) := \begin{cases} 1, & \text{if } \phi \geq \phi_e/2, \\ 2\phi/\phi_e & \text{if } \phi \geq 0 \text{ and } \phi \leq \phi_e/2, \\ 0, & \text{if } \phi \leq 0. \end{cases}$$

This means that we are considering $\phi = \phi_e/2$ as the equation for the hypersurface defining the boundary of the tumour extension, since we can assume that the tumour profile given as a solution of the degenerate Cahn–Hilliard equation (without growth) with the single well cellular potential has a kink–like form between the two equilibria $\phi = 0$ and $\phi = \phi_e$. Finally, $H(\phi_{\text{data}}(T))$ is the characteristic function of the tumour extension from data, computed through the **Target** problem:

Problem 7

Target:

Given MRI(t = 0), determine

$$H(\phi_{data}(T)) = \textbf{Target}(MRI(t = T)), \tag{20}$$

where, given a segmentation map of the tumour extension from MRI(t = T), the function $H(\phi_{data}(T))$ takes the value 1 on the tumour map and the value 0 outside.

The functional J measures the $L^2(\Omega)$ distance between the characteristic functions of the tumor extensions from simulations and data. Note that, due to the fact that we cannot easily obtain informations about the tumor cell densities from the MRI images, we are going to consider the distance between the characteristic functions of the tumor extensions from simulations and data, and not the distance between the tumor distributions.

The value of the functional J calculated at the FOM level is

$$J(\mathbf{F}_{1k}, \mathcal{P}_k) = \frac{1}{2||\pi_h H(\phi_{\text{data}}(T))||_h^2}||\pi_h[H_{\phi_e}(\phi_h^N) - H(\phi_{\text{data}}(T))]||_h^2 + \frac{\eta}{2}\sum_{m=1}^{|\mathcal{P}|}\left(\frac{\mathcal{P}_{k,m} - \mathcal{P}_{\text{exp,m}}}{\mathcal{P}_{\text{exp,m}}}\right)^2, \tag{21}$$

where $||f_h||_h^2 = (f_h, f_h)_h = \{f_h\}^T M_h\{f_h\}$ is the lumped $L^2(\Omega)$ norm, with M_h the lumped mass matrix. We define the following

Problem 8

FOM optimisation problem:

$$\min_{\mathcal{P}_k \in \mathcal{P}_{bio}} J(\mathbf{F}_{1k}, \mathcal{P}_k), \quad \mathbf{F}_k \text{ solution of}(9). \tag{22}$$

Here, $\mathcal{P}_{\text{bio}}$ is the set of biological ranges for each parameter in the set $\mathcal{P}$, as given in Table 1.

In order to solve (22), we will write an iterative algorithm which, given the FOM solution $\mathbf{F}_k$ corresponding to a parameter set $\mathcal{P}_k$ at iteration k, computes the associated **ROM** and **ROM linearised** solutions from **Problem 5** and **Problem 6**, and minimises the functional J at the ROM level through sensitivity analysis, updating the parameter set and initiating a new iteration $k + 1$ until convergence. The value of the functional J calculated at the ROM level is

$$J(\mathbf{RN}_{1k}, \mathcal{P}_k) = \frac{1}{2||\pi_h H(\phi_{\text{data}}(T))||_h^2}\left|\left|\pi_h H_{\phi_e}\left(\sum_{i=1}^{N_{\text{POD}}}\alpha_{ik}^N\xi_i^\phi\right) - \pi_h H(\phi_{\text{data}}(T))\right|\right|_h^2 + \frac{\eta}{2}\sum_{m=1}^{|\mathcal{P}|}\left(\frac{\mathcal{P}_{k,m} - \mathcal{P}_{\text{exp,m}}}{\mathcal{P}_{\text{exp,m}}}\right)^2. \tag{23}$$

In order to calculate a minimum for (23), for $\mathcal{P}_k \in \mathcal{P}_{\text{bio}}$ and with **RN** the solution of (15), we use sensitivity analysis to define a projected gradient algorithm which updates the parameters set along descent directions of the functional J. We define the weighted gradient directions, for each component $m = 1, \ldots, 9$ in the parameter set $\mathcal{P}_k$,

$$\nabla_{\mathcal{P}_k,w}J(\mathbf{RN}_{1k}, \mathcal{P}_k)|_m := \tag{24}$$

$$\left(J_\alpha(\mathbf{RN}_{1k}, \mathcal{P}_k)^T(\mathbf{RL}_{1k}^N\text{diag}[d\mathcal{P}_0])\right)_m^T + \text{diag}[d\mathcal{P}_0]J_{\mathcal{P}_k}(\mathbf{RN}_{1k}, \mathcal{P}_k)|_m = \frac{1}{||\pi_h H(\phi_{\text{data}}(T))||_h^2} \times$$

$$\left[\{\pi_h H_{\phi_e}(\Phi\vec{\alpha}_k^N) - \pi_h H(\phi_{\text{data}}(T))\}^T M_h\left(\text{diag}\left\{\pi_h\frac{\partial H_{\phi_e}}{\partial\Phi\vec{\alpha}_k^N}(\Phi\vec{\alpha}_k^N)\right\}\Phi\left(\frac{\partial\vec{\alpha}_k^N}{\partial\mathcal{P}_{k,m}}d\mathcal{P}_{0,m}\right)\right) + \right.$$

$$\left.\{\pi_h H_{\phi_e}(\Phi\vec{\alpha}_k^N) - \pi_h H(\phi_{\text{data}}(T))\}^T M_h\left\{\pi_h\frac{\partial H_{\phi_e}}{\partial c_{ek}}(\Phi\vec{\alpha}_k^N)dc_{ek,0}\right\}\bigg|_{m=9}\right] + \eta\frac{(\mathcal{P}_{k,m} - \mathcal{P}_{\text{exp,m}})}{\mathcal{P}_{\text{exp,m}}^2}d\mathcal{P}_{0,m},$$

where

$$dP_0 := 10^{-n_w}P_0, \ n_w \in \mathbb{N}_+,$$

is the vector of weights, which defines a weighted Euclidean scalar product in the parameter space. M_h denotes the lumped scalar mass matrix. We note that the weighted gradient (24) can be obtained in an equivalent way using the standard Euclidean inner product in parameter space and solving the linearised problems (18) at P_k for a definite variation $P_k + dP_0$.

Then, we define the projection function

$$P_k(\lambda) := \max(P_{\text{bio,min}}, \min(P_{\text{bio,max}}, P_k - \lambda \nabla_{P_k, w} J(\mathbf{RN}_{1k}, P_k))),$$

which updates the values of the parameters P_k along the weighted gradient directions with a learning rate λ and projects them onto the feasible set.

Following [27], we define the

Problem 9

Projected Weighted Gradient Algorithm: *Given **RN**, **RL**, P_k, we update*

a: *Given $\beta < 1$ and $\lambda = \beta$, compute $P_k(\lambda)$.*
b: *Find the least integer m such that $\lambda_k = \beta^m$ and*

$$J(\mathbf{RN}(P_k(\lambda_k)), P_k(\lambda_k)) - J(\mathbf{RN}_{1k}, P_k) \leq \frac{-10^{-4}}{\lambda_k}|P_k(\lambda_k) - P_k|^2;$$

c:

$$P_{k+1} = \mathbf{PWG}(\mathbf{RN}_k, \mathbf{RL}_k, P_k) := P_k(\lambda_k). \tag{25}$$

We finally formulate the following **Optimization algorithm**:

Algorithm 1 Optimization Algorithm

Require: MRI(t=0), DTI(t=0), MRI(t=T), $\mathcal{P}_0, \mathcal{P}_{\text{bio}}, \mathcal{P}_{\text{av}}$;

  Initialisation(MRI(t=0), DTI(t=0)) (Problem (7));

  Target(MRI(t=T)) (Problem (20));

  for $k \geq 0$ **do**

    Step 1–FOM: $\mathbf{F}_k(\textbf{Initialisation}, \mathcal{P}_k)$ (Problem (8));

    Compute $J(\mathbf{F}_{1k}, \mathcal{P}_k)$;

    if $k \geq 1$ **and** $J((\mathbf{F}_{1k}, \mathcal{P}_k) \geq J((\mathbf{F}_{1k-1}, \mathcal{P}_{k-1})$ **then**

      $\mathcal{P}_{\text{opt}} \leftarrow \mathcal{P}_{k-1}$;

      break;

    else if $k \geq 1$ **and** $|J(\mathbf{F}_{1k}, \mathcal{P}_k) - J(\mathbf{F}_{1k-1}, \mathcal{P}_{k-1})| \leq \text{tol}_F |J(\mathbf{F}_{11}, \mathcal{P}_1) - J(\mathbf{F}_{10}, \mathcal{P}_0)|$ **then**

      $\mathcal{P}_{\text{opt}} \leftarrow \mathcal{P}_k$;

      break;

    Step 2–POD: $\mathbf{P}_k(\mathbf{F}_k)$ (problem (11));

    Step 3–Assemble the ROM systems: $\mathbf{A}_k(\mathbf{P}_k)$ (problem (16));

    Step 4–ROM Optimization:

    for $l \geq 0$ **do**

      $\mathcal{P}_l \leftarrow \mathcal{P}_k$,

      Step A: $\mathbf{RN}_l(\mathbf{A}_l, \mathcal{P}_l, \phi_h^0, n_h^0)$; $\mathbf{RL}_l(\mathbf{A}_l, \mathcal{P}_l, \mathbf{RN}_l)$ (problems (17),(18));

      Step B Compute $J(\mathbf{RN}_{1l}, \mathcal{P}_l)$;

      Step C: $\mathcal{P}_{l+1} = \mathbf{PWG}(\mathbf{RN}_l, \mathbf{RL}_l, \mathcal{P}_l)$ (problem (25));

      if $\max_{i=1,\ldots,|\mathcal{P}|}\left((\mathcal{P}_{i,l+1} - \mathcal{P}_{i,l})/\mathcal{P}_{i,l} \right) \leq \text{tol}_{Ra}$ **and**

$|J(\mathbf{RN}_{1l+1}, \mathcal{P}_{l+1}) - J(\mathbf{RN}_{1l}, \mathcal{P}_l)| \leq \text{tol}_{Rb}|J(\mathbf{RN}_{11}, \mathcal{P}_1) - J(\mathbf{RN}_{10}, \mathcal{P}_0)|$**and**

$|\mathcal{P}_{l+1}(1) - \mathcal{P}_{l+1}| \leq \text{tol}_{Pa}|\mathcal{P}_0| + \text{tol}_{Pr}|\mathcal{P}_0(1) - \mathcal{P}_0|$ **then**

        $\mathcal{P}_{k+1} \leftarrow \mathcal{P}_{l+1}$;

        break.

The Algorithm 1 stops at an iteration k when the functional J, calculated at the **FOM** level, decreases, with respect to its value at $k-1$, by an amount which is a sufficiently small fraction of the initial decrease between iteration 1 and 0, which means that a local minimum is being approached. In the same way, the projected gradient iterations stop at an iteration l when the following termination criteria are simultaneously satisfied: the functional J, calculated at the **ROM** level, decreases of a sufficiently small amount with respect to the initial decrease attained at the first iteration, the parameters are changing by a relative small amount along the descent directions and the Euclidean norm of $\mathcal{P}_l(1) - \mathcal{P}_l$, which is a measure of stationarity related to the magnitude of the weighted gradient of J, is sufficiently small with respect to the norm of $\mathcal{P}_0$ and the initial norm of $\mathcal{P}_0(1) - \mathcal{P}_0$. After **Step 4**, we go back to **Step 1** and calculate the new POD basis associated to the FOM solutions obtained with the new set of parameters $\mathcal{P}_{l+1}$. We thus dynamically span the space of parameters by solving the optimization algorithm over ROM systems associated to different POD bases for each set $\mathcal{P}_k$ at each step k. This is indeed an alternative way to consider parameters variability in the MOR of evolution equations with respect to the local reduced basis method used e.g. in [35], which would request the static computation by k-means clustering of different local POD basis from FOM solutions performed for different sets of parameters, performing the minimisation problem on a ROM level by choosing properly the local basis along the flow of projected gradient parameter updates.

We finally observe that the weights in (24) are needed to precondition the ill–conditioned gradient projected algorithm (25). Indeed, due to the large differences in the order of magnitude of the parameters in the set $\mathcal{P}$ (see Table 1), the solutions of the linearised systems (18)

differ accordingly (higher linearised solutions for smaller parameters) by order of magnitudes and some parameters may undergo large variations during the first step of the Armijo procedure in **Problem 9**. These variations could not be fully represented by the information contained in the starting POD basis, which is based on FOM solutions which satisfy the physical constraints, thus causing the Newton algorithm to compute $\mathbf{RN}(\mathcal{P}_k(\beta)))$ to diverge and the solution to violate the physical constraints. The latter fact happens when the negative values associated to the higher order POD basis are amplified during the algorithm. An alternative way to proceed would be to regularise the ROM system in order to eliminate its instability when the ROM solutions take values in an unphysical range and to penalise unphysical solutions, by choosing a convex potential containing a smooth penalisation of negative values. This method was found to be unnecessary when weights are introduced in (24).

4 Results

In this section we apply the proposed algorithm to optimise the parameter estimation from the neuroimaging data of two test cases provided by a clinical study conducted at the Istituto Neurologico Besta in Milan. Test case 1 is a clinical follow-up of a primary tumour subjected to adjuvant therapy, optimising the model parameters by following-up the tumour growth until surgical removal. Test case 2 concerns the recurrence pattern of a GBM after surgery until the start of radiotherapy. While in the first case the tumour mass keeps a round shape, in the latter it grows in an irregular manner infiltrating the peritumoral brain tissue after surgery.

Since the biological range of the model parameters to be estimated can vary as summarised in Table 1, we use as our initial guess for the optimisation algorithm the manually tuned parameters in [2, 3], reading

$$\mathcal{P}_0 \equiv \{(1/5000), (0.08), (2.0), (10^4), (8640), (0.1225), (694), (0.3), (0.611)\},$$
$$\mathcal{P}_{\text{bio}} \equiv \{[1/5032.2, 1/1377.86], [0.012, 0.5], [0.007, 90.72], [10^3, 10^5], [10^3, 10^5],$$
$$[0.0841, 0.6084], [106.66, 1533.3], [0.1, 0.33], [0.2, 0.611]\},$$
$$\mathcal{P}_{\text{exp}} \equiv \{(1/3991.06), (0.06), (2.0), (10^4), (8640), (0.1225), (694), (0.3), (0.611)\}, \qquad (26)$$

with units $mm^2/(\text{Pa}\,\text{day})$, day^{-1}, mm^2/day, day^{-1}, day^{-1}, $\text{Pa}\,mm^2$ and Pa for the first seven parameters respectively, whereas δ and c_e are dimensionless. Moreover, we set $\eta = 10^{-4}$, $\text{tol}_F = \text{tol}_{Ra} = \text{tol}_{Rb} = \text{tol}_{Pr} = 10^{-3}$, $\text{tol}_{Pa} = 10^{-6}$, $n_w = 1$.

4.1 Test case 1: clinical follow-up of a primary tumour

We first apply the proposed Optimization Algorithm for a test case which investigates the clinical follow-up of a primary tumour.
A patient diagnosed with multiple GBM lesions underwent a surgical removal, which left one posterior temporal mass untouched. The patient started radiotherapy with concomitant chemotherapy (Temozolomide) 25 days after surgery following the Stupp protocol; the pre-Radiotherapy MRI confirmed the presence of the primary GBM mass in the posterior temporal area. The patient completed the standard radiation protocol, and performed post-radiotherapy MRI immediately after the treatment and then every two months. These MRI scans depict the progression of the posterior temporal lesion. Further 6 MRI scans were taken on following the schedule of the clinical protocol until a post-radiotherapy stage at 8 months after surgery. Our numerical simulations investigate the follow-up of the growing posterior lesion from 6 months after surgery (initial time $t = 0$ days in the simulations) to 8 months after surgery (final time $t = T := 2$ months). At $t = T$ we compare data and simulations, searching for the optimal set of parameters $\mathcal{P}_{\text{opt}}$ which locally minimises the functional (19), obtained by solving **Algorithm 1**. Between $t = 0$ and $t = 2$ months the

patient underwent two chemotherapy cycles, so that

$$K_T(t) = \begin{cases} K_{C_3} & 0 \leq t \leq 8, \quad 33 \leq t \leq 38 \text{ [days]}, \\ 0 & \text{otherwise.} \end{cases}$$

In Figure 1 we show the axial, sagittal and coronal slices of the T1-weighted MRI at different temporal stages. The clinicians observed that at $t = 4$ months (10 months after surgery), the posterior lesion joins the infiltrated mass re–grown from the peritumoral area affected by surgery. Therefore, we choose to set the optimization problem only between $t = 0$ and $t = 2$ months, when the posterior lesion can be considered as a single tumour mass expanding in a healthy brain tissue.

4.1.1 Initialisation

In Figures 2 and 3 we represent the results of the **initialisation** step of **Algorithm 1**, which defines the domain Ω (Figure 2), the map(WM,GM,CSF), the initial condition ϕ_h^0 and the tensors $\mathbf{D}$ and $\mathbf{T}$ (Figure 3), extracted from the segmentation of the MR images and from the study of the log-signal associated to the DTI at $t = 0$.

The number of elements and the number of nodes of the mesh $\mathcal{T}_h$ are 301867 and 50713 respectively. Moreover, we choose $\Delta T = 0.1225$ (days), and $N = 490$.
The characteristic function of the tumour extension $\phi_{\text{data}}(T)$ has been extracted from the segmentation of the MR images at $t = 2$ month.

4.1.2 Step 1

In Figure 4 we report the values of the functional $J(\phi_h^N(\mathcal{P}_k), \mathcal{P}_k)$, calculated in **step 1** of **Algorithm 1**, and of the set of parameters $\mathcal{P}_k$, for different values of k. We also plot the iso–surfaces $\phi_{\text{data}}(T) = 0$ from the MRI data and $\phi_h^N(\mathcal{P}_k) = \phi_e/2$ from the FOM simulations, reporting the value of the Jaccard index, defined as the intersection over union ratio between the two volumes enclosed within these two surfaces.
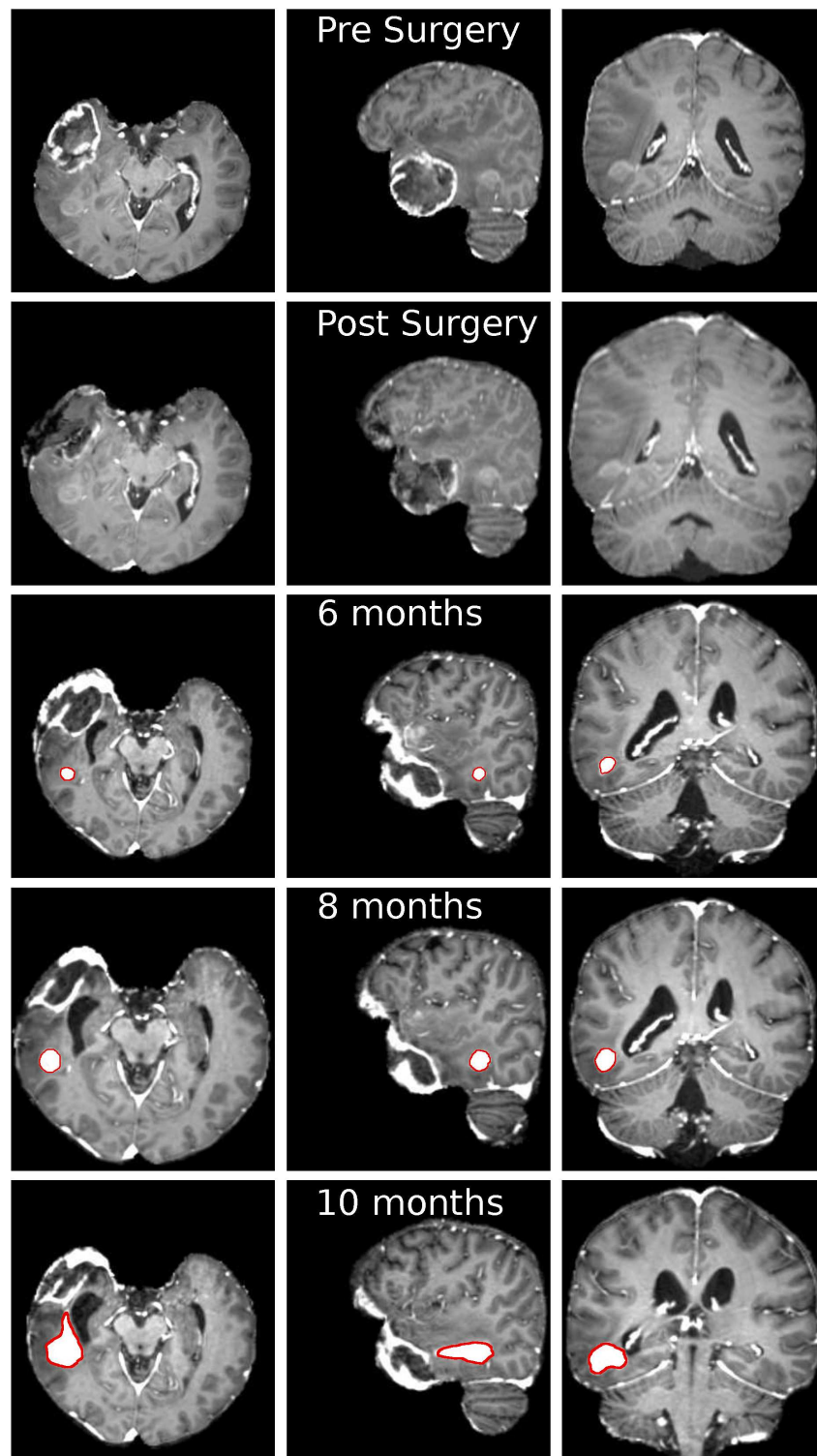
Figure 1: Axial (first column), sagittal (second column) and coronal (third column) slices of the T1-weighted MRI at different temporal stages. First row: before surgery; second raw: after surgery; third row: 6 months after surgery; fourth row: 8 months after surgery; fifth row: 10 months after surgery. It is possible to appreciate the progressive volumetric increase of the posterior temporal mass. The segmented boundary of the tumour is highlighted in red color.
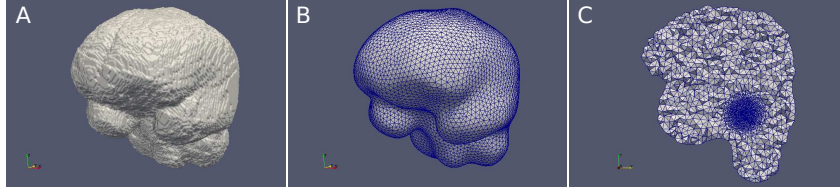
Figure 2: (A) External brain surface extracted from the medical images; (B) Smoothed and re–meshed external surface; (C) Tetrahedral mesh generated within the external surface, conveniently refined in the peritumoral area.
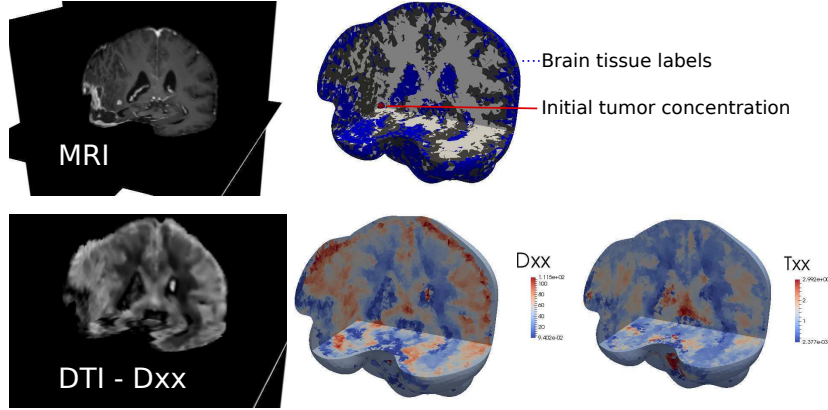

Figure 3: 3D virtual reconstructions of the MRI (top) and DTI (bottom) data, with the corresponding computational meshes containing the labels of the brain tissues and the xx component of the tensors $\mathbf{D}$ and $\mathbf{T}$. White matter, grey matter and CSF are highlighted in white, grey and blue colors respectively. The initial tumour distribution is also highlighted in brown color, as segmented from the T1-weighted MRI.

The **Algorithm 1** stops at $k = 2$, since

$$J(\phi_h^N(\mathcal{P}_{k+1}), \mathcal{P}_{k+1}) = J(\phi_h^N(\mathcal{P}_k), \mathcal{P}_k)$$

for $k = 2$. Indeed, the ROM optimization algorithm for $k = 2$ makes no advances in the parameter space (see Figure 7). We thus identify

$$\mathcal{P}_{\text{opt}} \equiv \mathcal{P}_2 =$$
$$\{L = 0.0002, \nu = 0.0213, k_n = 1.9842, S_n = 10000.04, \delta_n = 8639.95, \gamma^2 = 0.1225,$$
$$E = 693.99, \delta = 0.3271, c_e = 0.611\}, \tag{27}$$

with the corresponding units. We observe that during the optimization process at different k levels the overall overlapping between the tumour extensions from FOM simulations and from data is increasing, which is shown by the corresponding increase in the value of the Jaccard index.

4.1.3 Step 2

In Table 2 we report, for each step k of **Algorithm 1**, the values of the cumulated fractions of $\text{tr}\mathbf{F}_1^T\mathbf{F}_1, \text{tr}\mathbf{F}_2^T\mathbf{F}_2, \text{tr}\mathbf{F}_3^T\mathbf{F}_3, \text{tr}(\psi_1'(\mathbf{F}_1))^T\psi_1'(\mathbf{F}_1), \text{tr}(\psi_1''(\mathbf{F}_1))^T\psi_1''(\mathbf{F}_1)$ associated to the eigenvalues of the corresponding matrices, arranging them starting from the eigenvalue with the highest magnitude and following a decreasing order.
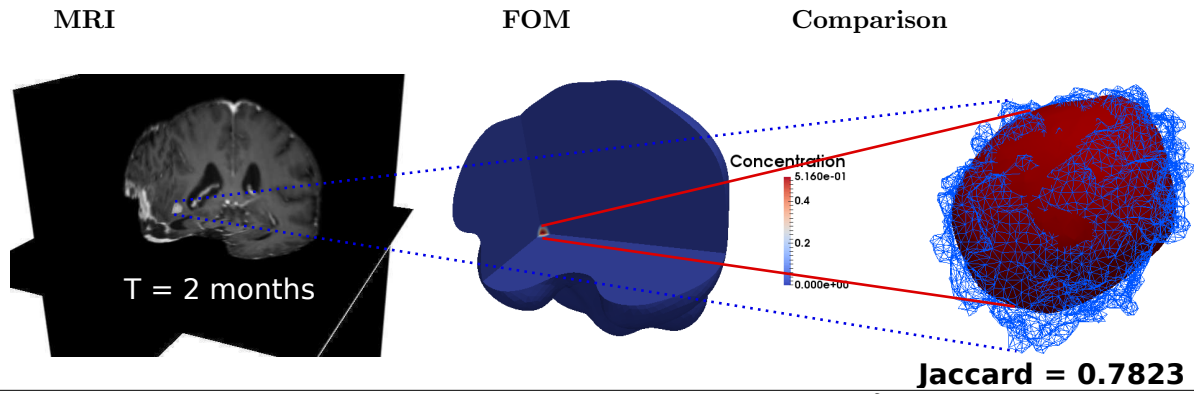We thus have that $N_{\text{POD}} = N_\phi^{\text{POD}} = 5$ for $k = 0$ and $N_{\text{POD}} = N_\phi^{\text{POD}} = 4$ for $k = 1, 2$. In Figure 5 we show the basis elements ξ_i^ϕ, corresponding to the highest eigenvalues needed to

16

Iteration	$\mathbf{J}(\mathcal{P}_0)$	$\mathbf{L}_0$	$\boldsymbol{\nu}_0$	$\mathbf{k}_{n0}$	$\mathbf{S}_{n0}$	$\boldsymbol{\delta}_{n0}$	γ_0^2	$\mathbf{E}_0$	$\boldsymbol{\delta}_0$	$\mathbf{c}_{e0}$
k=0	0.32328	0.0002	0.08	2	10000	8640	0.1225	694	0.3	0.611
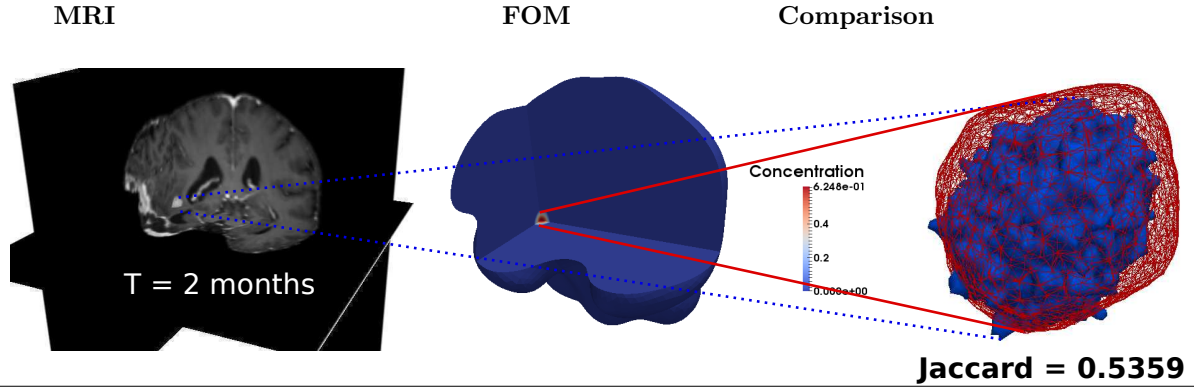
Iteration	$\mathbf{J}(\mathcal{P}_1)$	$\mathbf{L}_1$	$\boldsymbol{\nu}_1$	$\mathbf{k}_{n1}$	$\mathbf{S}_{n1}$	$\boldsymbol{\delta}_{n1}$	γ_1^2	$\mathbf{E}_1$	$\boldsymbol{\delta}_0$	$\mathbf{c}_{e0}$
k=1	0.08001	0.0002	0.02352	1.9769	9999.99	8640.00	0.1225	693.99	0.3237	0.5755

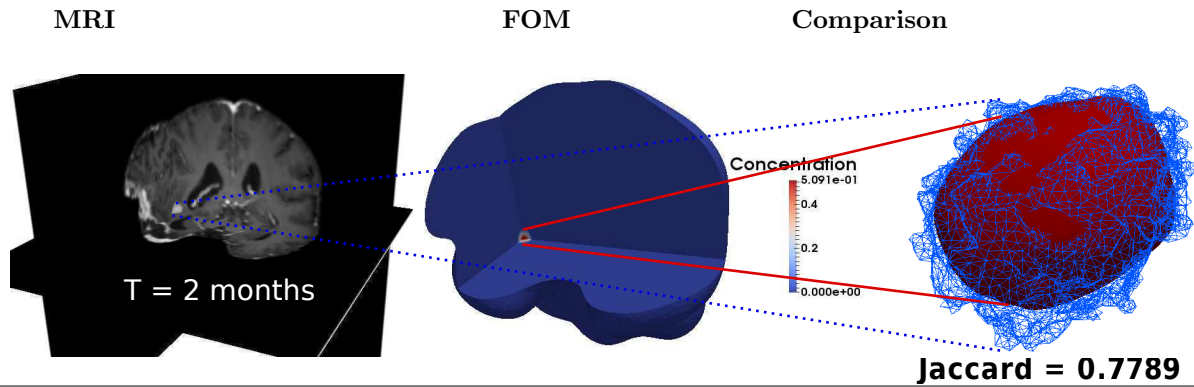| Iteration	$\mathbf{J}(\mathcal{P}_2)$	$\mathbf{L}_2$	$\boldsymbol{\nu}_2$	$\mathbf{k}_{n2}$	$\mathbf{S}_{n2}$	$\boldsymbol{\delta}_{n2}$	γ_2^2	$\mathbf{E}_2$	$\boldsymbol{\delta}_0$	$\mathbf{c}_{e0}$
k=2	0.07167	0.0002	0.0213	1.9842	10000.04	8639.95	0.1225	693.99	0.3271	0.611

Figure 4: Values of $J(\phi_h^N(\mathcal{P}_k), \mathcal{P}_k)$ and of $\mathcal{P}_k$ for different iteration steps k of **Algorithm 1**, with a comparison between the isosurfaces $\phi_{\mathrm{data}}(T) = 0$ (highlighted in blue color) and $\phi_h^N(\mathcal{P}_k) = \phi_e/2$ (highlighted in red color).

explain the 99.99% variance of the data, for $k = 0, 1$, superposed with the initial condition and final distribution of cell concentration (highlighted by a distribution of green and red points respectively). We observe that ξ_1^ϕ and ξ_2^ϕ are distributed over the bulk of the final state ϕ_h^N and the initial condition ϕ_h^0 respectively, whereas ξ_3^ϕ, ξ_4^ϕ and ξ_5^ϕ are oscillating functions over the set where the tumour is expanding during its temporal evolution, and

Table 2: Values of the cumulated fraction of $\mathrm{tr}\mathbf{F}_1^T\mathbf{F}_1$, $\mathrm{tr}\mathbf{F}_2^T\mathbf{F}_2$, $\mathrm{tr}\mathbf{F}_3^T\mathbf{F}_3$, $\mathrm{tr}(\psi_1'(\mathbf{F}_1))^T\psi_1'(\mathbf{F}_1)$, $\mathrm{tr}(\psi_1''(\mathbf{F}_1))^T\psi_1''(\mathbf{F}_1)$ for the first eigenvalues with the highest magnitude.

| Iteration k=0	Eigenvalue	% $\mathrm{tr}\mathbf{F}_1^T\mathbf{F}_1$	% $\mathrm{tr}\mathbf{F}_2^T\mathbf{F}_2$	% $\mathrm{tr}\mathbf{F}_3^T\mathbf{F}_3$	% $\mathrm{tr}(\psi_1')^T\psi_1'$	% $\mathrm{tr}(\psi_1'')^T\psi_1''$
	First	95.1394	99.9195	99.9695	99.9098	99.3874
	Second	99.4332	99.9868	99.9964	99.9778	99.8069
	Third	99.8773	99.9970	99.9991	99.9950	99.9483
	Fourth	99.9695	99.9986	99.9996	99.9983	99.9882
	Fifth	99.9912	99.9997	99.9999	99.9997	99.9980
Iteration k=1	Eigenvalue	% $\mathrm{tr}\mathbf{F}_1^T\mathbf{F}_1$	% $\mathrm{tr}\mathbf{F}_2^T\mathbf{F}_2$	% $\mathrm{tr}\mathbf{F}_3^T\mathbf{F}_3$	% $\mathrm{tr}(\psi_1')^T\psi_1'$	% $\mathrm{tr}(\psi_1'')^T\psi_1''$
	First	97.6975	99.9483	99.9891	99.9133	99.0374
	Second	99.6790	99.9950	99.9987	99.9932	99.9278
	Third	99.9524	99.9989	99.9997	99.9985	99.9849
	Fourth	99.9912	99.9996	99.9998	99.9996	99.9971
Iteration k=2	Eigenvalue	% $\mathrm{tr}\mathbf{F}_1^T\mathbf{F}_1$	% $\mathrm{tr}\mathbf{F}_2^T\mathbf{F}_2$	% $\mathrm{tr}\mathbf{F}_3^T\mathbf{F}_3$	% $\mathrm{tr}(\psi_1')^T\psi_1'$	% $\mathrm{tr}(\psi_1'')^T\psi_1''$
	First	97.7632	99.9500	99.9890	99.9105	99.0029
	Second	99.6881	99.9953	99.9988	99.9933	99.9280
	Third	99.9542	99.9990	99.9997	99.9986	99.9855
	Fourth	99.9917	99.9997	99.9999	99.9996	99.9973

thus contain the information about the tumour boundary and its expansion.

We observe that the number of basis functions needed to explain the 99.99% variance of the data is small, which depends on the fact that the region of tumour expansion small and there are no significant topological changes in the evolution dynamics of the FOM solution, which also spreads in a smooth manner. In order to deal with a sufficiently smooth FOM dynamics we needed to choose a mesh $\mathcal{T}_h$ sufficiently refined in the region of tumour evolution. This turned out to be necessary in order to deal with low dimensional higher order tensors in **Problem 4** (16) and to deal with ROM systems which are solvable with low computational resources and in highly reduced computational times.
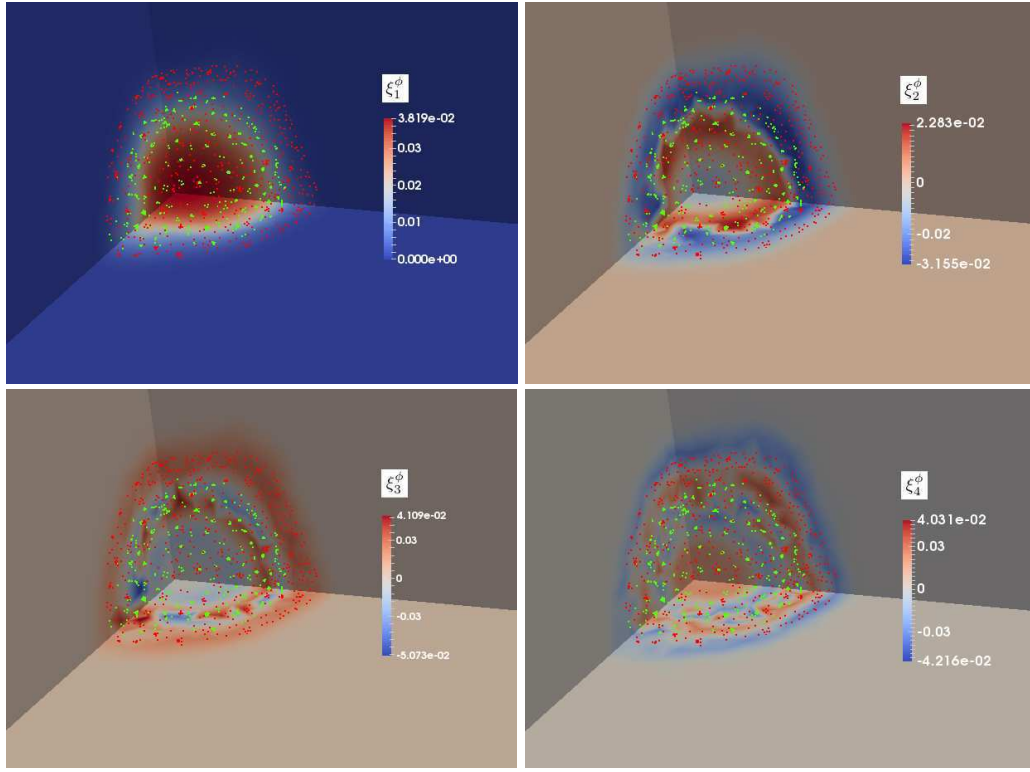
Iteration k=0
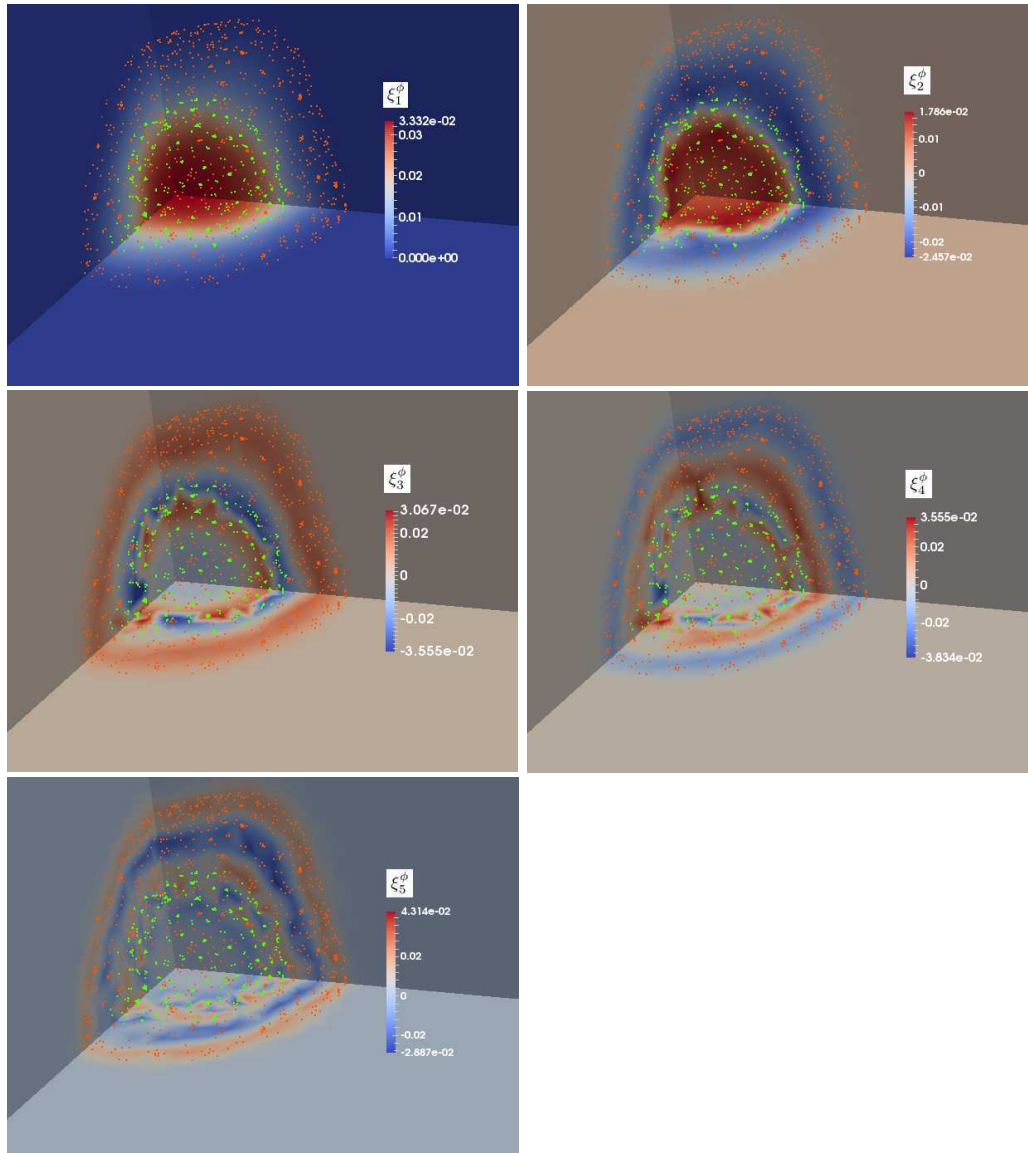
Figure 5: Plot of the basis elements ξ_i^ϕ corresponding to the highest eigenvalues needed to explain the 99.99% variance of the data, for $k = 0, 1$. Green and red points are distributed over the initial condition and final distribution of cell concentration, respectively.

We finally show in Figure 6 a comparison between the final state ϕ_h^N calculated from the FOM simulation through **Algorithm 2** with parameter set $\mathcal{P}_0$ and the corresponding final state $\sum_{i=1}^{N_{\mathrm{POD}}} \alpha_{i0}^N \xi_i^\phi$ obtained as a solution of the ROM system (15) through **Algorithm 4**.
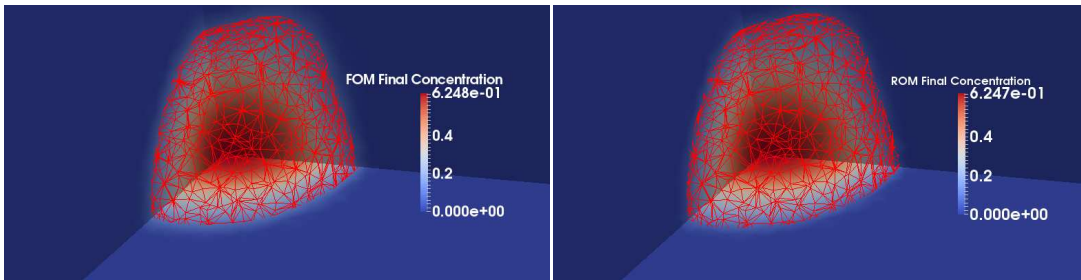

Figure 6: Comparison between the final state ϕ_h^N, solution of the FOM simulation with parameter set $\mathcal{P}_0$ and the corresponding final state $\sum_{i=1}^{N_{\mathrm{POD}}} \alpha_{i0}^N \xi_i^\phi$, solution of the ROM system (15). The iso–surfaces $\phi_h^N = \phi_e/2$ and $\sum_{i=1}^{N_{\mathrm{POD}}} \alpha_{i0}^N \xi_i^\phi = \phi_e/2$ are highlighted in red colors.

We observe that the ROM solution is approximating the FOM solution with a very high fidelity.

4.1.4   Steps 3 and 4

In Figure 7 we report the values of the functional $J(\vec{\alpha}_l, \mathcal{P}_l)$, of the normalised set of parameters
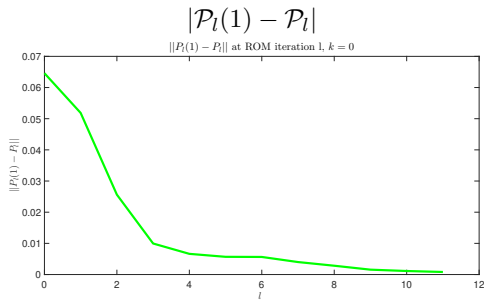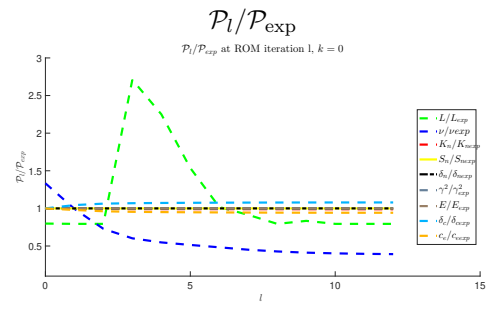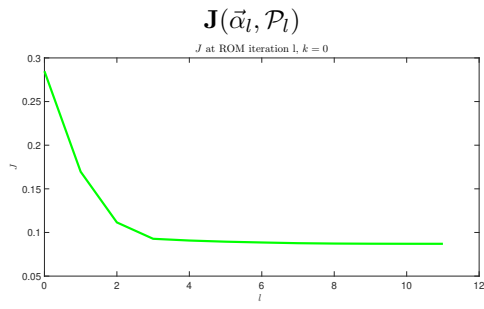
$$\mathcal{P}_l/\mathcal{P}_{\exp} = \{L_l/L_{\exp}, \nu_l/\nu_{\exp}, k_{nl}/k_{n\exp}, S_{nl}/S_{n\exp}, \delta_{nl}/\delta_{n\exp}, \gamma_l^2/\gamma_{\exp}^2, E_l/E_{\exp}, \delta_c/\delta_{c\exp}, c_e/c_{ee\exp}\},$$

and of $|\mathcal{P}_l(1) - \mathcal{P}_l|$, computed in **Steps 3** and **4** of **Algorithm 1**, for $k = 0, 1, 2$. We also plot the iso–surfaces $\phi_{\text{data}}(T) = 0$ from the MRI data and $\sum_{i=1}^{N_{\text{POD}}} \alpha_{i\bar{l}}^N \xi_i^\phi = \phi_e/2$ from the ROM simulations, where $\bar{l}$ is the number of the last iteration of **Step 4**, reporting the value of the Jaccard index between the two volumes enclosed by these surfaces.

For $k = 0$ the ROM optimization process in **Steps 3** and **4** goes through 11 steps before matching the termination conditions. We also observe that only the model parameters L, ν, δ, c_e change significantly from their starting values during the optimization process, being the system quite insensitive to changes of the remaining parameters $k_n, S_n, \delta_n, \gamma^2, E$. The proliferation rate ν is the most sensitive parameter whose variations lead to the functional minimisation. This is in accordance to the sensitivity analysis found in the literature for tumour growth models based on Cahn–Hilliard–Darcy–Forchheimer–Brinkman equations with logistic growth [18].

For $k = 1$ the ROM optimization process in **Steps 3** and **4** goes through 45 steps. Finally, for $k = 2$ the ROM optimization process is making no progress.
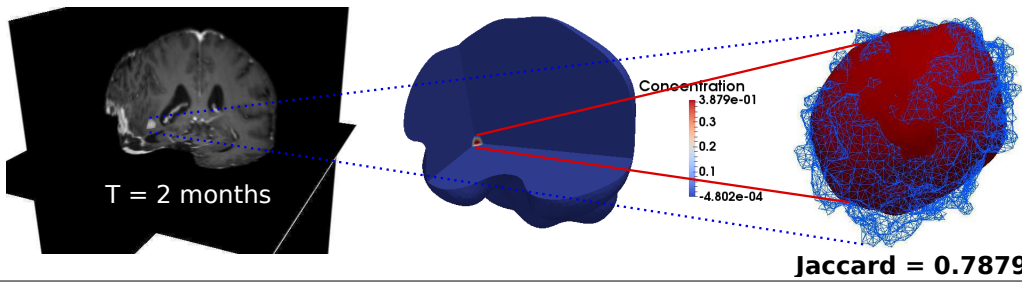
J$(\vec{\alpha}_l, \mathcal{P}_l)$

$\mathcal{P}_l/\mathcal{P}_{\exp}$

$|\mathcal{P}_l(1) - \mathcal{P}_l|$

MRI	ROM $(\mathcal{P}_{\bar{l}=11})$	Comparison

T = 2 months

Jaccard = 0.7879

J$(\vec{\alpha}_l, \mathcal{P}_l)$

$\mathcal{P}_l/\mathcal{P}_0$
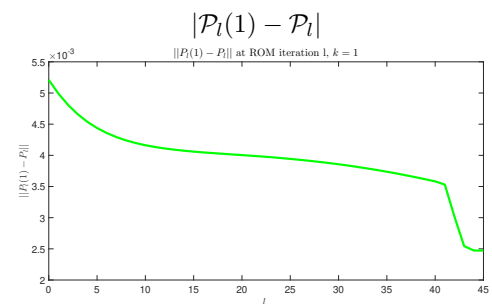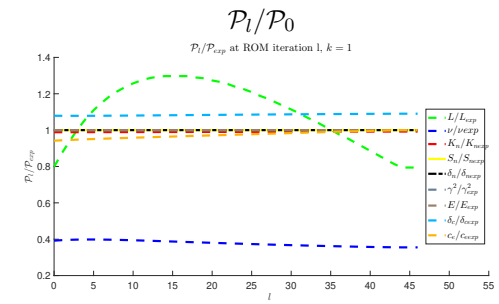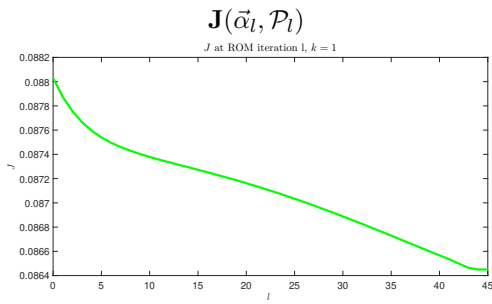
$|\mathcal{P}_l(1) - \mathcal{P}_l|$

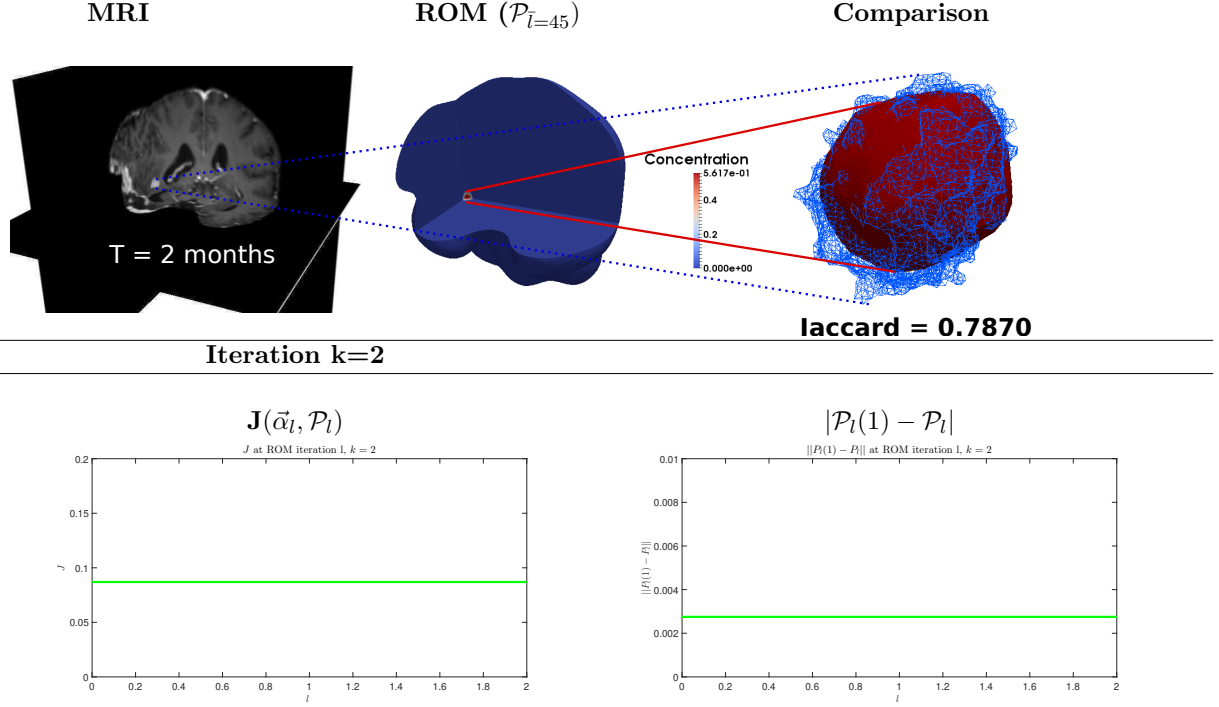Figure 7: Values of the functional $J(\vec{\alpha}_l, \mathcal{P}_l)$, of the normalised set of parameters $\mathcal{P}_l/\mathcal{P}_{\exp}$ and of $|\mathcal{P}_l(1) - \mathcal{P}_l|$ for steps $k = 0, 1, 2$ of **Algorithm 1**, together with a comparison between the isosurfaces $\phi_{\text{data}}(T) = 0$ (highlighted in blue color) and $\sum_{i=1}^{N_{\text{POD}}} \alpha_{i\bar{l}}^N \xi_i^\phi = \phi_e/2$ (highlighted in red color).

4.1.5   Computational cost

We conclude by reporting in Table 3 the elapsed time (in seconds) for the computation of steps $1 - 4$ of **Algorithm 1** for the different values of the iteration step k. We observe

Table 3: Elapsed time (in seconds) for the computation of steps $1 - 4$, for the different values of the iteration step k.

Iteration	Step 1	Step 2	Step 3	Step 4
k=0	201914.27	12.42	6281.31	157.8289
Iteration	**Step 1**	**Step 2**	**Step 3**	**Step 4**
k=1	201425.71	12.89	2600.37	587.07
Iteration	**Step 1**	**Step 2**	**Step 3**	**Step 4**
k=2	213040.53	11.44	2544.43	42.53

that the computational time for the projected gradient iterations at the ROM level is 3 to 4 order of magnitude smaller than the time needed to solve the FOM problem. We thus can very efficiently minimise the functional J at the ROM level, checking at the FOM level the effective functional decrease and updating the POD basis to span the parameters space. In order to have light ROM systems, we need to have higher order tensors in **Problem 4**

(16) with low dimension. Indeed, with only 4 or 5 basis functions **Step 3** of Algorithm (1) requires a heavy computational cost, which is only 2 orders of magnitude smaller than the time needed to solve the FOM problem.

4.1.6 Some remarks on benchmark results

In this paragraph we report some numerical results to show how the POD analysis in **Step 2** of Algorithm (1) varies when the tumour concentration in the FOM simulations in **Step 1** is spreading on a larger region than the one observed in Test Case 1. This happens if we consider a tumour dynamics over a larger time interval and also if we consider an initial set of parameters which induces a larger and more anisotropic tumour expansion. Moreover, we report numerical results about the performance of **Step 4** of Algorithm (1) when a different initial set of parameter is considered and when a lower threshold of POD significance (namely 99.9%) is considered.

In Table 4 we report the POD analysis of the snapshot matrices obtained from the FOM solution (8) at $k = 0$ of **Algorithm 1** with $N = 980$, i.e. when the tumour dynamics span a time interval of 120 days.

Table 4: Values of the cumulated fraction of $\mathrm{tr}\mathbf{F}_1^T\mathbf{F}_1, \mathrm{tr}\mathbf{F}_2^T\mathbf{F}_2, \mathrm{tr}\mathbf{F}_3^T\mathbf{F}_3, \mathrm{tr}(\psi_1'(\mathbf{F}_1))^T\psi_1'(\mathbf{F}_1), \mathrm{tr}(\psi_1''(\mathbf{F}_1))^T\psi_1'(\mathbf{F}_1)$ for the first eigenvalues with the highest magnitude.

Iteration k=0 N = 980	Eigenvalue	% $\mathrm{tr}\mathbf{F}_1^T\mathbf{F}_1$	% $\mathrm{tr}\mathbf{F}_2^T\mathbf{F}_2$	% $\mathrm{tr}\mathbf{F}_3^T\mathbf{F}_3$	% $\mathrm{tr}(\psi_1')^T\psi_1'$	% $\mathrm{tr}(\psi_1'')^T\psi_1''$
	First	90.2061	99.6130	99.8455	99.5709	97.7895
	Second	98.5523	99.8068	99.9859	99.9554	99.6662
	Third	99.5893	99.9866	99.9958	99.9836	99.8917
	Fourth	99.8472	99.9967	99.9982	99.9928	99.9446
	Fifth	99.9401	99.9989	99.9992	99.9968	99.9805
	Sixth	99.9744	99.9995	99.9995	99.9987	99.9941
	Seventh	99.9884	99.9998	99.9998	99.9995	99.9978
	Eighth	99.9944	99.9999	99.9999	99.9998	99.9991

We thus have that $N_{\mathrm{POD}} = N_\phi^{\mathrm{POD}} = 8$ for $k = 0$.

In Table 5 we report the same POD analysis for a time span of 120 days, choosing also an initial set of parameters

$$\mathcal{P}_0^{\mathrm{bis}} \equiv \{(1/3205.13), (0.128), (3.00), (9 * 10^3), (6184), (0.2862), (819.98), (0.215), (0.3364)\};$$

in order to observe a larger and more anisotropic spread of the initial tumour distribution during the dynamics.

We thus have that $N_{\mathrm{POD}} = N_\phi^{\mathrm{POD}} = 10$ for $k = 0$.

In Figure 8 we also show the basis elements ξ_i^ϕ, corresponding to the highest eigenvalues needed to explain the 99.99% variance of the data, for the case of $N = 980$ and initial set $\mathcal{P}_0^{\mathrm{bis}}$, superposed with the initial condition and final distribution of cell concentration (highlighted by a distribution of green and red points respectively).

Table 5: Values of the cumulated fraction of $\mathrm{tr}\mathbf{F}_1^T\mathbf{F}_1$, $\mathrm{tr}\mathbf{F}_2^T\mathbf{F}_2$, $\mathrm{tr}\mathbf{F}_3^T\mathbf{F}_3$, $\mathrm{tr}(\psi_1'(\mathbf{F}_1))^T\psi_1'(\mathbf{F}_1)$, $\mathrm{tr}(\psi_1''(\mathbf{F}_1))^T\psi_1''(\mathbf{F}_1)$ for the first eigenvalues with the highest magnitude.

Iteration $k=0$ $N = 980$ $\mathcal{P}_0^{\mathrm{bis}}$	Eigenvalue	% $\mathrm{tr}\mathbf{F}_1^T\mathbf{F}_1$	% $\mathrm{tr}\mathbf{F}_2^T\mathbf{F}_2$	% $\mathrm{tr}\mathbf{F}_3^T\mathbf{F}_3$	% $\mathrm{tr}(\psi_1')^T\psi_1'$	% $\mathrm{tr}(\psi_1'')^T\psi_1''$
	First	89.5942	96.9529	99.2853	97.0274	93.7024
	Second	97.6348	97.8125	99.9235	99.7625	99.3436
	Third	99.3231	99.7177	99.9817	99.9318	99.7444
	Fourth	99.7375	99.9534	99.9927	99.9631	99.8768
	Fifth	99.8762	99.9866	99.9962	99.9850	99.9567
	Sixth	99.9370	99.9944	99.9978	99.9930	99.9849
	Seventh	99.9670	99.9975	99.9988	99.9969	99.9945
	Eighth	99.9821	99.9987	99.9992	99.9986	99.9974
	Nineth	99.9899	99.9993	99.9996	99.9992	99.9985
	Tenth	99.9942	99.9996	99.9997	99.9996	99.9992

We can observe that, while ξ_1^ϕ and ξ_2^ϕ are distributed over the final state ϕ_h^N and the bulk of the initial condition ϕ_h^0 respectively, the higher order basis ξ_i^ϕ, $i = 3,\ldots,10$ are oscillating functions over the set where the tumour is expanding during its temporal evolution, and thus contain the information about the tumour boundary and its expansion. Since the latter set is larger than the case shown in Figure 5, the number of oscillating functions over this region with a frequency needed to explain the 99.99% of the data is increased.
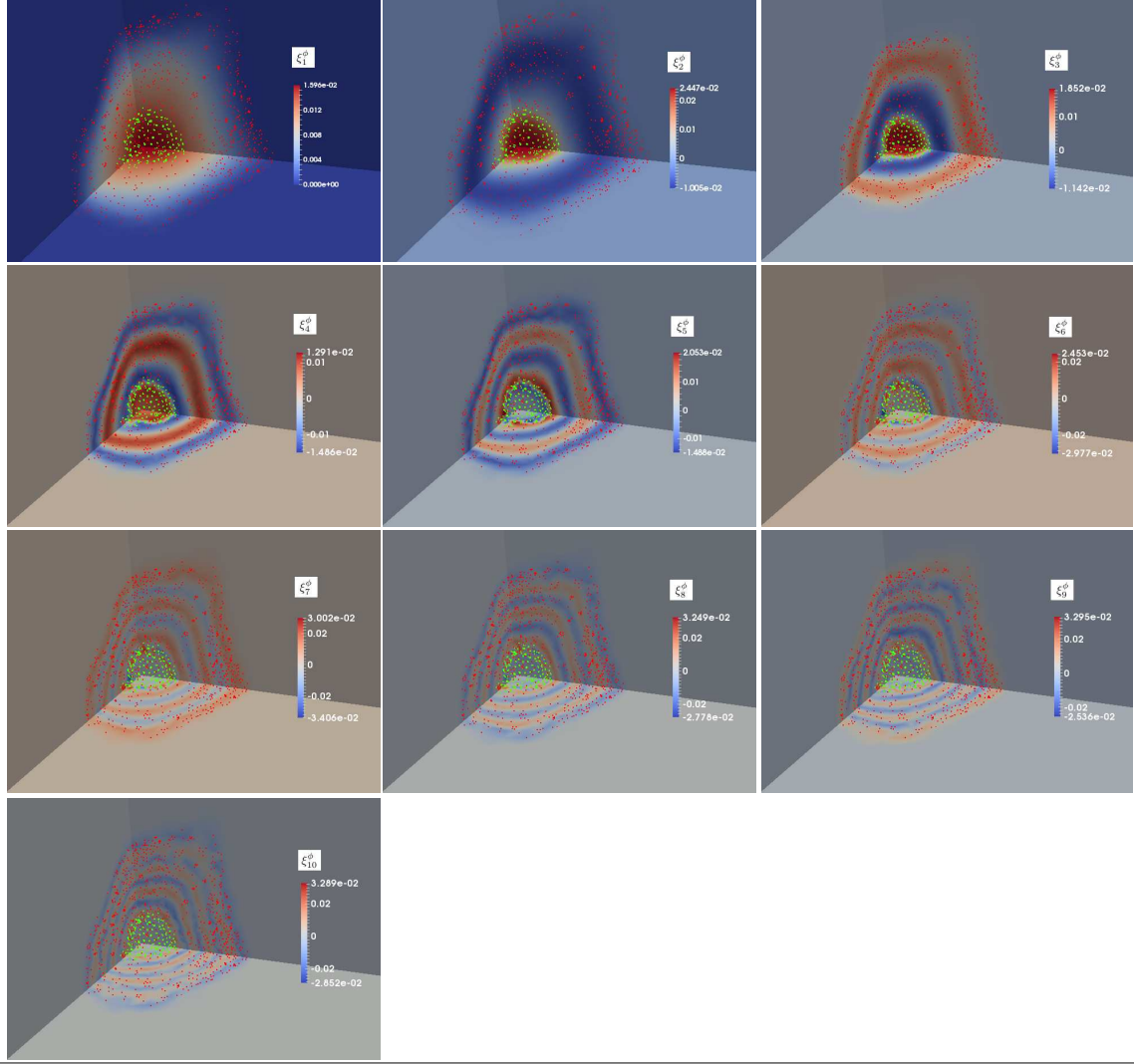
Figure 8: Plot of the basis elements ξ_i^{ϕ} corresponding to the highest eigenvalues needed to explain the 99.99% variance of the data, for $k = 0$, $N = 980$, $\mathcal{P}_0^{\text{bis}}$.

We show in Figure 9 a comparison between the final state ϕ_h^N calculated from the FOM simulation through **Algorithm 2** with parameter set $\mathcal{P}_0^{\text{bis}}$ and the corresponding final state $\sum_{i=1}^{N_{\text{POD}}} \alpha_{i0}^N \xi_i^{\phi}$ obtained as a solution of the ROM system (15) through **Algorithm 4**, with $N_{\text{POD}} = 5$ and $N_{\text{POD}} = 10$.

We observe that the ROM solution is approximating the FOM solution with a very high fidelity when we consider 10 POD basis (corresponding to a 99.99% threshold of POD variance), whereas a low fidelity approximation is obtained when considering 5 basis (corresponding to a 99.87% threshold of POD variance).

In Figure 10 we report the values of the functional $J(\vec{\alpha}_l, \mathcal{P}_l)$, of the normalised set of parameters

$$\mathcal{P}_l/\mathcal{P}_{\text{exp}} = \{L_l/L_{\text{exp}}, \nu_l/\nu_{\text{exp}}, k_{nl}/k_{n\text{exp}}, S_{nl}/S_{n\text{exp}}, \delta_{nl}/\delta_{n\text{exp}}, \gamma_l^2/\gamma_{\text{exp}}^2, E_l/E_{\text{exp}}, \delta_c/\delta_{c\text{exp}}, c_e/c_{e\text{exp}}\},$$

and of $|\mathcal{P}_l(1) - \mathcal{P}_l|$, computed in **Steps 3** and **4** of **Algorithm 1**, for $k = 0$, obtained when starting from the initial set of parameters $\mathcal{P}_0^{\text{bis}}$ and considering the time span $N = 490$. We
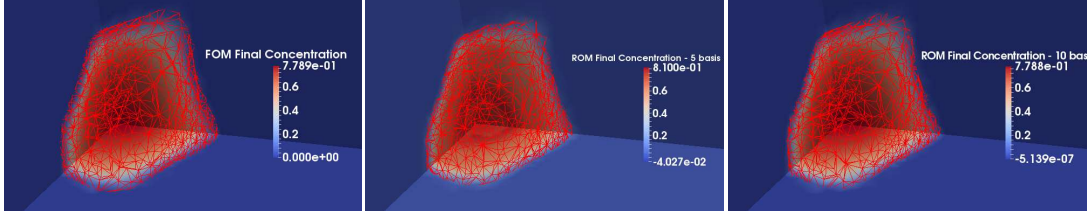
Figure 9: Comparison between the final state ϕ_h^N, solution of the FOM simulation with parameter set $\mathcal{P}_0^{\mathrm{bis}}$ and $N = 980$, and the corresponding final state $\sum_{i=1}^{N_{\mathrm{POD}}} \alpha_{i0}^N \xi_i^\phi$, solution of the ROM system (15). The iso–surfaces $\phi_h^N = \phi_e/2$ and $\sum_{i=1}^{N_{\mathrm{POD}}} \alpha_{i0}^N \xi_i^\phi = \phi_e/2$ are highlighted in red colors.

note that in this case we need $N_{\mathrm{POD}} = 6$ to explain the 99.99% of variance of the data. Moreover, in order for the Algorithm (25) to converge we need to choose $n_w = 2$.
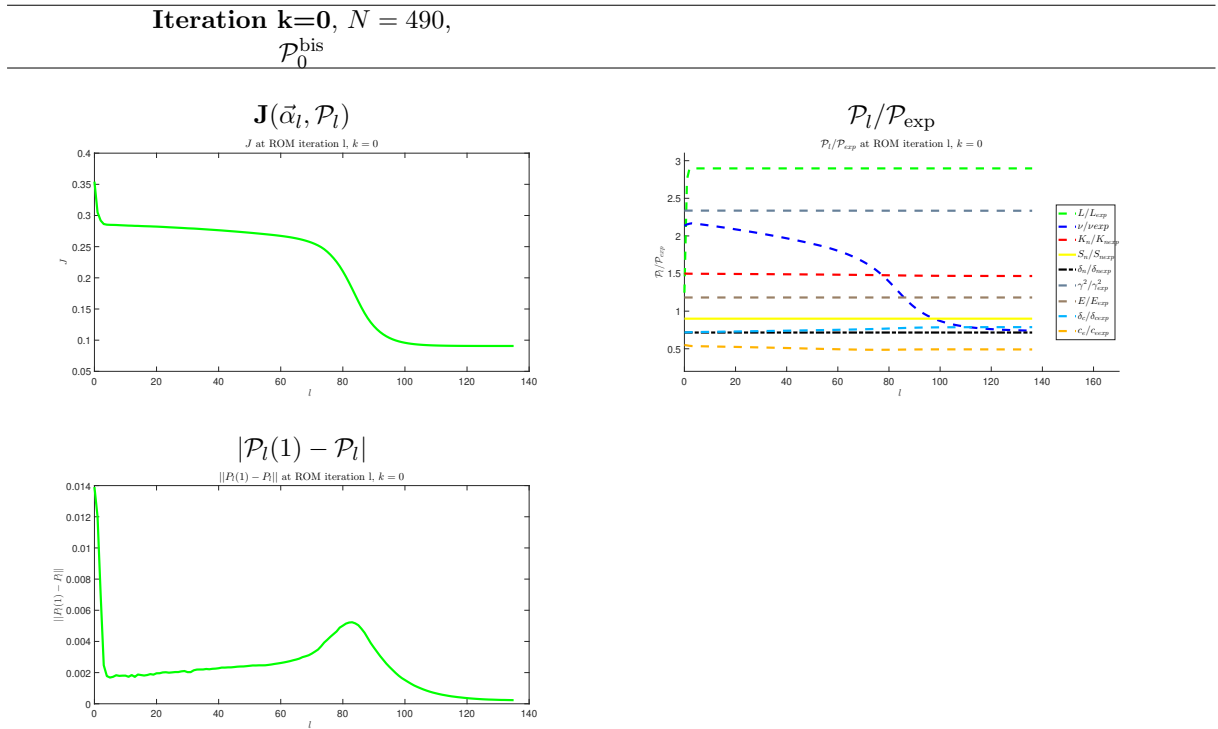
Iteration k=0, $N = 490$, $\mathcal{P}_0^{\mathrm{bis}}$

Figure 10: Values of the functional $J(\vec{\alpha}_l, \mathcal{P}_l)$, of the normalised set of parameters $\mathcal{P}_l/\mathcal{P}_{\mathrm{exp}}$ and of $|\mathcal{P}_l(1) - \mathcal{P}_l|$ for step $k = 0$ of **Algorithm 1**, with $N = 490$ and starting from the set $\mathcal{P}_0^{\mathrm{bis}}$.

We observe that the parameters ν and L go through a large excursion. The parameter ν is decreasing to $1/3$ of its initial value, whereas the parameter L reaches its active value $L_{\mathrm{bio,max}}$ and remains stick to it, differently from the behaviour observed in Figure 7 where, starting from $\mathcal{P}_0$, the parameter L reaches its maximum value and than relaxes to its initial value. The functional J, starting from a value $J = 0.3543$ higher than $J = 0.2847$ reported in Figure 7, relaxes onto a minimum value $J = 0.0906$ which is next to the value $J = 0.0870$ reported in Figure 7 in a number of steps $\bar{l} = 136$ much higher than $\bar{l} = 11$ in Figure 7. Finally, we consider the results of the **Steps 2–4** of Algorithm (1), for the first step $k = 0$, with starting point $\mathcal{P}_0$, $N = 490$ and when a threshold value of 99.9% is considered in the POD analysis. In Figure 11 we report the values of the functional $J(\vec{\alpha}_l, \mathcal{P}_l)$, of the

normalised set of parameters

$$\mathcal{P}_l/\mathcal{P}_{\exp} = \{L_l/L_{\exp}, \nu_l/\nu_{\exp}, k_{nl}/k_{n\exp}, S_{nl}/S_{n\exp}, \delta_{nl}/\delta_{n\exp}, \gamma_l^2/\gamma_{\exp}^2, E_l/E_{\exp}, \delta_c/\delta_{c\exp}, c_e/c_{e\exp}\},$$

and of $|\mathcal{P}_l(1) - \mathcal{P}_l|$, computed in **Steps 3** and **4** of **Algorithm 1**. We note that in this case we need $N_{\mathrm{POD}} = 4$ to explain the 99.9% of variance of the data.
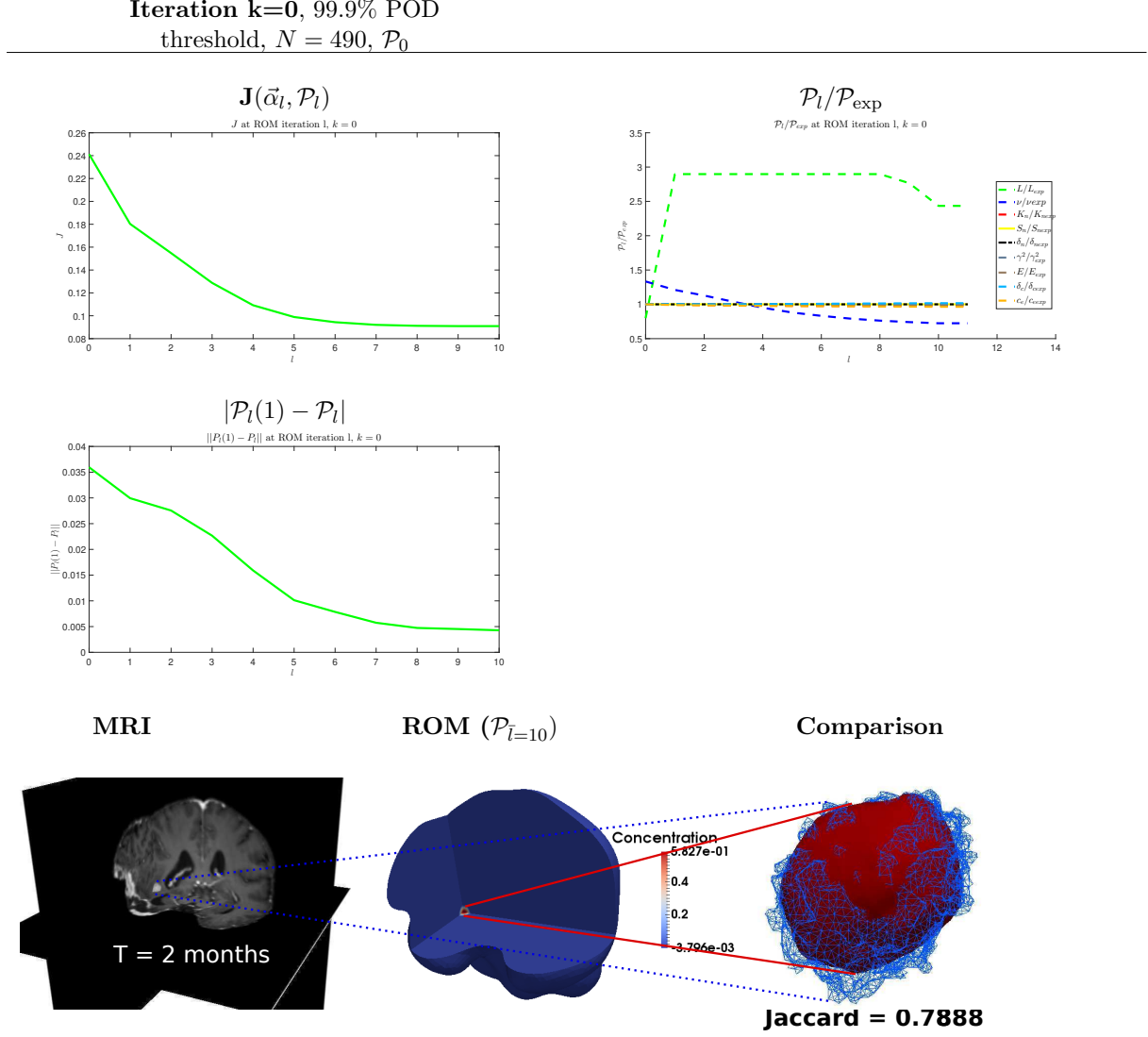

Figure 11: Values of the functional $J(\vec{\alpha}_l, \mathcal{P}_l)$, of the normalised set of parameters $\mathcal{P}_l/\mathcal{P}_{\exp}$ and of $|\mathcal{P}_l(1) - \mathcal{P}_l|$ for steps $k = 0$ of **Algorithm 1**, together with a comparison between the isosurfaces $\phi_{\mathrm{data}}(T) = 0$ (highlighted in blue color) and $\sum_{i=1}^{N_{\mathrm{POD}}} \alpha_{i\bar{l}}^N \xi_i^\phi = \phi_e/2$ (highlighted in red color).

We observe that in this case of a lower POD threshold of 99.9% the value of the functional J reaches a minimum value 0.0909 which is higher than the minimal value 0.0870 attained during the optimization algorithm with an higher threshold of 99.99% (see Figure 7). Moreover, in the former case the parameter ν varies by a smaller amount, whereas the parameter L, once reached the active value $L_{\max}$, changes of a smaller amount.

4.2 Test case 2: clinical follow-up after surgical resection and recurrence

Secondly, we apply the Optimization Algorithm so a clinical test case which followed the surgical resection and the recurrence pattern of a GBM.

A patient diagnosed with giant cell GBM underwent subtotal tumour removal. The patient started radiotherapy with concomitant Temozolomide 42 days after surgery following to Stupp protocol. The pre-Radiotherapy MRI showed tumour relapse. After 25 doses of RT, the patient had a severe worsening of the clinical status.

MRI were taken at the pre-operative, immediate post-operative, pre-radiotherapy (34 days after surgery) temporal stages and lastly at 5 days after the interruption of RT and concomitant CHT due to disease progression.

Our numerical simulations focus on the period starting with the surgical removal (initial time $t = 0$ of simulations) up to the first application of radiotherapy (time $t = T =: 34$ days). At $t = T$ we compare data and simulations, searching for the optimal set of parameters $\mathcal{P}_{opt}$ which locally minimises the functional (19), obtained by solving **Algorithm 1**, thus estimating the model parameters directing the recurrence growth without any adjuvant therapy.

In Figure 12 we show the axial, sagittal and coronal slices of the T1-weighted MRI at different temporal stages.

We can observe that, after the application of 25 fractions of RT, at $t = 78$ days after surgery (Post Rad event) the GBM recurrence has grown in volume with respect to the Pre Rad event, inducing a severe and rapid worsening of the patient's clinical status. The aim of the present work is to study the patient specific optimization of the growth parameters in the temporal range of tumour evolution after surgery and before the application of radiotherapy and chemotherapy.
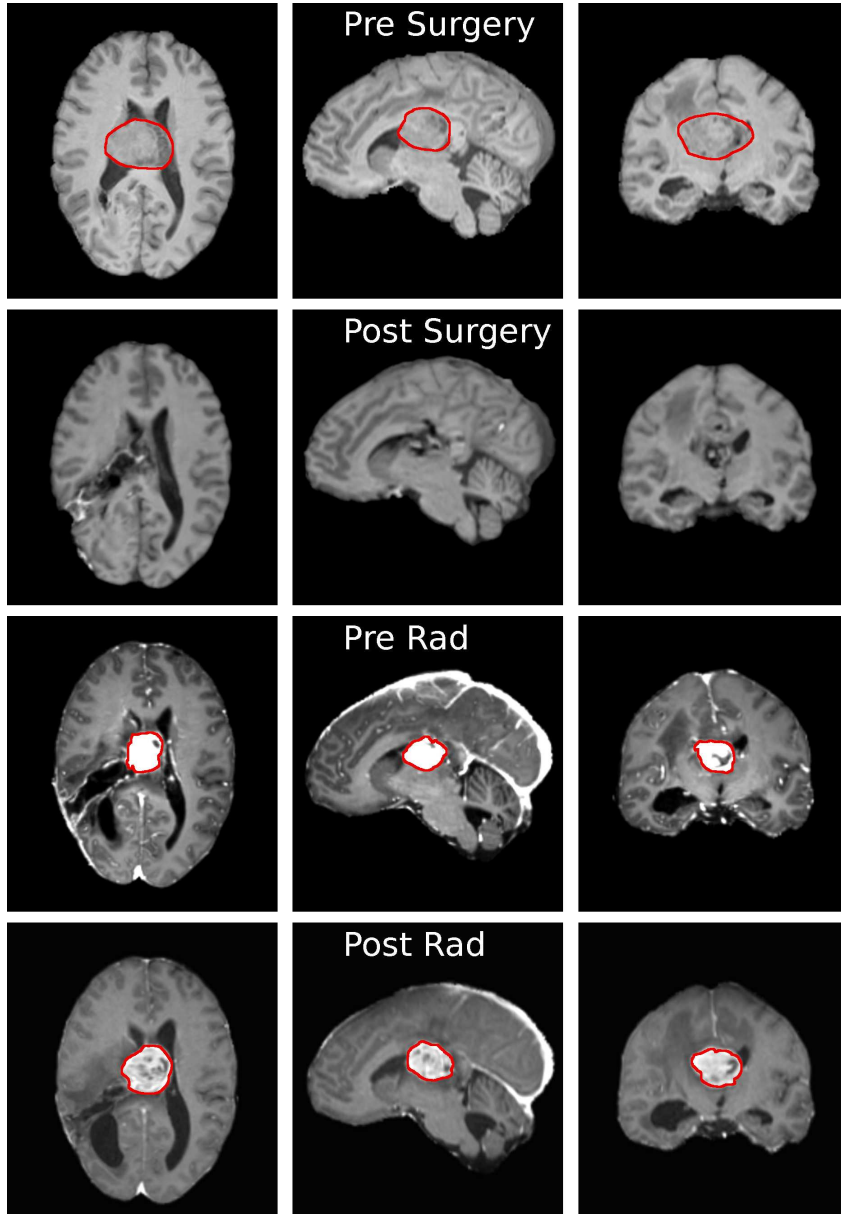
Figure 12: Axial (first column), sagittal (second column) and coronal (third column) slices of the T1-weighted MRI at different temporal stages. First row: before surgery; second raw: after surgery; third row: 34 days after surgery; fourth row: 78 days after surgery. It is possible to appreciate the subtotal resection of the corpus callosum GBM and the early tumour relapse at Pre Rad MRI and at Post Rad MRI. The segmented boundary of the tumour is highlighted in red color.

4.2.1 Initialisation

In Figures 13 and 14 we represent the results of the **initialisation** step of **Algorithm 1**, which defines the domain Ω (Figure 13), the map(WM,GM,CSF), the initial condition ϕ_h^0 and the tensors $\mathbf{D}$ and $\mathbf{T}$ (Figure 14).

The number of elements and the number of nodes of the mesh $\mathcal{T}_h$ are 305489 and 51005 respectively. Moreover, we choose $\Delta T = 0.1225$ (days), than $N = 280$. As in Test Case 1, a good refinement of the mesh in the region of tumour evolution is necessary to obtain ROM
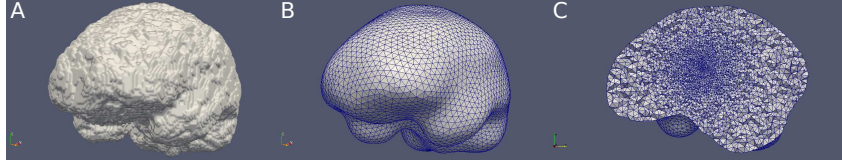
Figure 13: (A) External brain surface extracted from the medical images; (B) Smoothed and re–meshed external surface; (C) Tetrahedral mesh generated within the external surface, conveniently refined in the area surrounding the tumour.
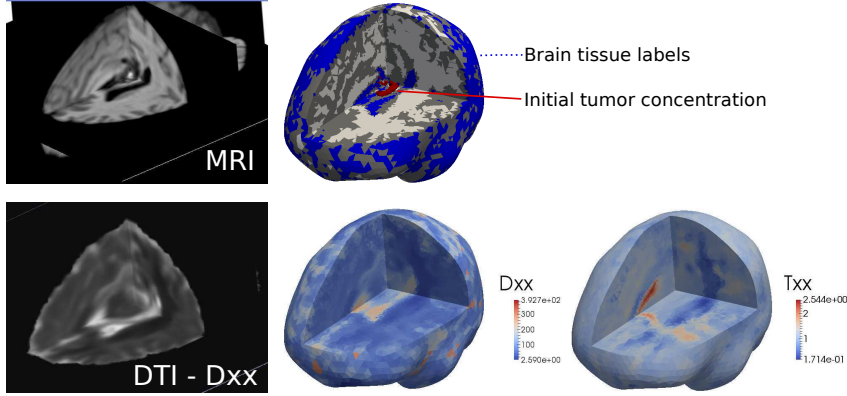

Figure 14: 3D virtual reconstructions of the MRI (top) and DTI (bottom) data, with the corresponding computational meshes containing the labels of the brain tissues and the xx component of the tensors $\mathbf{D}$ and $\mathbf{T}$. White matter, grey matter and CSF are highlighted in white, grey and blue colors respectively. The initial tumour distribution is also highlighted in brown color, as segmented from the T1 MRI.

systems with sufficiently low dimensionality to be solved with low computational resources and in highly reduced computational times.

In a similar way the characteristic function of the tumour extension $\phi_{\text{data}}(T)$ has been obtained from the segmentation of the MR images at $t = 34$ days (PreRad event).

4.2.2 Step 1

In Figure 15 we report the values of the functional $J(\phi_h^N(\mathcal{P}_k), \mathcal{P}_k)$, calculated in **step 1** of **Algorithm 1**, and of the set of parameters $\mathcal{P}_k$, for different values of k. We also plot the isosurfaces $\phi_{\text{data}}(T) = 0$ and $\phi_h^N(\mathcal{P}_k) = \phi_e/2$ from the FOM simulations, reporting the Jaccard index between the two volumes enclosed by these surfaces.

Iteration	$\mathbf{J}(\mathcal{P}_0)$	$\mathbf{L}_0$	$\boldsymbol{\nu}_0$	$\mathbf{k}_{n0}$	$\mathbf{S}_{n0}$	$\boldsymbol{\delta}_{n0}$	$\boldsymbol{\gamma}_0^2$	$\mathbf{E}_0$	$\boldsymbol{\delta}_0$	$\mathbf{c}_{e0}$
k=0	0.28323	0.0002	0.08	2	10000	8640	0.1225	694	0.3	0.611

MRI   FOM   Comparison
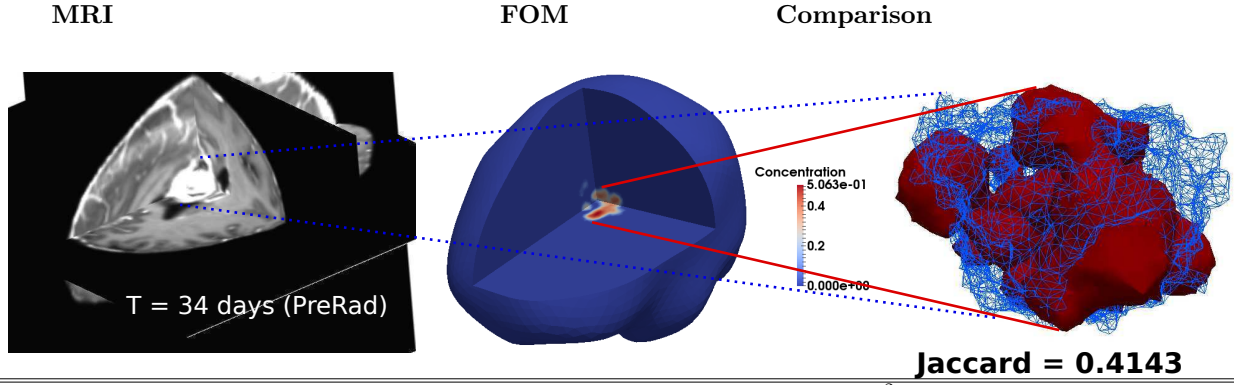
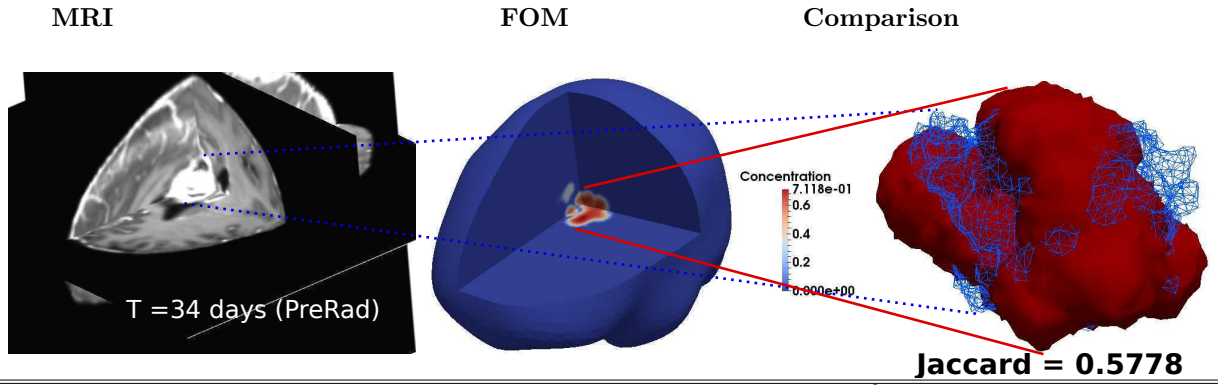
Iteration	$\mathbf{J}(\mathcal{P}_1)$	$\mathbf{L}_1$	$\boldsymbol{\nu}_1$	$\mathbf{k}_{n1}$	$\mathbf{S}_{n1}$	$\boldsymbol{\delta}_{n1}$	$\boldsymbol{\gamma}_1^2$	$\mathbf{E}_1$	$\boldsymbol{\delta}_1$	$\mathbf{c}_{e1}$
k=1	0.2554	0.0002	0.18537	2.1046	10000.06	8639.94	0.1225	693.97	0.2160	0.611

MRI   FOM   Comparison

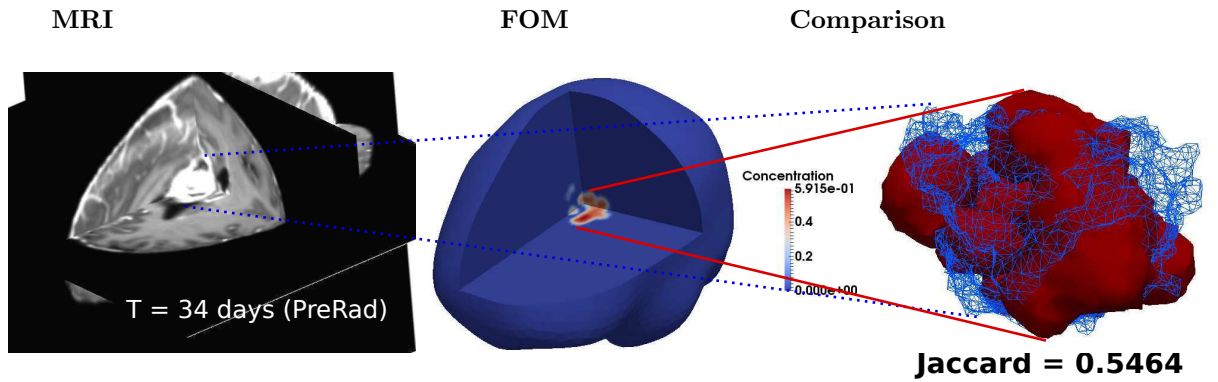| Iteration	$\mathbf{J}(\mathcal{P}_2)$	$\mathbf{L}_2$	$\boldsymbol{\nu}_2$	$\mathbf{k}_{n2}$	$\mathbf{S}_{n2}$	$\boldsymbol{\delta}_{n2}$	$\boldsymbol{\gamma}_2^2$	$\mathbf{E}_2$	$\boldsymbol{\delta}_2$	$\mathbf{c}_{e2}$
k=2	0.2298	0.000532	0.10573	2.0805	10000.05	8639.94	0.1225	693.97	0.2376	0.5792

MRI   FOM   Comparison

Figure 15: Values of $J(\phi_h^N(\mathcal{P}_k), \mathcal{P}_k)$ and of $\mathcal{P}_k$ for different iteration steps k of **Algorithm 1**, with a comparison between the iso–surfaces $\phi_{\text{data}}(T) = 0$ (highlighted in blue color) and $\phi_h^N(\mathcal{P}_k) = \phi_e/2$ (highlighted in red color).

The **Algorithm 1** stops since

$$J(\phi_h^N(\mathcal{P}_{k+1}), \mathcal{P}_{k+1}) = J(\phi_h^N(\mathcal{P}_k), \mathcal{P}_k)$$

for $k = 2$. Indeed, the ROM optimization algorithm for $k = 2$ makes no advances in the parameter space (see Figure 18). We thus identify

$$\mathcal{P}_{\text{opt}} \equiv \mathcal{P}_2 =$$
$$\{L = 0.000532, \nu = 0.10573, k_n = 2.0805, S_n = 10000.05, \delta_n = 8639.94, \gamma^2 = 0.1225,$$
$$E = 693.97, \delta = 0.2376, c_e = 0.5792\}, \tag{28}$$

with the corresponding units. We observe that also in this case the overall overlapping between the tumour extensions from FOM simulations and from data is increasing, which is shown by the corresponding increase in the value of the Jaccard index. The Jaccard indexes are anyhow smaller than the values computed for Test Case 1, reported in Figure 4, due to greater uncertainty in the segmentation of initial left tumour particles after surgery and in the segmentation of the tumour extension before radiotherapy, which consists in peritumoural infiltrations which are not visible in the MRI data.

4.2.3 Step 2

In Table 6 we report, for each step k of **Algorithm 1**, the values of the cumulated fractions of $\mathrm{tr}\mathbf{F}_1^T\mathbf{F}_1, \mathrm{tr}\mathbf{F}_2^T\mathbf{F}_2, \mathrm{tr}\mathbf{F}_3^T\mathbf{F}_3, \mathrm{tr}(\psi_1'(\mathbf{F}_1))^T\psi_1'(\mathbf{F}_1), \mathrm{tr}(\psi_1''(\mathbf{F}_1))^T\psi_1''(\mathbf{F}_1)$ associated to the eigenvalues of the corresponding matrices, arranging them starting from the eigenvalue with the highest magnitude and following a decreasing order.

Table 6: Values of the cumulated fraction of $\mathrm{tr}\mathbf{F}_1^T\mathbf{F}_1$,$\mathrm{tr}\mathbf{F}_2^T\mathbf{F}_2$,$\mathrm{tr}\mathbf{F}_3^T\mathbf{F}_3$,$\mathrm{tr}(\psi_1'(\mathbf{F}_1))^T\psi_1'(\mathbf{F}_1)$,$\mathrm{tr}(\psi_1''(\mathbf{F}_1))^T\psi_1''(\mathbf{F}_1)$ for the first eigenvalues with the highest magnitude.

Iteration k=0	Eigenvalue	% $\mathrm{tr}\mathbf{F}_1^T\mathbf{F}_1$	% $\mathrm{tr}\mathbf{F}_2^T\mathbf{F}_2$	% $\mathrm{tr}\mathbf{F}_3^T\mathbf{F}_3$	% $\mathrm{tr}(\psi_1')^T\psi_1'$	% $\mathrm{tr}(\psi_1'')^T\psi_1''$
	First	93.5098	99.9731	99.9904	99.9714	99.7753
	Second	99.5129	99.9973	99.9993	99.9960	99.9577
	Third	99.9574	99.9998	99.9999	99.9998	99.9984
	Fourth	99.9957	99.9999	99.9999	99.9999	99.9998
Iteration k=1	Eigenvalue	% $\mathrm{tr}\mathbf{F}_1^T\mathbf{F}_1$	% $\mathrm{tr}\mathbf{F}_2^T\mathbf{F}_2$	% $\mathrm{tr}\mathbf{F}_3^T\mathbf{F}_3$	% $\mathrm{tr}(\psi_1')^T\psi_1'$	% $\mathrm{tr}(\psi_1'')^T\psi_1''$
	First	92.6867	99.7216	99.9210	99.5998	99.3884
	Second	98.8774	99.9860	99.9951	99.9878	99.9182
	Third	99.8253	99.9980	99.9993	99.9980	99.9844
	Fourth	99.9702	99.9996	99.9998	99.9997	99.9983
	Fifth	99.9945	99.9999	99.9999	99.9999	99.9997
Iteration k=2	Eigenvalue	% $\mathrm{tr}\mathbf{F}_1^T\mathbf{F}_1$	% $\mathrm{tr}\mathbf{F}_2^T\mathbf{F}_2$	% $\mathrm{tr}\mathbf{F}_3^T\mathbf{F}_3$	% $\mathrm{tr}(\psi_1')^T\psi_1'$	% $\mathrm{tr}(\psi_1'')^T\psi_1''$
	First	93.2361	99.9348	99.9793	99.9325	99.4953
	Second	99.3359	99.9958	99.9988	99.9946	99.9383
	Third	99.9291	99.9995	99.9998	99.9996	99.9971
	Fourth	99.9915	99.9999	99.9999	99.9999	99.9996

We thus have that

$$N_{\text{POD}} = N_\phi^{\text{POD}} = 4, \quad \text{for } k = 0, 2, \ N_{\text{POD}} = N_\phi^{\text{POD}} = 5, \quad \text{for } k = 1.$$
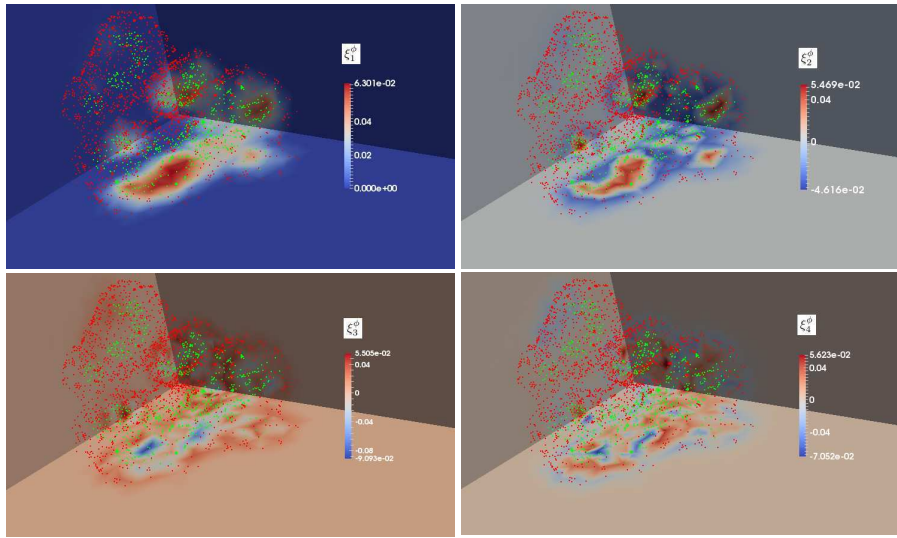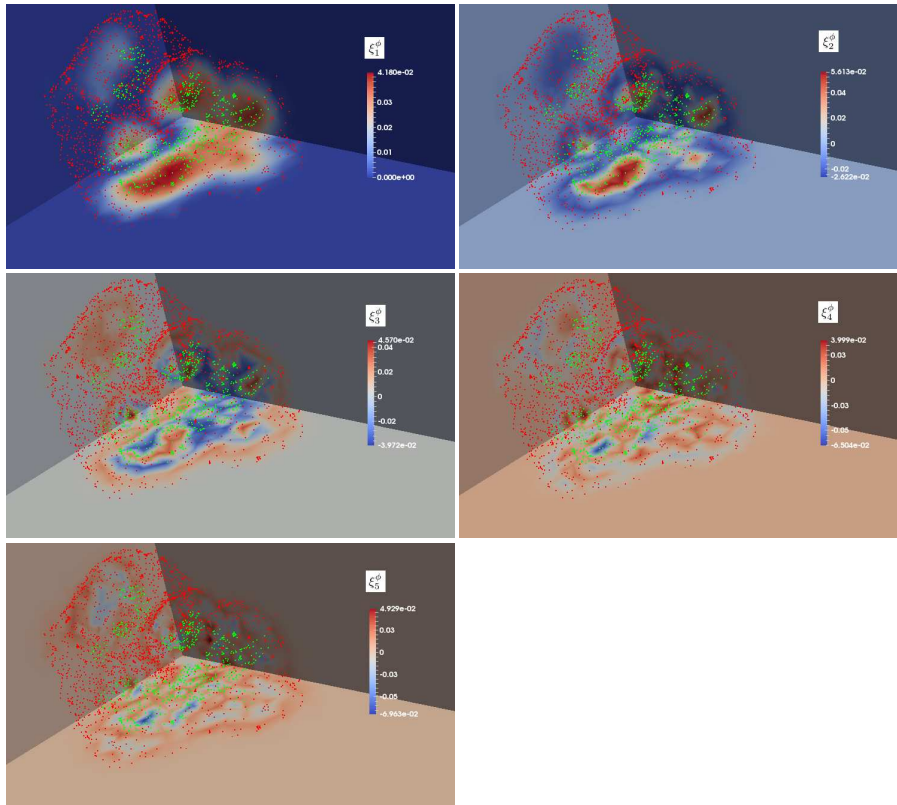
Iteration k=0

Iteration k=1

Figure 16: Plot of the basis elements ξ_i^ϕ, corresponding to the highest eigenvalues needed to explain the 99.99% of the data, for $k = 0, 1$. Green and red points are distributed over the initial condition and final distribution of cell concentration, respectively.

In Figure 16 we show the basis elements ξ_i^ϕ, corresponding to the highest eigenvalues needed to explain the 99.99% variance of the data, for $k = 0, 1$.

We observe, as in the previous Test Case 1, that ξ_1^ϕ and ξ_2^ϕ are distributed over the core of the final state ϕ_h^N and the initial condition ϕ_h^0 respectively, whereas ξ_3^ϕ, ξ_4^ϕ and ξ_5^ϕ are oscillating functions over the set where the tumour is expanding during its temporal evolution, and thus contain the information about the tumour boundary and its expansion. We observe that the low dimensionality of the ROM systems is preserved also in the case of tumour dynamics with sparse tumour particles and infiltrations, if the mesh for the FOM system is sufficiently well refined in the region of the tumour core and infiltrations.

We finally show in Figure 17 a comparison between the final state ϕ_h^N calculated from the FOM simulation through **Algorithm 2** with parameter set $\mathcal{P}_0$ and the corresponding final state $\sum_{i=1}^{N_{\text{POD}}} \alpha_{i0}^N \xi_i^\phi$ obtained as a solution of the ROM system (15) through **Algorithm 4**.
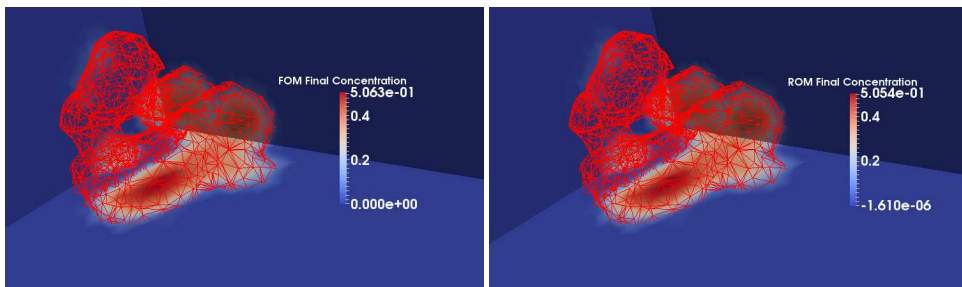

Figure 17: Comparison between the final state ϕ_h^N, solution of the FOM simulation with parameter set $\mathcal{P}_0$ and the corresponding final state $\sum_{i=1}^{N_{\text{POD}}} \alpha_{i0}^N \xi_i^\phi$, solution of the ROM system (15). The iso–surfaces $\phi_h^N = \phi_e/2$ and $\sum_{i=1}^{N_{\text{POD}}} \alpha_{i0}^N \xi_i^\phi = \phi_e/2$ are highlighted in red color.

We observe also in this test case that the ROM solution is approximating the FOM solution with a very high fidelity.
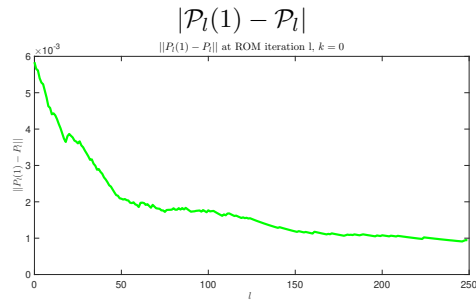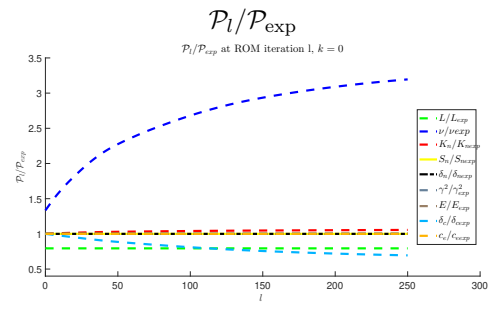
4.2.4 Steps 3 and 4

In Figure 18 we report the values of the functional $J(\vec{\alpha}_l, \mathcal{P}_l)$, of the normalised set of parameters

$$\mathcal{P}_l/\mathcal{P}_{\text{exp}} = \{L_l/L_{\text{exp}}, \nu_l/\nu_{\text{exp}}, k_{nl}/k_{n\text{exp}}, S_{nl}/S_{n\text{exp}}, \delta_{nl}/\delta_{n\text{exp}}, \gamma_l^2/\gamma_{\text{exp}}^2, E_l/E_{\text{exp}}, \delta_c/\delta_{c\text{exp}}, c_e/c_{e\text{exp}}\},$$

and of $|\mathcal{P}_l(1) - \mathcal{P}_l|$, computed in **Steps 3** and **4** of **Algorithm 1**, for $k = 0, 1, 2$. We also plot the isosurfaces $\phi_{\text{data}}(T) = 0$ from the MRI data and $\sum_{i=1}^{N_{\text{POD}}} \alpha_{i\bar{l}}^N \xi_i^\phi = \phi_e/2$ from the ROM simulations, where $\bar{l}$ is the value of the last iteration of **Step 4**, reporting the value of the Jaccard index between the two sets enclosed by these surfaces.

$\mathbf{J}(\vec{\alpha}_l, \mathcal{P}_l)$

J at ROM iteration l, $k = 0$

$\mathcal{P}_l/\mathcal{P}_{\exp}$

$\mathcal{P}_l/\mathcal{P}_{exp}$ at ROM iteration l, $k = 0$

$|\mathcal{P}_l(1) - \mathcal{P}_l|$

$||P_l(1) - P_l||$ at ROM iteration l, $k = 0$
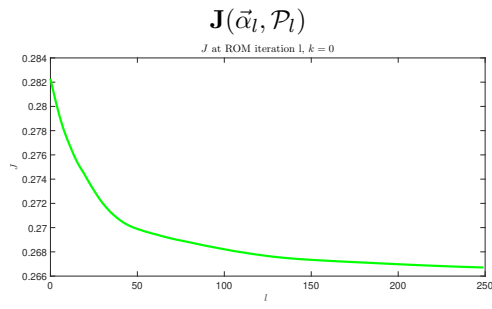
MRI **ROM $(\mathcal{P}_{\bar{l}=249})$** **Comparison**

T = 34 days (PreRad)

Concentration

Iaccard = 0.5060

$\mathbf{J}(\vec{\alpha}_l, \mathcal{P}_l)$

J at ROM iteration l, $k = 1$

$\mathcal{P}_l/\mathcal{P}_0$

$\mathcal{P}_l/\mathcal{P}_{exp}$ at ROM iteration l, $k = 1$

$|\mathcal{P}_l(1) - \mathcal{P}_l|$

$||P_l(1) - P_l||$ at ROM iteration l, $k = 1$

| MRI | ROM ($\mathcal{P}_{\bar{l}=34}$) | Comparison |

T = 34 days (PreRad)

Concentration
6.278e-01
0.4
0.2
0.000e+00

Jaccard = 0.5730

Iteration k=2

| $\mathbf{J}(\vec{\alpha}_l, \mathcal{P}_l)$ | $|\mathcal{P}_l(1) - \mathcal{P}_l|$ |
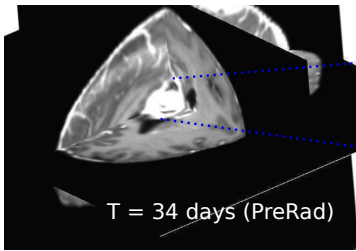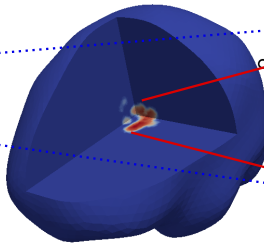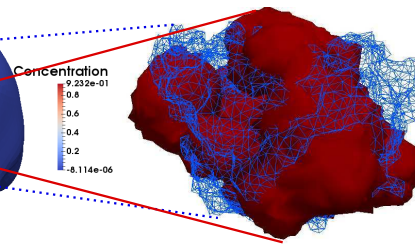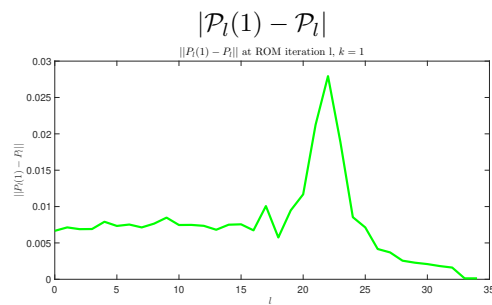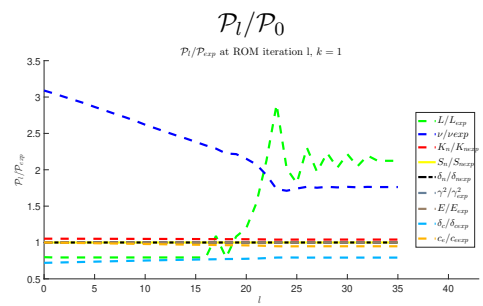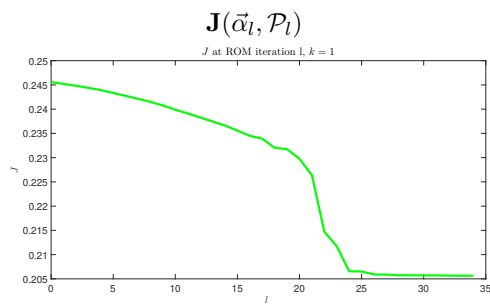
Figure 18: Values of the functional $J(\vec{\alpha}_l, \mathcal{P}_l)$ and of the normalised set of parameters $\mathcal{P}_l/\mathcal{P}_0$ for steps $k = 0, 1, 2$ of **Algorithm 1**, together with a comparison between the iso–surfaces $\phi_{\text{data}}(T) = 0$(highlighted in blue color) and $\sum_{i=1}^{N_{\text{POD}}} \alpha_{il}^N \xi_i^\phi = \phi_e/2$ (highlighted in red color).

For $k = 0$ the ROM optimization process in **Steps 3** and **4** goes through 249 steps before matching the termination conditions. Thus the ROM Optimization Algorithm is much slower in Test Case 2, corresponding to irregular initial data and target function, then in Test Case 1, which is characterised by more regular data. We also observe that, like in Test Case 1, only the model parameters L, ν, δ, c_e cha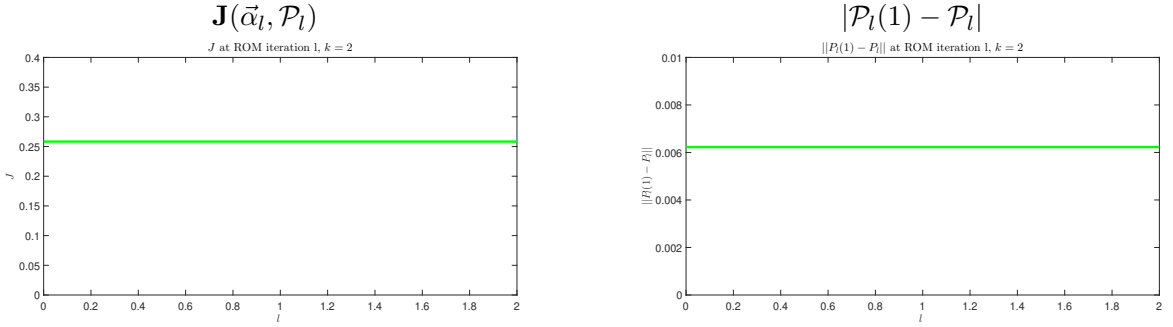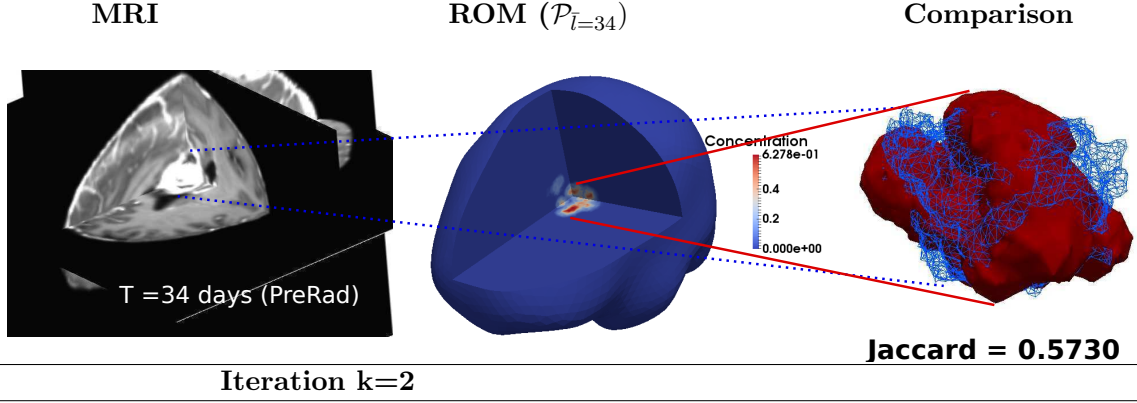nge significantly from their starting values during the optimization process, being the system quite insensitive to changes of the remaining parameters $k_n, S_n, \delta_n, \gamma^2, E$. The proliferation rate ν is the most sensitive parameter for $k = 0$. For $k = 1$ the ROM optimization process in **Steps 3** and **4** goes through 34 steps. We observe that for $k = 1$ also the parameter L varies by a large excursion along the functional minimisation and relaxes in an oscillating manner onto its local equilibrium value. Finally, for $k = 2$ the ROM optimization process is making no progress.

Comparing the output of the Optimization Algorithm (1) with the ones reported in Figure 7 for Test Case 1, we observe that in Test Case 2 we need more iterations to converge to an optimal state, that the functional overall decreases of a much smaller amount (due to the uncertainty in identifying the target function) and that the computation of new POD basis associated to different set of parameters introduces a higher degree of variability in the tumour dynamics, causing the minimising sequences of parameters to show oscillations instead of monotone relaxing to the optimal state like in Test Case 1.

4.2.5   Computational cost

We conclude by reporting in Table 7 the elapsed time (in seconds) for the computation of steps $1 - 4$ of **Algorithm 1** for the different values of the iteration step k. Comparing Table 7 with Table 3 we observe that in the case of tumour recurrence with sparse particles and infiltrations the computational time for the projected gradient iterations at the ROM

Table 7: Elapsed time (in seconds) for the computation of steps $1 - 4$, for the different values of the iteration step k.

Iteration k=0	Step 1	Step 2	Step 3	Step 4
	144575.36	8.58	2438.42	3431.52

Iteration k=1	Step 1	Step 2	Step 3	Step 4
	164645.5	11.75	6453.26	336.09

Iteration k=2	Step 1	Step 2	Step 3	Step 4
	135222.43	7.75	2416.61	45.14

level is 2 to 3 order of magnitude smaller than the time needed to solve the FOM problem, provided to properly refine the mesh in the FOM simulations. We also note that the FOM computations require a comparable computational time with respect to Test Case 1. The same is valid for the computational time required to assemble the ROM systems in **Step 3**. We finally conclude that the computational efficiency of the Optimization Algorithm (1) is unaffected by the degree of regularity of the tumour dynamics, at least in the test cases analysed here where no morphological transition happens during the evolution. The degree of convergence of the optimization algorithm and the degree of variability of parameters along the projected gradient directions introduced by exploring the parameter space through different basis functions is instead affected by the tumour dynamics regularity.

4.2.6 Some remarks on benchmark results

In this paragraph we report some numerical results to show how the POD analysis in **Step 2** of Algorithm (1) varies when the tumour concentration in the FOM simulations in **Step 1** is spreading on a larger region than the one observed in Test Case 1, considering a tumour dynamics over a larger time interval. Moreover, we report numerical results about the performance of **Step 4** of Algorithm (1) when a lower threshold of POD significance (namely 99.9%) is considered.

In Table 8 we report the POD analysis of the snapshot matrices obtained from the FOM solution (8) at $k = 0$ of **Algorithm 1** with $N = 980$ and initial set $\mathcal{P}_0$, i.e. when the tumour dynamics span a time interval of 120 days.

Table 8: Values of the cumulated fraction of $\mathrm{tr}\mathbf{F}_1^T\mathbf{F}_1$,$\mathrm{tr}\mathbf{F}_2^T\mathbf{F}_2$,$\mathrm{tr}\mathbf{F}_3^T\mathbf{F}_3$,$\mathrm{tr}(\psi_1'(\mathbf{F}_1))^T\psi_1'(\mathbf{F}_1)$,$\mathrm{tr}(\psi_1''(\mathbf{F}_1))^T\psi_1''(\mathbf{F}_1)$ for the first eigenvalues with the highest magnitude.

Iteration k=0 $N = 980, \mathcal{P}_0$	Eigenvalue	% $\mathrm{tr}\mathbf{F}_1^T\mathbf{F}_1$	% $\mathrm{tr}\mathbf{F}_2^T\mathbf{F}_2$	% $\mathrm{tr}\mathbf{F}_3^T\mathbf{F}_3$	% $\mathrm{tr}(\psi_1')^T\psi_1'$	% $\mathrm{tr}(\psi_1'')^T\psi_1''$
	First	89.4596	99.9168	99.9707	99.9142	97.3884
	Second	98.1194	99.9783	99.9937	99.9737	99.7634
	Third	99.6551	99.9931	99.9973	99.9925	99.9445
	Fourth	99.9223	99.9991	99.9996	99.9989	99.9914
	Fifth	99.9818	99.9998	99.9999	99.9998	99.9985
	Sixth	99.9954	99.9999	99.9999	99.9999	99.9995

We thus have that $N_{\mathrm{POD}} = N_\phi^{\mathrm{POD}} = 6$ for $k = 0$. We note that in this case the number of basis functions needed to explain 99.99% of the data on a time window of 120 days is

lower than in Test Case 1 (see Table 4). This is due to the fact that the tumour expansion through time in Test Case 2 is limited by the presence of the ventricle' walls, and thus the region where the tumour is spreading from the initial tumour distribution is contained.

Finally, we consider the results of the **Steps 2–4** of Algorithm (1), for the first step $k = 0$, with $N = 490$ and starting set $\mathcal{P}_0$ and when a threshold value of 99.9% is considered in the POD analysis. In Figure 19 we report the values of the functional $J(\vec{\alpha}_l, \mathcal{P}_l)$, of the normalised set of parameters

$$\mathcal{P}_l/\mathcal{P}_{\exp} = \{L_l/L_{\exp}, \nu_l/\nu_{\exp}, k_{nl}/k_{n\exp}, S_{nl}/S_{n\exp}, \delta_{nl}/\delta_{n\exp}, \gamma_l^2/\gamma_{\exp}^2, E_l/E_{\exp}, \delta_c/\delta_{c\exp}, c_e/c_{e\exp}\},$$

and of $|\mathcal{P}_l(1) - \mathcal{P}_l|$, computed in **Steps 3** and **4** of **Algorithm 1**, for $k = 0$. We note that in this case we need $N_{\mathrm{POD}} = 3$ to explain the 99.9% of variance of the data.
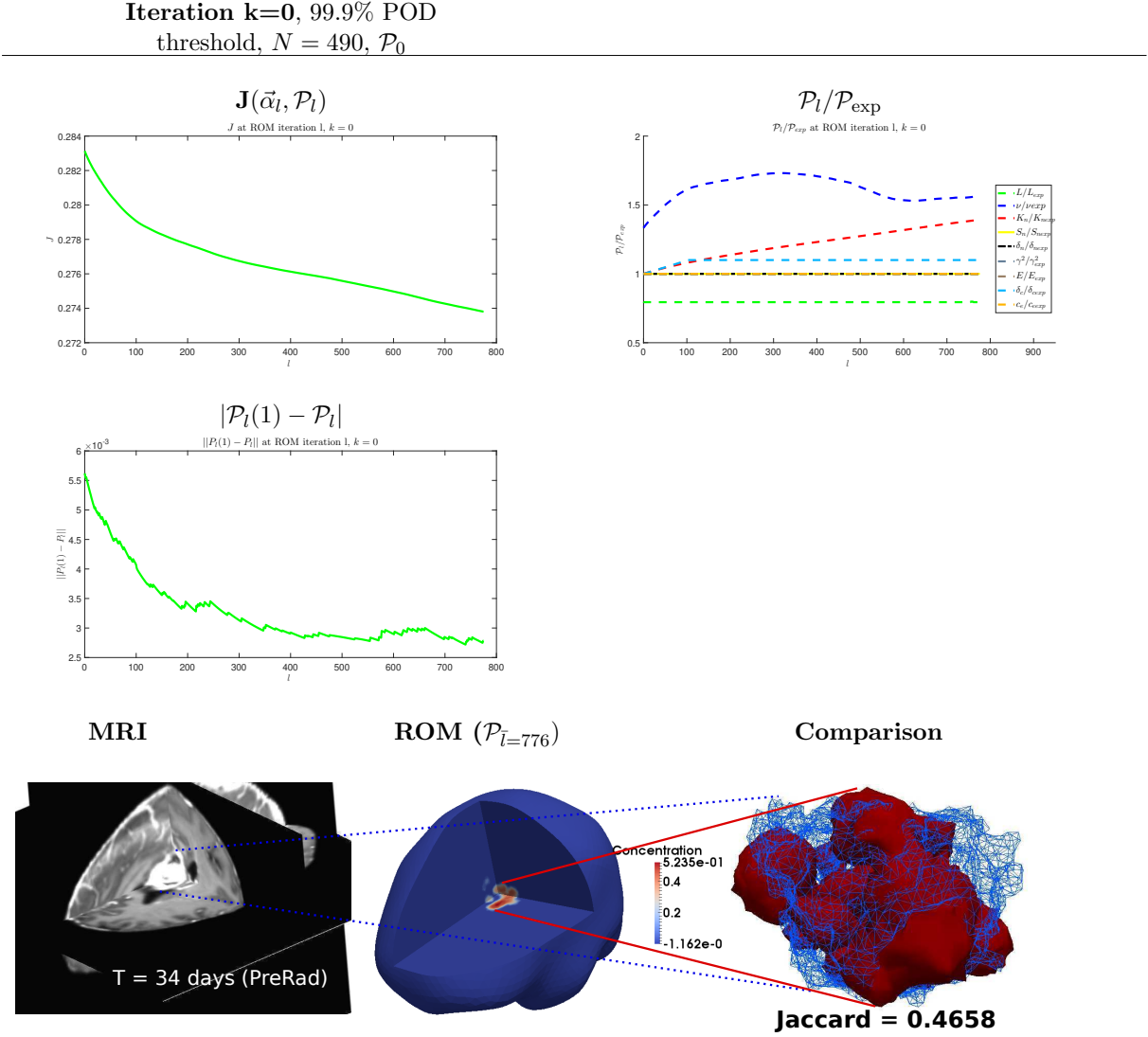
Figure 19: Values of the functional $J(\vec{\alpha}_l, \mathcal{P}_l)$, of the normalised set of parameters $\mathcal{P}_l/\mathcal{P}_{\exp}$ and of $|\mathcal{P}_l(1) - \mathcal{P}_l|$ for steps $k = 0$ of **Algorithm 1**, with $N = 490$, $\mathcal{P}_0$ and 99.9% POD threshold, together with a comparison between the isosurfaces $\phi_{\mathrm{data}}(T) = 0$ (highlighted in blue color) and $\sum_{i=1}^{N_{\mathrm{POD}}} \alpha_{i\bar{l}}^N \xi_i^\phi = \phi_e/2$ (highlighted in red color).

We observe that in this case of a lower POD threshold of 99.9% the value of the functional J reaches a minimum value 0.2738 which is higher than the minimal value 0.2667 attained during the optimization algorithm with an higher threshold of 99.99% (see Figure 7). The

local minimum is attained in a large number of steps $\bar{l} = 776$. Moreover, in the former case the parameter ν varies by a much smaller amount, the parameters L and δ remain unchanged and the parameter k_n varies through the functional minimisation. We also see more noise in the plot of $|\mathcal{P}_l(1) - \mathcal{P}_l|$ with respect to the case with 99.99% threshold.

5   Conclusions

This work proposed a novel Optimization Algorithm (1) for the parameter estimation of a nonlinear diffuse interface model of GBM evolution from neuroimaging data. The algorithm solves a constrained optimization problem in the form of a MPEC defined in **Problem 8** (22), where the objective functional is defined in (21) by a proper distance between the tumour domain set in numerical simulations and the corresponding clinical data at a key time of clinical interest. Due to the high computational cost of solving the FOM (defined in **Problem 2** (9)), the algorithm iteratively computes the optimization functional at the FOM level and minimises it at the ROM level through sensitivity analysis.

First, an effective MOR is defined through **Problems 3, 4, 5** (see (11), (16) and (17)), by projecting the equations onto the POD basis obtained from the time snapshots of the FOM solutions and approximating the nonlinear terms through DEIM interpolation. The nonlinearity of the ROM system is solved by a Newton algorithm, interpolating the nonlinear terms associated to the singular potential and its first derivative on the same interpolation nodes to enforce there the separation property of the FOM solution. Moreover, the degenerate mobility and chemotactic terms are transformed as higher order tensors acting on the reduced order space, taking into account for both the degeneracy of the corresponding terms at the FOM level and the heterogeneity and anisotropy of the tumour invasion pattern.

A sensitivity analysis is performed at the ROM level to minimise the optimization functional by solving linearised systems defined in **Problem 6** (18) and updating the parameters along weighted gradient directions solving **Problem 9** (25).

The algorithm ensures that the ROM solutions do not violate the physical constraints satisfied by the FOM solutions while dynamically spanning the space of parameters throughout the iterative steps. In particular, new POD basis functions associated to the updated set of parameters are calculated when the ROM minimisation problem has converged. This is an alternative way to consider parameters variability in the MOR of evolution equations with respect to the local reduced basis method used e.g. in [35].

   Second, we applied the proposed algorithm using the neuroimaging data provided by two clinical test cases: the growth of a primary GBM and a recurrent GBM after surgical resection.

In both cases we observed the convergence of the algorithm to an optimal state, represented by the optimal sets of parameters (27) and (28). These two sets display different optimal values, since the GBM spreading dynamics during primary and recurrent growth are controlled by intrinsically different biological processes. Moreover, the difference in the two set of parameters reflects also the higher aggressiveness of giant GBM cells in Test Case 2, which is reflected in higher values of motility and proliferation.

In both cases we observed that the ROM solution approximates the FOM solution with a very high fidelity, and that the accuracy in reproducing the tumour domain from neuroimaging data increases at each step during the optimization process.

The number of basis functions needed to explain the 99.99% variance of the data and the kind of morphological informations contained in them are the same in both cases, probably due to the fact that there are no significant topological changes in the evolution dynamics, that occurs smoothly thanks to chosen mesh refinement in the tumour evolution region. This turned out to be an important feature in order to deal with low dimensional higher–order tensors in **Problem 4** (16): ROM systems become indeed solvable with low computational resources and in highly reduced computational times.

We also observe that the computational time for the projected gradient iterations at the ROM level (**Step 4** of Algorithm (1)) is 2 to 4 orders of magnitude smaller than the time needed to solve the FOM problem, while the time for the assembly of the ROM systems

(**Step 3**) is 2 orders of magnitude smaller. This makes the whole algorithm very efficient in reducing the computational cost of the optimization process, both in the cases of the regular growth of a primary tumour and in the case of tumour recurrence with sparse particles and infiltrations. The overall time of a sensitivity analysis performed at the FOM level is finally reduced by 2 order of magnitude.

Finally we note that the Jaccard indexes calculated at the optimal states for Test Case 2 are smaller than the values computed for Test Case 1, and that we need more iterations to converge to an optimal state in the former case, with a smaller overall decrease of the objective functional and a higher degree of oscillations in the minimising sequences of parameters. This is due partly to the sparse distribution of tumour cells in the initial segmentation after surgery, and partly to the peritumoral infiltrations which may not be detectable by MRI data at the final time.

In conclusion, we proposed an optimization algorithm that allows a robust parameter estimation of a nonlinear diffuse interface model from neuroimaging data. The optimization is performed at low computational cost using an automated procedure that allows to solve the difficulties related the presence of a Cahn–Hilliard-type equation with single-well potential, non-conserved order parameter and degenerate mobility. These features open the path to the creation of an automated computational platform that may be integrated in clinical practice to run simulations from neuroimaging data, thus to assist medical doctors in evaluating patient-specific therapeutic options. Future developments will concern the patient-specific therapy optimization in a given temporal range and the assessment of uncertainty quantification of the underlying model.

Acknowledgements

6 Appendix

We report here the DEIM algorithm for the nonlinear term $\psi_1'(\phi)$ used to calculate the associated POD basis and row selection operator (see [11] for details):

Algorithm 2 DEIM Algorithm

Require: Assemble the matrix $\Psi_{1,ij} := \psi_1'^T(\phi_h^i)\psi_1'(\phi_h^j)$;

   Step A Compute the POD basis $\xi_1^{\psi_1'}, \dots, \xi_{N_{\psi'}^{\text{POD}}}^{\psi_1'}$ for Ψ_1;

   Step B $l \leftarrow \arg\max_{j=1,\dots,N_h} |\xi_1^{\psi_1'}(\mathbf{x}_j)|$;

   Step C $U_{\psi_1'} = [\xi_1^{\psi_1'}]$, $i = l$, $P_1 = [\vec{l}]$;

   for $j = 2, \dots, N_{\psi'}^{\text{POD}}$ **do**

   $u \leftarrow \xi_j^{\psi_1'}$;

   Solve $U_{\psi_1'i}c = u_i$; $r = u - U_{\psi_1'}c$;

   $l \leftarrow \arg\max_{j=1,\dots,N_h} |r(x_j)|$; $U_{\psi_1'} \leftarrow [U_{\psi_1'}, u]$; $P_1 = [P_1, \vec{l}]$,

---

where $\vec{l}$ is the finite element vector with value 1 on the node l and zero otherwise. In the same way, we obtain $U_{\psi_1''} = (\xi_1^{\psi_1''}, \dots, \xi_{N_{\psi''}^{\text{POD}}}^{\psi_1''})$ and P_2 for $\psi_1''(\phi)$.

We also report here the Newton method $\mathbf{RN}_k$ (17) used to solve (15). Let us define the second order tensors

$$B_{ml}(\vec{\alpha}_k^{n-1}) := \alpha_{ik}^{n-1}\alpha_{jk}^{n-1}\alpha_{sk}^{n-1}V_{2,ijsml} - 2\alpha_{ik}^{n-1}\alpha_{jk}^{n-1}V_{3,ijml} + \alpha_{ik}^{n-1}V_{4,iml},$$

$$K_{ml}(\vec{\alpha}_k^{n-1}) := \alpha_{ik}^{n-1}\alpha_{jk}^{n-1}\alpha_{sk}^{n-1}V_{8,ijsml} - 2\alpha_{ik}^{n-1}\alpha_{jk}^{n-1}V_{9,ijml} + \alpha_{ik}^{n-1}V_{10,iml},$$

$$V_{5,ml}(\vec{\alpha}_k^{n-1}) := \alpha_{ik}^{n-1}V_{5,iml} \quad V_{6,ml}(\vec{\alpha}_k^{n-1}) := \alpha_{ik}^{n-1}\alpha_{jk}^{n-1}V_{6,ijml},$$

$$V_{7,ml}(\vec{\alpha}_k^{n-1}) := \alpha_{ik}^{n-1}V_{7,iml} \quad U_{3,ml}(\vec{\alpha}_k^{n-1}) := \alpha_{ik}^{n-1}U_{3,iml} \quad W_{3,ml}(\vec{\alpha}_k^{n-1}) := \alpha_{ik}^{n-1}W_{3,iml}.$$

We use the following algorithm to solve the **ROM Newton** problem.

Algorithm 3 ROM Newton Algorithm

Initialisation

$$\vec{\eta}_k^n = \left[\frac{1}{\Delta t}W_1 + W_2 + (\delta_{nk} - S_{nk})W_3(\vec{\alpha}_k^{n-1}) + S_{nk}W_1\right]^{-1}\left(\frac{1}{\Delta t}W_1\vec{\eta}_k^{n-1} + S_{nk}W_4 - S_{nk}W_5\vec{\alpha}_k^{n-1}\right),$$

$$\vec{\alpha}_k^{n,0} = \vec{\alpha}_k^{n-1}, \vec{\beta}_k^{n,0} = \vec{\beta}_k^{n-1};$$

$$\text{error} = 1, \ p = 0.$$

while error $> 10^{-3}$ and $p < 1000$ **do**

  Assemble second order tensors:

$$U_{22,ml}(\vec{\alpha}_k^{n,p}) := (P_{2,ij}^T U_{\psi'',js})^{-1}\psi_1''(P_{2,sn}^T\Phi_{nh}\alpha_{hk}^{n,p})U_{22,iml},$$

$$C(\vec{\alpha}_k^{n,p}) := \gamma_k^2 U_1^{-1}U_6 + E_k c_{ek}U_1^{-1}U_{22}(\vec{\alpha}_k^{n,p}),$$

$$D(\vec{\alpha}_k^{n-1}, \vec{\alpha}_k^{n,p}, \vec{\beta}_k^{n,p}) := -U_1\vec{\beta}_k^{n,p} + \gamma_k^2 U_6\vec{\alpha}_k^{n,p} + E_k c_{ek}U_{21}(P_2^T U_{\psi'})^{-1}\psi_1'(P_2^T\Phi\alpha_k^{n,p}) - E_k U_3(\vec{\alpha}_k^{n-1})\vec{\alpha}_k^{n-1} - E_k c_{ek}U_4\vec{\alpha}_k^{n-1} - E_k c_{ek}U_5,$$

  Solve for first order variations:

$$d\vec{\alpha}_k = \left[\frac{V_1}{\Delta t} + L_k B(\vec{\alpha}_k^{n-1})C(\vec{\alpha}_k^{n,p})\right]^{-1}\left(-L_k B(\vec{\alpha}_k^{n-1})U_1^{-1}D(\vec{\alpha}_k^{n-1}, \vec{\alpha}_k^{n,p}, \vec{\beta}_k^{n,p}) - \frac{V_1}{\Delta t}\vec{\alpha}_k^{n,p} - L_k B(\vec{\alpha}_k^{n-1})\vec{\beta}_k^{n,p} + k_{nk}K(\vec{\alpha}_k^{n-1})\vec{\eta}_k^n + \nu_k(V_5(\vec{\alpha}_k^{n-1}) - V_6(\vec{\alpha}_k^{n-1}))\vec{\eta}_k^n + \left(\nu_k\delta_k(V_7(\vec{\alpha}_k^{n-1}) - V_1) + \frac{V_1}{\Delta t} - k_T V_1\right)\vec{\alpha}_k^{n-1}\right),$$

$$d\vec{\beta}_k = C(\vec{\alpha}_k^{n,p})d\vec{\alpha}_k + U_1^{-1}D(\vec{\alpha}_k^{n-1}, \vec{\alpha}_k^{n,p}, \vec{\beta}_k^{n,p}),$$

  Update the Newton iterations:

$$\vec{\alpha}_k^{n,p+1} = \vec{\alpha}_k^{n,p} + d\vec{\alpha}_k, \quad \vec{\beta}_k^{n,p+1} = \vec{\beta}_k^{n,p} + d\vec{\beta}_k$$

$$\text{error} = \sqrt{d\vec{\alpha}_k^T d\vec{\alpha}_k + d\vec{\beta}_k^T d\vec{\beta}_k},$$

$$p = p + 1.$$

  Update the time step:

$$\vec{\alpha}_k^n = \vec{\alpha}_k^{n,p+1}, \quad \vec{\beta}_k^n = \vec{\beta}_k^{n,p+1}.$$

We finally define the ROM linearised systems $\mathbf{RL}_k$ (18), obtained by varying $\mathcal{P}_k = \mathcal{P}_k + \delta\mathcal{P}$ in (19). Let us define the second order tensors

$$B'_{ml,\mathcal{P}_{kh}}\left(\vec{\alpha}_k^{n-1}, \frac{\partial\vec{\alpha}_k^{n-1}}{\partial\mathcal{P}_{kh}}\right) := 3\frac{\partial\alpha_{ik}^{n-1}}{\partial\mathcal{P}_{kh}}\alpha_{jk}^{n-1}\alpha_{sk}^{n-1}V_{2,ijsml} - 4\frac{\partial\alpha_{ik}^{n-1}}{\partial\mathcal{P}_{kh}}\alpha_{jk}^{n-1}V_{3,ijml} + \frac{\partial\alpha_{ik}^{n-1}}{\partial\mathcal{P}_{kh}}V_{4,iml},$$

$$K'_{ml,\mathcal{P}_{kh}}\left(\vec{\alpha}_k^{n-1}, \frac{\partial\vec{\alpha}_k^{n-1}}{\partial\mathcal{P}_{kh}}\right) := 3\frac{\partial\alpha_{ik}^{n-1}}{\partial\mathcal{P}_{kh}}\alpha_{jk}^{n-1}\alpha_{sk}^{n-1}V_{8,ijsml} - 4\frac{\partial\alpha_{ik}^{n-1}}{\partial\mathcal{P}_{kh}}\alpha_{jk}^{n-1}V_{9,ijml} + \frac{\partial\alpha_{ik}^{n-1}}{\partial\mathcal{P}_{kh}}V_{10,iml},$$

$$V'_{5,ml}\left(\frac{\partial\vec{\alpha}_k^{n-1}}{\partial\mathcal{P}_{kh}}\right) := \frac{\partial\alpha_{ik}^{n-1}}{\partial\mathcal{P}_{kh}}V_{5,iml}, \quad V'_{6,ml}\left(\vec{\alpha}_k^{n-1},\frac{\partial\vec{\alpha}_k^{n-1}}{\partial\mathcal{P}_{kh}}\right) := 2\frac{\partial\alpha_{ik}^{n-1}}{\partial\mathcal{P}_{kh}}\alpha_{jk}^{n-1}V_{6,ijml},$$

$$V'_{7,ml}\left(\frac{\partial\vec{\alpha}_k^{n-1}}{\partial\mathcal{P}_{kh}}\right) := \frac{\partial\alpha_{ik}^{n-1}}{\partial\mathcal{P}_{kh}}V_{7,iml}, \quad U'_{3,ml}\left(\frac{\partial\vec{\alpha}_k^{n-1}}{\partial\mathcal{P}_{kh}}\right) := \frac{\partial\alpha_{ik}^{n-1}}{\partial\mathcal{P}_{kh}}U_{3,iml}, \quad W'_{3,ml}\left(\frac{\partial\vec{\alpha}_k^{n-1}}{\partial\mathcal{P}_{kh}}\right) := \frac{\partial\alpha_{ik}^{n-1}}{\partial\mathcal{P}_{kh}}W_{3,iml}.$$

where $i,j,k,s,l,m = 1,\ldots,N_{\text{POD}}$ and $\mathcal{P}_{kh}$ is the $h-$th element of the set $\mathcal{P}_k$, with $h = 1,\ldots,|\mathcal{P}_k|$. Then we obtain the following **ROM** linearised systems, for $n = 0,\ldots,N$,

Linearised system for $\mathbf{L}_k \to \mathbf{L}_k + \delta\mathbf{L}$:

$$\begin{cases}
\dfrac{V_1}{\Delta t}\dfrac{\partial\vec{\alpha}_k^n}{\partial L_k} &= -L_k B(\vec{\alpha}_k^{n-1})\dfrac{\partial\vec{\beta}_k^n}{\partial L_k} - L_k B'_{L_k}\left(\vec{\alpha}_k^{n-1},\dfrac{\partial\vec{\alpha}_k^{n-1}}{\partial L_k}\right)\vec{\beta}_k^n - B(\vec{\alpha}_k^{n-1})\vec{\beta}_k^n + k_{nk}K(\vec{\alpha}_k^{n-1})\dfrac{\partial\vec{\eta}_k^n}{\partial L_k} + \\
&\quad k_{nk}K'\left(\vec{\alpha}_k^{n-1},\dfrac{\partial\vec{\alpha}_k^{n-1}}{\partial L_k}\right)\vec{\eta}_k^n + \nu_k\left(V'_5\left(\dfrac{\partial\vec{\alpha}_k^{n-1}}{\partial L_k}\right) - V'_6\left(\vec{\alpha}_k^{n-1},\dfrac{\partial\vec{\alpha}_k^{n-1}}{\partial L_k}\right)\right)\vec{\eta}_k^n + \\
&\quad \nu_k\left(V_5(\vec{\alpha}_k^{n-1}) - V_6(\vec{\alpha}_k^{n-1})\right)\dfrac{\partial\vec{\eta}_k^n}{\partial L_k} + \left(\nu_k\delta_k(V_7(\vec{\alpha}_k^{n-1}) - V_1) + \left(\dfrac{1}{\Delta t} - K_T\right)V_1\right)\dfrac{\partial\vec{\alpha}_k^{n-1}}{\partial L_k} + \\
&\quad \nu_k\delta_k V'_7\left(\dfrac{\partial\vec{\alpha}_k^{n-1}}{\partial L_k}\right)\vec{\alpha}_k^{n-1}, \\[2ex]
U_1\dfrac{\partial\vec{\beta}_k^n}{\partial L_k} &= \gamma_k^2 U_6\dfrac{\partial\vec{\alpha}_k^n}{\partial L_k} + E_k c_{ek}U_{22}(\vec{\alpha}_k^n)\dfrac{\partial\vec{\alpha}_k^n}{\partial L_k} - E_k U'_3\left(\dfrac{\partial\vec{\alpha}_k^{n-1}}{\partial L_k}\right)\vec{\alpha}_k^{n-1} - E_k U_3(\vec{\alpha}_k^{n-1})\dfrac{\partial\vec{\alpha}_k^{n-1}}{\partial L_k} - \\
&\quad E_k c_{ek}U_4\dfrac{\partial\vec{\alpha}_k^{n-1}}{\partial L_k}, \\[2ex]
\dfrac{W_1}{\Delta t}\dfrac{\partial\vec{\eta}_k^n}{\partial L_k} &= -W_2\dfrac{\partial\vec{\eta}_k^n}{\partial L_k} + (S_{nk} - \delta_{nk})W'_3\left(\dfrac{\partial\vec{\alpha}_k^{n-1}}{\partial L_k}\right)\vec{\eta}_k^n + \left((S_{nk} - \delta_{nk})W_3(\vec{\alpha}_k^{n-1}) - S_{nk}W_1\right)\dfrac{\partial\vec{\eta}_k^n}{\partial L_k} \\
&\quad -S_{nk}W_5\dfrac{\partial\vec{\alpha}_k^{n-1}}{\partial L_k} + \dfrac{W_1}{\Delta t}\dfrac{\partial\vec{\eta}_k^{n-1}}{\partial L_k}.
\end{cases} \tag{29}$$

Linearised system for $\boldsymbol{\nu}_k \to \boldsymbol{\nu}_k + \delta\boldsymbol{\nu}$:

$$\begin{cases}
\dfrac{V_1}{\Delta t}\dfrac{\partial\vec{\alpha}_k^n}{\partial\nu_k} &= -L_k B(\vec{\alpha}_k^{n-1})\dfrac{\partial\vec{\beta}_k^n}{\partial\nu_k} - L_k B'_{L_k}\left(\vec{\alpha}_k^{n-1},\dfrac{\partial\vec{\alpha}_k^{n-1}}{\partial\nu_k}\right)\vec{\beta}_k^n + k_{nk}K(\vec{\alpha}_k^{n-1})\dfrac{\partial\vec{\eta}_k^n}{\partial\nu_k} + \\
&\quad k_{nk}K'\left(\vec{\alpha}_k^{n-1},\dfrac{\partial\vec{\alpha}_k^{n-1}}{\partial\nu_k}\right)\vec{\eta}_k^n + \nu_k\left(V'_5\left(\dfrac{\partial\vec{\alpha}_k^{n-1}}{\partial\nu_k}\right) - V'_6\left(\vec{\alpha}_k^{n-1},\dfrac{\partial\vec{\alpha}_k^{n-1}}{\partial\nu_k}\right)\right)\vec{\eta}_k^n + \\
&\quad \nu_k\left(V_5(\vec{\alpha}_k^{n-1}) - V_6(\vec{\alpha}_k^{n-1})\right)\dfrac{\partial\vec{\eta}_k^n}{\partial\nu_k} + \left(\nu_k\delta_k(V_7(\vec{\alpha}_k^{n-1}) - V_1) + \left(\dfrac{1}{\Delta t} - K_T\right)V_1\right)\dfrac{\partial\vec{\alpha}_k^{n-1}}{\partial\nu_k} + \\
&\quad \nu_k\delta_k V'_7\left(\dfrac{\partial\vec{\alpha}_k^{n-1}}{\partial\nu_k}\right)\vec{\alpha}_k^{n-1} + \left(V_5(\vec{\alpha}_k^{n-1}) - V_6(\vec{\alpha}_k^{n-1})\right)\vec{\eta}_k^n + \delta_k(V_7(\vec{\alpha}_k^{n-1}) - V_1)\vec{\alpha}_k^{n-1}, \\[2ex]
U_1\dfrac{\partial\vec{\beta}_k^n}{\partial\nu_k} &= \gamma_k^2 U_6\dfrac{\partial\vec{\alpha}_k^n}{\partial\nu_k} + E_k c_{ek}U_{22}(\vec{\alpha}_k^n)\dfrac{\partial\vec{\alpha}_k^n}{\partial\nu_k} - E_k U'_3\left(\dfrac{\partial\vec{\alpha}_k^{n-1}}{\partial\nu_k}\right)\vec{\alpha}_k^{n-1} - E_k U_3(\vec{\alpha}_k^{n-1})\dfrac{\partial\vec{\alpha}_k^{n-1}}{\partial\nu_k} - \\
&\quad E_k c_{ek}U_4\dfrac{\partial\vec{\alpha}_k^{n-1}}{\partial\nu_k}, \\[2ex]
\dfrac{W_1}{\Delta t}\dfrac{\partial\vec{\eta}_k^n}{\partial\nu_k} &= -W_2\dfrac{\partial\vec{\eta}_k^n}{\partial\nu_k} + (S_{nk} - \delta_{nk})W'_3\left(\dfrac{\partial\vec{\alpha}_k^{n-1}}{\partial\nu_k}\right)\vec{\eta}_k^n + \left((S_{nk} - \delta_{nk})W_3(\vec{\alpha}_k^{n-1}) - S_{nk}W_1\right)\dfrac{\partial\vec{\eta}_k^n}{\partial\nu_k} \\
&\quad -S_{nk}W_5\dfrac{\partial\vec{\alpha}_k^{n-1}}{\partial\nu_k} + \dfrac{W_1}{\Delta t}\dfrac{\partial\vec{\eta}_k^{n-1}}{\partial\nu_k}.
\end{cases} \tag{30}$$

Linearised system for $\mathbf{k}_{nk} \to \mathbf{k}_{nk} + \delta\mathbf{k}_n$:

$$
\begin{cases}
\dfrac{V_1}{\Delta t}\dfrac{\partial\vec{\alpha}_k^n}{\partial k_{nk}} & = -L_k B(\vec{\alpha}_k^{n-1})\dfrac{\partial\vec{\beta}_k^n}{\partial k_{nk}} - L_k B'_{L_k}\left(\vec{\alpha}_k^{n-1},\dfrac{\partial\vec{\alpha}_k^{n-1}}{\partial k_{nk}}\right)\vec{\beta}_k^n + k_{nk}K(\vec{\alpha}_k^{n-1})\dfrac{\partial\vec{\eta}_k^n}{\partial k_{nk}} + \\[2mm]
& \quad k_{nk}K'\left(\vec{\alpha}_k^{n-1},\dfrac{\partial\vec{\alpha}_k^{n-1}}{\partial k_{nk}}\right)\vec{\eta}_k^n + K(\vec{\alpha}_k^{n-1})\vec{\eta}_k^n + \nu_k\left(V_5'\left(\dfrac{\partial\vec{\alpha}_k^{n-1}}{\partial k_{nk}}\right) - V_6'\left(\vec{\alpha}_k^{n-1},\dfrac{\partial\vec{\alpha}_k^{n-1}}{\partial k_{nk}}\right)\right)\vec{\eta}_k^n + \\[2mm]
& \quad \nu_k\big(V_5(\vec{\alpha}_k^{n-1}) - V_6(\vec{\alpha}_k^{n-1})\big)\dfrac{\partial\vec{\eta}_k^n}{\partial k_{nk}} + \left(\nu_k\delta_k(V_7(\vec{\alpha}_k^{n-1}) - V_1) + \left(\dfrac{1}{\Delta t} - K_T\right)V_1\right)\dfrac{\partial\vec{\alpha}_k^{n-1}}{\partial k_{nk}} + \\[2mm]
& \quad \nu_k\delta_k V_7'\left(\dfrac{\partial\vec{\alpha}_k^{n-1}}{\partial k_{nk}}\right)\vec{\alpha}_k^{n-1}, \\[4mm]
U_1\dfrac{\partial\vec{\beta}_k^n}{\partial k_{nk}} & = \gamma_k^2 U_6\dfrac{\partial\vec{\alpha}_k^n}{\partial k_{nk}} + E_k c_{ek}U_{22}(\vec{\alpha}_k^n)\dfrac{\partial\vec{\alpha}_k^n}{\partial k_{nk}} - E_k U_3'\left(\dfrac{\partial\vec{\alpha}_k^{n-1}}{\partial k_{nk}}\right)\vec{\alpha}_k^{n-1} - E_k U_3(\vec{\alpha}_k^{n-1})\dfrac{\partial\vec{\alpha}_k^{n-1}}{\partial k_{nk}} - \\[2mm]
& \quad E_k c_{ek}U_4\dfrac{\partial\vec{\alpha}_k^{n-1}}{\partial k_{nk}}, \\[4mm]
\dfrac{W_1}{\Delta t}\dfrac{\partial\vec{\eta}_k^n}{\partial k_{nk}} & = -W_2\dfrac{\partial\vec{\eta}_k^n}{\partial k_{nk}} + (S_{nk} - \delta_{nk})W_3'\left(\dfrac{\partial\vec{\alpha}_k^{n-1}}{\partial k_{nk}}\right)\vec{\eta}_k^n + \left((S_{nk} - \delta_{nk})W_3(\vec{\alpha}_k^{n-1}) - S_{nk}W_1\right)\dfrac{\partial\vec{\eta}_k^n}{\partial k_{nk}} \\[2mm]
& \quad - S_{nk}W_5\dfrac{\partial\vec{\alpha}_k^{n-1}}{\partial k_{nk}} + \dfrac{W_1}{\Delta t}\dfrac{\partial\vec{\eta}_k^{n-1}}{\partial k_{nk}}.
\end{cases}
\tag{31}
$$

Linearised system for $\mathbf{S}_{nk} \to \mathbf{S}_{nk} + \delta\mathbf{S}_n$:

$$
\begin{cases}
\dfrac{V_1}{\Delta t}\dfrac{\partial\vec{\alpha}_k^n}{\partial S_{nk}} & = -L_k B(\vec{\alpha}_k^{n-1})\dfrac{\partial\vec{\beta}_k^n}{\partial S_{nk}} - L_k B'_{L_k}\left(\vec{\alpha}_k^{n-1},\dfrac{\partial\vec{\alpha}_k^{n-1}}{\partial S_{nk}}\right)\vec{\beta}_k^n + k_{nk}K(\vec{\alpha}_k^{n-1})\dfrac{\partial\vec{\eta}_k^n}{\partial S_{nk}} + \\[2mm]
& \quad k_{nk}K'\left(\vec{\alpha}_k^{n-1},\dfrac{\partial\vec{\alpha}_k^{n-1}}{\partial S_{nk}}\right)\vec{\eta}_k^n + \nu_k\left(V_5'\left(\dfrac{\partial\vec{\alpha}_k^{n-1}}{\partial S_{nk}}\right) - V_6'\left(\vec{\alpha}_k^{n-1},\dfrac{\partial\vec{\alpha}_k^{n-1}}{\partial S_{nk}}\right)\right)\vec{\eta}_k^n + \\[2mm]
& \quad \nu_k\big(V_5(\vec{\alpha}_k^{n-1}) - V_6(\vec{\alpha}_k^{n-1})\big)\dfrac{\partial\vec{\eta}_k^n}{\partial S_{nk}} + \left(\nu_k\delta_k(V_7(\vec{\alpha}_k^{n-1}) - V_1) + \left(\dfrac{1}{\Delta t} - K_T\right)V_1\right)\dfrac{\partial\vec{\alpha}_k^{n-1}}{\partial S_{nk}} + \\[2mm]
& \quad \nu_k\delta_k V_7'\left(\dfrac{\partial\vec{\alpha}_k^{n-1}}{\partial S_{nk}}\right)\vec{\alpha}_k^{n-1}, \\[4mm]
U_1\dfrac{\partial\vec{\beta}_k^n}{\partial S_{nk}} & = \gamma_k^2 U_6\dfrac{\partial\vec{\alpha}_k^n}{\partial S_{nk}} + E_k c_{ek}U_{22}(\vec{\alpha}_k^n)\dfrac{\partial\vec{\alpha}_k^n}{\partial S_{nk}} - E_k U_3'\left(\dfrac{\partial\vec{\alpha}_k^{n-1}}{\partial S_{nk}}\right)\vec{\alpha}_k^{n-1} - E_k U_3(\vec{\alpha}_k^{n-1})\dfrac{\partial\vec{\alpha}_k^{n-1}}{\partial S_{nk}} - \\[2mm]
& \quad E_k c_{ek}U_4\dfrac{\partial\vec{\alpha}_k^{n-1}}{\partial S_{nk}}, \\[4mm]
\dfrac{W_1}{\Delta t}\dfrac{\partial\vec{\eta}_k^n}{\partial S_{nk}} & = -W_2\dfrac{\partial\vec{\eta}_k^n}{\partial S_{nk}} + (S_{nk} - \delta_{nk})W_3'\left(\dfrac{\partial\vec{\alpha}_k^{n-1}}{\partial S_{nk}}\right)\vec{\eta}_k^n + \left((S_{nk} - \delta_{nk})W_3(\vec{\alpha}_k^{n-1}) - S_{nk}W_1\right)\dfrac{\partial\vec{\eta}_k^n}{\partial S_{nk}} \\[2mm]
& \quad - S_{nk}W_5\dfrac{\partial\vec{\alpha}_k^{n-1}}{\partial S_{nk}} + \dfrac{W_1}{\Delta t}\dfrac{\partial\vec{\eta}_k^{n-1}}{\partial S_{nk}} + W_4 - W_5\vec{\alpha}_k^{n-1} + (W_3(\vec{\alpha}_k^{n-1}) - W_1)\vec{\eta}_k^n.
\end{cases}
\tag{32}
$$

Linearised system for $\boldsymbol{\delta}_{nk} \to \boldsymbol{\delta}_{nk} + \delta\boldsymbol{\delta}_n$:

$$
\begin{cases}
\dfrac{V_1}{\Delta t}\dfrac{\partial \vec{\alpha}_k^n}{\partial \delta_{nk}} &= -L_k B(\vec{\alpha}_k^{n-1})\dfrac{\partial \vec{\beta}_k^n}{\partial \delta_{nk}} - L_k B'_{L_k}\left(\vec{\alpha}_k^{n-1}, \dfrac{\partial \vec{\alpha}_k^{n-1}}{\partial \delta_{nk}}\right)\vec{\beta}_k^n + k_{nk}K(\vec{\alpha}_k^{n-1})\dfrac{\partial \vec{\eta}_k^n}{\partial \delta_{nk}} + \\[2mm]
& \quad k_{nk}K'\left(\vec{\alpha}_k^{n-1}, \dfrac{\partial \vec{\alpha}_k^{n-1}}{\partial \delta_{nk}}\right)\vec{\eta}_k^n + \nu_k\left(V_5'\left(\dfrac{\partial \vec{\alpha}_k^{n-1}}{\partial \delta_{nk}}\right) - V_6'\left(\vec{\alpha}_k^{n-1}, \dfrac{\partial \vec{\alpha}_k^{n-1}}{\partial \delta_{nk}}\right)\right)\vec{\eta}_k^n + \\[2mm]
& \quad \nu_k\left(V_5(\vec{\alpha}_k^{n-1}) - V_6(\vec{\alpha}_k^{n-1})\right)\dfrac{\partial \vec{\eta}_k^n}{\partial \delta_{nk}} + \left(\nu_k\delta_k(V_7(\vec{\alpha}_k^{n-1}) - V_1) + \left(\dfrac{1}{\Delta t} - K_T\right)V_1\right)\dfrac{\partial \vec{\alpha}_k^{n-1}}{\partial \delta_{nk}} + \\[2mm]
& \quad \nu_k\delta_k V_7'\left(\dfrac{\partial \vec{\alpha}_k^{n-1}}{\partial \delta_{nk}}\right)\vec{\alpha}_k^{n-1}, \\[4mm]
U_1\dfrac{\partial \vec{\beta}_k^n}{\partial \delta_{nk}} &= \gamma_k^2 U_6\dfrac{\partial \vec{\alpha}_k^n}{\partial \delta_{nk}} + E_k c_{ek} U_{22}(\vec{\alpha}_k^n)\dfrac{\partial \vec{\alpha}_k^n}{\partial \delta_{nk}} - E_k U_3'\left(\dfrac{\partial \vec{\alpha}_k^{n-1}}{\partial \delta_{nk}}\right)\vec{\alpha}_k^{n-1} - E_k U_3(\vec{\alpha}_k^{n-1})\dfrac{\partial \vec{\alpha}_k^{n-1}}{\partial \delta_{nk}} - \\[2mm]
& \quad E_k c_{ek} U_4 \dfrac{\partial \vec{\alpha}_k^{n-1}}{\partial \delta_{nk}}, \\[4mm]
\dfrac{W_1}{\Delta t}\dfrac{\partial \vec{\eta}_k^n}{\partial \delta_{nk}} &= -W_2\dfrac{\partial \vec{\eta}_k^n}{\partial \delta_{nk}} + (S_{nk} - \delta_{nk})W_3'\left(\dfrac{\partial \vec{\alpha}_k^{n-1}}{\partial \delta_{nk}}\right)\vec{\eta}_k^n + \left((S_{nk} - \delta_{nk})W_3(\vec{\alpha}_k^{n-1}) - S_{nk}W_1\right)\dfrac{\partial \vec{\eta}_k^n}{\partial \delta_{nk}} \\[2mm]
& \quad -S_{nk}W_5\dfrac{\partial \vec{\alpha}_k^{n-1}}{\partial \delta_{nk}} + \dfrac{W_1}{\Delta t}\dfrac{\partial \vec{\eta}_k^{n-1}}{\partial \delta_{nk}} - W_3(\vec{\alpha}_k^{n-1})\vec{\eta}_k^n.
\end{cases}
\tag{33}
$$

Linearised system for $\boldsymbol{\gamma}_k \to \boldsymbol{\gamma}_k + \delta\boldsymbol{\gamma}$:

$$
\begin{cases}
\dfrac{V_1}{\Delta t}\dfrac{\partial \vec{\alpha}_k^n}{\partial \gamma_k^2} &= -L_k B(\vec{\alpha}_k^{n-1})\dfrac{\partial \vec{\beta}_k^n}{\partial \gamma_k^2} - L_k B'_{L_k}\left(\vec{\alpha}_k^{n-1}, \dfrac{\partial \vec{\alpha}_k^{n-1}}{\partial \gamma_k^2}\right)\vec{\beta}_k^n + k_{nk}K(\vec{\alpha}_k^{n-1})\dfrac{\partial \vec{\eta}_k^n}{\partial \gamma_k^2} + \\[2mm]
& \quad k_{nk}K'\left(\vec{\alpha}_k^{n-1}, \dfrac{\partial \vec{\alpha}_k^{n-1}}{\partial \gamma_k^2}\right)\vec{\eta}_k^n + \nu_k\left(V_5'\left(\dfrac{\partial \vec{\alpha}_k^{n-1}}{\partial \gamma_k^2}\right) - V_6'\left(\vec{\alpha}_k^{n-1}, \dfrac{\partial \vec{\alpha}_k^{n-1}}{\partial \gamma_k^2}\right)\right)\vec{\eta}_k^n + \\[2mm]
& \quad \nu_k\left(V_5(\vec{\alpha}_k^{n-1}) - V_6(\vec{\alpha}_k^{n-1})\right)\dfrac{\partial \vec{\eta}_k^n}{\partial \gamma_k^2} + \left(\nu_k\delta_k(V_7(\vec{\alpha}_k^{n-1}) - V_1) + \left(\dfrac{1}{\Delta t} - K_T\right)V_1\right)\dfrac{\partial \vec{\alpha}_k^{n-1}}{\partial \gamma_k^2} + \\[2mm]
& \quad \nu_k\delta_k V_7'\left(\dfrac{\partial \vec{\alpha}_k^{n-1}}{\partial \gamma_k^2}\right)\vec{\alpha}_k^{n-1}, \\[4mm]
U_1\dfrac{\partial \vec{\beta}_k^n}{\partial \gamma_k^2} &= \gamma_k^2 U_6\dfrac{\partial \vec{\alpha}_k^n}{\partial \gamma_k^2} + E_k c_{ek} U_{22}(\vec{\alpha}_k^n)\dfrac{\partial \vec{\alpha}_k^n}{\partial \gamma_k^2} - E_k U_3'\left(\dfrac{\partial \vec{\alpha}_k^{n-1}}{\partial \gamma_k^2}\right)\vec{\alpha}_k^{n-1} - E_k U_3(\vec{\alpha}_k^{n-1})\dfrac{\partial \vec{\alpha}_k^{n-1}}{\partial \gamma_k^2} - \\[2mm]
& \quad E_k c_{ek} U_4 \dfrac{\partial \vec{\alpha}_k^{n-1}}{\partial \gamma_k^2} + U_6\vec{\alpha}_k^n, \\[4mm]
\dfrac{W_1}{\Delta t}\dfrac{\partial \vec{\eta}_k^n}{\partial \gamma_k^2} &= -W_2\dfrac{\partial \vec{\eta}_k^n}{\partial \gamma_k^2} + (S_{nk} - \delta_{nk})W_3'\left(\dfrac{\partial \vec{\alpha}_k^{n-1}}{\partial \gamma_k^2}\right)\vec{\eta}_k^n + \left((S_{nk} - \delta_{nk})W_3(\vec{\alpha}_k^{n-1}) - S_{nk}W_1\right)\dfrac{\partial \vec{\eta}_k^n}{\partial \gamma_k^2} \\[2mm]
& \quad -S_{nk}W_5\dfrac{\partial \vec{\alpha}_k^{n-1}}{\partial \gamma_k^2} + \dfrac{W_1}{\Delta t}\dfrac{\partial \vec{\eta}_k^{n-1}}{\partial \gamma_k^2}.
\end{cases}
\tag{34}
$$

Linearised system for $\mathbf{E}_k \to \mathbf{E}_k + \delta\mathbf{E}$:

$$
\begin{cases}
\begin{aligned}
\dfrac{V_1}{\Delta t}\dfrac{\partial \vec{\alpha}_k^n}{\partial E_k} &= -L_k B(\vec{\alpha}_k^{n-1})\dfrac{\partial \vec{\beta}_k^n}{\partial E_k} - L_k B'_{L_k}\left(\vec{\alpha}_k^{n-1}, \dfrac{\partial \vec{\alpha}_k^{n-1}}{\partial E_k}\right)\vec{\beta}_k^n + k_{nk}K(\vec{\alpha}_k^{n-1})\dfrac{\partial \vec{\eta}_k^n}{\partial E_k} + \\
&\quad k_{nk}K'\left(\vec{\alpha}_k^{n-1}, \dfrac{\partial \vec{\alpha}_k^{n-1}}{\partial E_k}\right)\vec{\eta}_k^n + \nu_k\left(V_5'\left(\dfrac{\partial \vec{\alpha}_k^{n-1}}{\partial E_k}\right) - V_6'\left(\vec{\alpha}_k^{n-1}, \dfrac{\partial \vec{\alpha}_k^{n-1}}{\partial E_k}\right)\right)\vec{\eta}_k^n + \\
&\quad \nu_k\left(V_5(\vec{\alpha}_k^{n-1}) - V_6(\vec{\alpha}_k^{n-1})\right)\dfrac{\partial \vec{\eta}_k^n}{\partial E_k} + \left(\nu_k\delta_k(V_7(\vec{\alpha}_k^{n-1}) - V_1) + \left(\dfrac{1}{\Delta t} - K_T\right)V_1\right)\dfrac{\partial \vec{\alpha}_k^{n-1}}{\partial E_k} + \\
&\quad \nu_k\delta_k V_7'\left(\dfrac{\partial \vec{\alpha}_k^{n-1}}{\partial E_k}\right)\vec{\alpha}_k^{n-1},
\end{aligned}\\[2em]
\begin{aligned}
U_1\dfrac{\partial \vec{\beta}_k^n}{\partial E_k} &= \gamma_k^2 U_6\dfrac{\partial \vec{\alpha}_k^n}{\partial E_k} + E_k c_{ek}U_{22}(\vec{\alpha}_k^n)\dfrac{\partial \vec{\alpha}_k^n}{\partial E_k} - E_k U_3'\left(\dfrac{\partial \vec{\alpha}_k^{n-1}}{\partial E_k}\right)\vec{\alpha}_k^{n-1} - E_k U_3(\vec{\alpha}_k^{n-1})\dfrac{\partial \vec{\alpha}_k^{n-1}}{\partial E_k} - \\
&\quad E_k c_{ek}U_4\dfrac{\partial \vec{\alpha}_k^{n-1}}{\partial E_k} + c_{ek}U_{21}(P_2^T U_{\psi'})^{-1}\psi_1'(P_2^T\Phi\alpha_k^n) - (U_3(\vec{\alpha}_k^{n-1}) + c_{ek}U_4)\vec{\alpha}_k^{n-1} - \\
&\quad c_{ek}U_5,
\end{aligned}\\[2em]
\begin{aligned}
\dfrac{W_1}{\Delta t}\dfrac{\partial \vec{\eta}_k^n}{\partial E_k} &= -W_2\dfrac{\partial \vec{\eta}_k^n}{\partial E_k} + (S_{nk} - \delta_{nk})W_3'\left(\dfrac{\partial \vec{\alpha}_k^{n-1}}{\partial E_k}\right)\vec{\eta}_k^n + \left((S_{nk} - \delta_{nk})W_3(\vec{\alpha}_k^{n-1}) - S_{nk}W_1\right)\dfrac{\partial \vec{\eta}_k^n}{\partial E_k} \\
&\quad -S_{nk}W_5\dfrac{\partial \vec{\alpha}_k^{n-1}}{\partial E_k} + \dfrac{W_1}{\Delta t}\dfrac{\partial \vec{\eta}_k^{n-1}}{\partial E_k}.
\end{aligned}
\end{cases}
\tag{35}
$$

Linearised system for $\boldsymbol{\delta}_k \to \boldsymbol{\delta}_k + \delta\boldsymbol{\delta}$:

$$
\begin{cases}
\begin{aligned}
\dfrac{V_1}{\Delta t}\dfrac{\partial \vec{\alpha}_k^n}{\partial \delta_k} &= -L_k B(\vec{\alpha}_k^{n-1})\dfrac{\partial \vec{\beta}_k^n}{\partial \delta_k} - L_k B'_{L_k}\left(\vec{\alpha}_k^{n-1}, \dfrac{\partial \vec{\alpha}_k^{n-1}}{\partial \delta_k}\right)\vec{\beta}_k^n + k_{nk}K(\vec{\alpha}_k^{n-1})\dfrac{\partial \vec{\eta}_k^n}{\partial \delta_k} + \\
&\quad k_{nk}K'\left(\vec{\alpha}_k^{n-1}, \dfrac{\partial \vec{\alpha}_k^{n-1}}{\partial \delta_k}\right)\vec{\eta}_k^n + \nu_k\left(V_5'\left(\dfrac{\partial \vec{\alpha}_k^{n-1}}{\partial \delta_k}\right) - V_6'\left(\vec{\alpha}_k^{n-1}, \dfrac{\partial \vec{\alpha}_k^{n-1}}{\partial \delta_k}\right)\right)\vec{\eta}_k^n + \\
&\quad \nu_k\left(V_5(\vec{\alpha}_k^{n-1}) - V_6(\vec{\alpha}_k^{n-1})\right)\dfrac{\partial \vec{\eta}_k^n}{\partial \delta_k} + \left(\nu_k\delta_k(V_7(\vec{\alpha}_k^{n-1}) - V_1) + \left(\dfrac{1}{\Delta t} - K_T\right)V_1\right)\dfrac{\partial \vec{\alpha}_k^{n-1}}{\partial \delta_k} + \\
&\quad \nu_k\delta_k V_7'\left(\dfrac{\partial \vec{\alpha}_k^{n-1}}{\partial \delta_k}\right)\vec{\alpha}_k^{n-1} + \nu_k(V_7(\vec{\alpha}_k^{n-1}) - V_1)\vec{\alpha}_k^{n-1},
\end{aligned}\\[2em]
\begin{aligned}
U_1\dfrac{\partial \vec{\beta}_k^n}{\partial \delta_k} &= \gamma_k^2 U_6\dfrac{\partial \vec{\alpha}_k^n}{\partial \delta_k} + E_k c_{ek}U_{22}(\vec{\alpha}_k^n)\dfrac{\partial \vec{\alpha}_k^n}{\partial \delta_k} - E_k U_3'\left(\dfrac{\partial \vec{\alpha}_k^{n-1}}{\partial \delta_k}\right)\vec{\alpha}_k^{n-1} - E_k U_3(\vec{\alpha}_k^{n-1})\dfrac{\partial \vec{\alpha}_k^{n-1}}{\partial \delta_k} - \\
&\quad E_k c_{ek}U_4\dfrac{\partial \vec{\alpha}_k^{n-1}}{\partial \delta_k},
\end{aligned}\\[2em]
\begin{aligned}
\dfrac{W_1}{\Delta t}\dfrac{\partial \vec{\eta}_k^n}{\partial \delta_k} &= -W_2\dfrac{\partial \vec{\eta}_k^n}{\partial \delta_k} + (S_{nk} - \delta_{nk})W_3'\left(\dfrac{\partial \vec{\alpha}_k^{n-1}}{\partial \delta_k}\right)\vec{\eta}_k^n + \left((S_{nk} - \delta_{nk})W_3(\vec{\alpha}_k^{n-1}) - S_{nk}W_1\right)\dfrac{\partial \vec{\eta}_k^n}{\partial \delta_k} \\
&\quad -S_{nk}W_5\dfrac{\partial \vec{\alpha}_k^{n-1}}{\partial \delta_k} + \dfrac{W_1}{\Delta t}\dfrac{\partial \vec{\eta}_k^{n-1}}{\partial \delta_k}.
\end{aligned}
\end{cases}
\tag{36}
$$

Linearised system for $\mathbf{c}_{ek} \to \mathbf{c}_{ek} + \delta\mathbf{c}_e$:

$$
\begin{cases}
\dfrac{V_1}{\Delta t}\dfrac{\partial \vec{\alpha}_k^n}{\partial c_{ek}} &= -L_k B(\vec{\alpha}_k^{n-1})\dfrac{\partial \vec{\beta}_k^n}{\partial c_{ek}} - L_k B'_{L_k}\left(\vec{\alpha}_k^{n-1}, \dfrac{\partial \vec{\alpha}_k^{n-1}}{\partial c_{ek}}\right)\vec{\beta}_k^n + k_{nk}K(\vec{\alpha}_k^{n-1})\dfrac{\partial \vec{\eta}_k^n}{\partial c_{ek}} + \\[2mm]
& k_{nk}K'\left(\vec{\alpha}_k^{n-1}, \dfrac{\partial \vec{\alpha}_k^{n-1}}{\partial c_{ek}}\right)\vec{\eta}_k^n + \nu_k\left(V_5'\left(\dfrac{\partial \vec{\alpha}_k^{n-1}}{\partial c_{ek}}\right) - V_6'\left(\vec{\alpha}_k^{n-1}, \dfrac{\partial \vec{\alpha}_k^{n-1}}{\partial c_{ek}}\right)\right)\vec{\eta}_k^n + \\[2mm]
& \nu_k\left(V_5(\vec{\alpha}_k^{n-1}) - V_6(\vec{\alpha}_k^{n-1})\right)\dfrac{\partial \vec{\eta}_k^n}{\partial c_{ek}} + \left(\nu_k\delta_k(V_7(\vec{\alpha}_k^{n-1}) - V_1) + \left(\dfrac{1}{\Delta t} - K_T\right)V_1\right)\dfrac{\partial \vec{\alpha}_k^{n-1}}{\partial c_{ek}} + \\[2mm]
& \nu_k\delta_k V_7'\left(\dfrac{\partial \vec{\alpha}_k^{n-1}}{\partial c_{ek}}\right)\vec{\alpha}_k^{n-1}, \\[4mm]

U_1\dfrac{\partial \vec{\beta}_k^n}{\partial c_{ek}} &= \gamma_k^2 U_6\dfrac{\partial \vec{\alpha}_k^n}{\partial c_{ek}} + E_k c_{ek}U_{22}(\vec{\alpha}_k^n)\dfrac{\partial \vec{\alpha}_k^n}{\partial c_{ek}} - E_k U_3'\left(\dfrac{\partial \vec{\alpha}_k^{n-1}}{\partial c_{ek}}\right)\vec{\alpha}_k^{n-1} - E_k U_3(\vec{\alpha}_k^{n-1})\dfrac{\partial \vec{\alpha}_k^{n-1}}{\partial c_{ek}} - \\[2mm]
& E_k c_{ek}U_4\dfrac{\partial \vec{\alpha}_k^{n-1}}{\partial c_{ek}} + E_k U_{21}(P_2^T U_{\psi'})^{-1}\psi_1'(P_2^T\Phi\alpha_k^n) - E_k U_4\vec{\alpha}_k^{n-1} - E_k U_5, \\[4mm]

\dfrac{W_1}{\Delta t}\dfrac{\partial \vec{\eta}_k^n}{\partial c_{ek}} &= -W_2\dfrac{\partial \vec{\eta}_k^n}{\partial c_{ek}} + (S_{nk} - \delta_{nk})W_3'\left(\dfrac{\partial \vec{\alpha}_k^{n-1}}{\partial c_{ek}}\right)\vec{\eta}_k^n + \left((S_{nk} - \delta_{nk})W_3(\vec{\alpha}_k^{n-1}) - S_{nk}W_1\right)\dfrac{\partial \vec{\eta}_k^n}{\partial c_{ek}} \\[2mm]
& -S_{nk}W_5\dfrac{\partial \vec{\alpha}_k^{n-1}}{\partial c_{ek}} + \dfrac{W_1}{\Delta t}\dfrac{\partial \vec{\eta}_k^{n-1}}{\partial c_{ek}};
\end{cases}
\tag{37}
$$

References

[1] K. Afanasiev and M. Hinze. Adaptive control of a wake flow using proper orthogonal decomposition. *Lecture Notes in Pure and Applied Mathematics*, 216:317–332, 2001.

[2] A. Agosti, C. Cattaneo, C. Giverso, D. Ambrosi, and P. Ciarletta. A computational framework for the personalized clinical treatment of glioblastoma multiforme. *ZAMM*, 98(12):2307–2327, 2018.

[3] A. Agosti, C. Giverso, E. Faggiano, A. Stamm, and P. Ciarletta. A personalized mathematical tool for neuro-oncology: a clinical case study. *International Journal of Nonlinear Mechanics*, 107:170–181, 2018.

[4] J. C. L. Alfonso, K. Talkenberger, M. Seifert, B. Klink, A. Hawkins-Daarud, K. R. Swanson, H. Hatzikirou, and A. Deutsch. The biology and mathematical modelling of glioma invasion: a review. *Journal of the Royal Society Interface*, 14(136):20170490, 2017.

[5] J. W. Barrett, J. F. Blowey, and H. Garcke. Finite element approximation of the Cahn-Hilliard equation with degenerate mobility. *SIAM J. Numer. Anal.*, 37(1):286–318, 1999.

[6] B. Bedogni and M. B. Powell. Hypoxia, melanocytes and melanoma survival and tumor development in the permissive microenvironment of the skin. *Pigment Cell Melanoma Res.*, 22:166–174, 2009.

[7] F. Bernis and A. Friedman. Higher order nonlinear degenerate parabolic equations. *J. Differential Equations*, 83:179–206, 1990.

[8] M. Bruehlmeier, U. Roelcke, P. Bläuenstein, J. Missimer, P. A. Schubiger, J. Th. Locher, R. Pellikka, and S. M. Ametamey. Measurement of the extracellular space in brain tumors using ^{76}br-bromide and pet. *J. Nucl. Med.*, 44(8):1210–1218, 2003.

[9] H. Byrne and L. Preziosi. Modelling solid tumour growth using the theory of mixtures. *Math. Med. Biol.*, 20(4):341–366, 2003.

[10] C. Chatelain, T. Balois, P. Ciarletta, and M. Ben Amar. Emergence of microstructural patterns in skin cancer: a phase separation analysis in a binary mixture. *New J. Phys.*, 115013(13):21pp, 2011.

[11] S. Chaturantabut and D. C. Sorensen. Nonlinear model reduction via discrete empirical interpolation. *SIAM J. Sci. Comput.*, 32:2737–2764, 2010.

[12] O. Clatz, M. Sermesant, P. Bondiau, H. Delingette, S. K. Warfield, G. Malandain, and N. Ayache. Realistic simulation of the 3d growth of brain tumors in mr images coupling diffusion with biomechanical deformation. *IEEE Trans. Med. Imaging*, 24(10):1334–1346, 2005.

[13] Christian Engwer, Thomas Hillen, Markus Knappitsch, and Christina Surulescu. Glioma follow white matter tracts: a multiscale DTI–based model. *J. Math. Biol.*, 71(3):551–582, 2015.

[14] Christian Engwer, Alexander Hunt, and Christina Surulescu. Effective equations for anisotropic glioma spread with proliferation: a multiscale approach and comparisons with previous settings. *Math. Med. Biol.*, 33(4):435–459, 2016.

[15] R. M. Ford and D. A. Lauffenburger. Analysis of chemotactic bacterial distributions in population migration assays using a mathematical model applicable to steep or shallow attractant gradients. *Bull. Math. Biol.*, 53(5):721–749, 1991.

[16] J. F. Fowler. The linear-quadratic formula and progress in fractionated radiotherapy. *Br. J. Radiol.*, 62:679–694, 1989.

[17] H. B. Frieboes, J. S. Lowengrub, S. Wise, X. Zheng, P. Macklin, E. L. Bearer, and V. Cristini. Computer simulation of glioma growth and morphology. *NeuroImage*, 37:S59–S70, 2007.

[18] M. Fritz, E. A. B. F. Lima, J. T. Oden, and B. Wohlmuth. On the unsteady Darcy-Forchheimer-Brinkman equation in local and nonlocal tumor growth models. *arXiv:1812.08872v2*, 2019.

[19] H. Garcke, K. F. Lam, E. Sitka, and V. Styles. A Cahn-Hilliard-Darcy model for tumour growth with chemotaxis and active transport. *Math. Models Methods Appl. Sci.*, 26(6):1095–1148, 2016.

[20] C. Gräßle and M. Hinze. Pod reduced order modeling for evolution equations utilizing arbitrary finite element discretizations. *Advances in Computational Mathematics*, 44(6):1941–1978, 2018.

[21] C. Gräßle, M. Hinze, and M. Scharmacher. POD for optimal control of the Cahn-Hilliard system using spatially adapted snapshots. *Numerical Mathematics and Advanced Applications ENUMATH 2017. Lecture Notes in Computational Science and Engineering. Springer, Cham.*, 126, 2019.

[22] H. Hatzikirou, A. Deutsch, C. Schaller, M. Simon, and K. R. Swanson. Mathematical modelling of glioblastoma tumour development: a review. *Mathematical Models and Methods in Applied Science*, 15(11):1779–1794, 2005.

[23] A. Hawkins-Daarud, S. Prudhomme, K. G. van der Zee, and J. T. Oden. Bayesian calibration, validation, and uncertainty quantification of diffuse interface models of tumor growth. *Journal of mathematical biology*, 67(6–7):1457–1485, 2013.

[24] P. R. Jackson, J. Juliano, A. Hawkins-Daarud, R. C. Rockne, and K. R. Swanson. Patient-specific mathematical neuro-oncology: using a simple proliferation and invasion tumor model to inform clinical practice. *Bulletin of mathematical biology*, 77(5):846–856, 2015.

[25] T. Jackson, N. Komarova, and K. R. Swanson. Mathematical oncology: using mathematics to enable cancer discoveries. *The American Mathematical Monthly*, 121(9):840–856, 2014.

[26] S. Jbabdi, E. Mandonnet, H. Duffau, L. Capelle, K. R. Swanson, M. Pélégrini-Issac, R. Guillevin, and H. Benali. Simulation of anisotropic growth of low-grade gliomas using diffusion tensor imaging. *Magnetic Resonance in Medicine: An Official Journal of the International Society for Magnetic Resonance in Medicine*, 54(3):616–624, 2005.

[27] C. T. Kelley. *Iterative Methods for Optimization.* SIAM, 1999.

[28] R. Leece, J. Xu, Q.T. Ostrom, Y. Chen, C. Kruchko, and J.S. Barnholtz-Sloan. Global incidence of 473 malignant brain and other central nervous system tumors by histology. *Neuro. Oncol.*, 19(474):1553–1564, 2017.

[29] R. Lipkova and et al. Personalized radiotherapy design for glioblastoma: Integrating mathematical tumor models, multimodal scan and bayesian inference. *IEEE Transactions on Medical Imaging*, 38(8):1875–1884, 2019.

[30] Z.Q. Luo, J.S. Pang, and D. Ralph. *Mathematical Programs with Equilibrium Constraints*. Cambridge University Press, UK, 1997.

[31] A. Martinez-Gonzalez, G. F. Calvo, L. A. Perez, and V. M. Perez-Garcia. Hypoxic cell waves around necrotic cores in glioblastoma: A biomathematical model and its therapeutic implications. *Bull. Math. Biol.*, 74(12):2875–2896, 2012.

[32] P. Mascheroni, C. Stigliano, M. Carfagna, D.P. Boso, L. Preziosi, P. Decuzzi, and B.A. Schrefler. Predicting the growth of glioblastoma multiforme spheroids using a multiphase porous media model. *Biomech. Model. Mechanobiol.*, 15:1215–1228, 2016.

[33] R. Mirnezami, J. Nicholson, and A. Darzi. Preparing for precision medicine. *New England Journal of Medicine*, 6(366):489–491, 2012.

[34] Q.T. Ostrom, H. Gittleman, G. Truitt, A. Boscia, C. Kruchko, and J.S. Barnholtz-Sloan. Cbtrus statistical 470 report: Primary brain and other central nervous system tumors diagnosed in the United States in 471 20112015. *Neuro. Oncol.*, 20:iv1–iv86, 2018.

[35] S. Pagani, A. Manzoni, and A. Quarteroni. Numerical approximation of parametrized problems in cardiac electrophysiology by a local reduced basis method. *Comput. Methods Appl. Mech. Engrg.*, 340:530–558, 2018.

[36] K. J. Painter and T. Hillen. Mathematical modelling of glioma growth: the use of diffusion tensor imaging (dti) data to predict the anisotropic pathways of cancer invasion. *Journal of Theoretical Biology*, 323:25–39, 2013.

[37] G. Powathil, M. Kohandel, S. Sivaloganathan, A. Oza, and M. Milosevic. Mathematical modeling of brain tumors: effects of radiotherapy and chemotherapy. *Phys. Med. Biol.*, 52:3291–3306, 2007.

[38] M. D. Prados, S. A. Byron, N. L. Tran, J. J. Phillips, A. M. Molinaro, K. L. Ligon, P. Y. Wen, J. G. Kuhn, I. K. Mellinghoff, J. F. De Groot, et al. Toward precision medicine in glioblastoma: the promise and the challenges. *Neuro-Oncology*, 17(8):1051–1063, 2015.

[39] L. Preziosi and A. Tosin. Multiphase modelling of tumour growth and extracellular matrix interaction: mathematical tools and applications. *Journal of Mathematical Biology*, 58(4–5):625, 2009.

[40] R. Rockne, E. C. Alvord Jr, J. K. Rockhill, and K. R. Swanson. A mathematical model for brain tumor response to radiation therapy. *J. Math. Biol.*, 58:561–578, 2009.

[41] R. Rockne, J. K. Rockhill, M. Mrugala, A. M. Spence, I. Kalet, K. Hendrickson, A. Lai, T. Cloughesy, E. C. Alvord Jr, and K. R. Swanson. Predicting the efficacy of radiotherapy in individual glioblastoma patients in vivo: a mathematical modeling approach. *Physics in Medicine & Biology*, 55(12):3271, 2010.

[42] R. K. Sachs, L. R. Hlatky, and P. Hahnfeldt. Simple ode models of tumor growth and anti-angiogenic or radiation treatment. *Math. Comput. Model.*, 33:1297–1305, 2001.

[43] R. Stupp and et al. Radiotherapy plus concomitant and adjuvant temozolomide for glioblastoma. *N. Engl. J. Med.*, 352:987–996, 2005.

[44] E. A. Swabb, J. Wei, and P. M. Gullino. Diffusion and convection in normal and neoplastic tissues. *Cancer Res.*, 34:2814–2822, 1974.

[45] Amanda Swan, Thomas Hillen, John C. Bowman, and Albert D. Murtha. A patient-specific anisotropic diffusion model for brain tumour spread. *Bull. Math. Biol.*, 80(5):1259–1291, 2018.

[46] K. R. Swanson, E. C. Alvord Jr, and J. D. Murray. A quantitative model for differential motility of gliomas in grey and white matter. *Cell Prolif.*, 33:317–329, 2000.

[47] K. R. Swanson, C. Bridge, J. D. Murray, and E. C. Alvord Jr. Virtual and real brain tumors: using mathematical modeling to quantify glioma growth and invasion. *J. Neurol. Sci.*, 126:1–10, 2003.

[48] J. Z. Wang, Z. Huang, S. S. Lo, W. T. C. Yuh, and N. A. Mayr. A generalized linear-quadratic model for radiosurgery, stereotactic body radiation therapy, and high-dose rate brachytherapy. *Sci. Transl. Med.*, 2(39):39ra48, 2010.

[49] S. M. Wise, J. S. Lowengrub, H. B. Frieboes, and V. Cristini. Three-dimensional multispecies nonlinear tumor growth I: model and numerical method. *J. Theoret. Biol.*, 253(3):524–543, 2008.